INFORMATION TO USERS

This manuscript has been reproduced from the microfilm master. UMI films the text directly from the original or copy submitted. Thus, some thesis and dissertation copies are in typewriter face, while others may be from any type of computer printer.

The quality of this reproduction is dependent upon the quality of the copy submitted. Broken or indistinct print, colored or poor quality illustrations and photographs, print bleedthrough, substandard margins, and improper alignment can adversely affect reproduction.

In the unlikely event that the author did not send UMI a complete manuscript and there are missing pages, these will be noted. Also, if unauthorized copyright material had to be removed, a note will indicate the deletion.

Oversize materials (e.g., maps, drawings, charts) are reproduced by sectioning the original, beginning at the upper left-hand corner and continuing from left to right in equal sections with small overlaps.

Photographs included in the original manuscript have been reproduced xerographically in this copy. Higher quality 6" x 9" black and white photographic prints are available for any photographs or illustrations appearing in this copy for an additional charge. Contact UMI directly to order.

ProQuest Information and Learning
300 North Zeeb Road, Ann Arbor, MI 48106-1346 USA
800-521-0600

THREE DIMENSIONAL NUMERICAL MODELING OF MIXING AT RIVER CONFLUENCES

SangSoo Han

A Thesis

in

The Department

of

Building, Civil, and Environment Engineering

Presented in Partial Fulfillment of Requirements
for the Degree of Master of Applied Science at
Concordia University
Montreal, Quebec, Canada

March 2002

ABSTRACT

THREE-DIMENSIONAL NUMERICAL MODELING OF MIXING AT RIVER CONFLUENCES

SangSoo Han

River confluences are key sites in river systems where, when the difference in depth between the two incoming streams can give rise to a distortion of the mixing layer and to upwelling of the deeper channel fluid in the shallower channel. This has been shown to enhance mixing between the two rivers. In the present study, the relation between the confluence bed geometry and the mixing characteristics is studied using a three-dimensional numerical model (PHOENICS software).

Curvilinear coordinates and modified k-ε closure model are used to investigate the flow structure for a laboratory confluence model and a field stream confluence. A scalar tracer with different concentrations was introduced in the main and the tributary channels of the simulated numerical model to examine the mixing rates in the region downstream of the junction. The tracer is subject to both convection and turbulent

diffusion.

The results displayed the enhanced mixing due to the amplified secondary flow pattern triggered by the effect of bed discordance. Numerical simulations at two flow conditions of the natural confluence with a similar bed discordance in the tributary also confirmed that a rapid mixing occurs due to the effect of bed discordance.

KEYWORDS

Confluences; Three-dimensional numerical model; Mixing; Tracer; Discordance effect

Acknowledgement

I would like to express my gratitude to all those who gave me the possibility to complete this thesis. Especially, I want to thank my supervisors Professor A. S. Ramamurthy from the department of Building, Civil, and Environmental engineering of Concordia University and Professor P. Biron from the department of Geography of Concordia University for their resources, stimulating suggestions, and patience.

TABLE OF CONTENTS

LIST OF FIGURES

LIST OF TABLES

NOMENCLATURE

A: area;

C: mass flow rate across the cell face;

C1: concentration;

C_1, C_2: concentrations of the main and secondary tributaries;

C_E: expected value of concentration;

C_o: observed value of the concentration;

D: diffusive fluxes across the control-volume face;

D: mean flow depth;

D_r: is the depth ratio;

dx: distance between cell centers;

d*t*: time step;

dt_f: user-set false-time-step;

E: roughness parameter;

g : gravitational acceleration;

h: vertical step height;

h_c: surface grid cell thickness;

J: diffusive fluxes across the control-volume face;

k, ke: turbulent kinetic energy;

Mr: momentum flux ratio between the Berthier and the Bayonne River;

p: pressure;

P_s: pressure on the surface;

Pe: Peclet number;

Q_1, Q_2: flow rates of the main and the secondary tributaries;

Q_3: total flow rate of the confluence;

q*: ratio of the upstream main channel flow to the total flow;

R: hydraulic radius;

R_e: Reynolds number;

S_p: source term for the control volume p;

S_ϕ: source term;

U: average velocity;

u: velocity component in the x direction;

u_i: instantaneous value of one of the velocity component u, v, or w;

$\overline{u}_i$: time averaged value;

u_i': time variant component;

V: cell volume;

v: velocity component in the y (planform) direction;

w: velocity component in the z (vertical) direction;

Zd: non-dimensional vertical distance from the main channel bed (Zd=z/d);

Z: height above the bed;

Γ_ϕ: diffusive exchange coefficient for ϕ;

ε: turbulence dissipation rate;

μ: coefficient of dynamic viscosity;

ν: kinematic viscosity;

ν_t: turbulent viscosity;

ν_l: laminar viscosity;

ρ: density of the water;

ϕ: variable;

ϕ_{new} : new value of the variable;

ϕ_{old} : value obtained from the previous iteration;

ϕ_P: cell-value to be computed;

ϕ_{P_Old}: cell-value from the previous iteration;

ϕ^* : present value

1. INTRODUCTION

Stream confluences play an important role as an integral connective part of watersheds. They consist of relatively short but complex reaches in which two or more channels merge and combine flows and sediment from the upper reaches to the lower reaches of watershed. Mixing characteristics in the river confluence are very important for river water quality management, since large quantities of industrial pollutant travel downstream in rivers. Confluences can be also found in hydraulic structures such as a sewer system.

River confluences are very common features in river systems, and they exhibit various configurations with complex geometries. The geometry can change rapidly over short distances due to sediment transport, and the flow field can be very complex. The flow characteristics also change depending not only on the geometry changes of the confluence but also on flow condition. Although studies on river confluence relying on field measurements have proven successful in revealing the flow field at confluences, the numerous difficulties in collecting and analyzing the data from the field have a limitation on natural confluence studies.

A recent trend in river confluence studies is the use of numerical models. However, most of the studies using numerical models in fluvial research in the past have been limited to two-dimensional models. With the recent dramatic increase of computing power, three-dimensional numerical models are getting more popular as they provide a better accuracy in many situations. Several recent studies have used successfully the

three-dimensional numerical model to study natural river confluences (e.g. Weerakoon et al., 1991; Bradbrook et al., 1998, 2000a,b; Lane et al., 1999), and they showed the prospect of three-dimensional numerical modeling as an efficient and effective tool to study the complex flow characteristics, for example in river confluences.

1.1 Research objectives

The followings are the objectives of the study which will be mainly based on the three-dimensional numerical simulation.

1. To determine the effect of discordance on the mechanics of flow and mixing characteristics in stream confluences.

2. To study and suggest methods to overcome difficulties associated with flow predictions for stream geometries which exhibit a high degree of skewness in cell configurations.

3. To determine the effects of flow features upstream of the confluence on the confluence mixing characteristics.

4. To determine the effect of free surface on the mechanics of confluence flow. The rigid-lid simulations will be extended to the case where free surface effects are incorporated in the simulation. To this end, the concept of porosity will be used to determine the free surface of the flow.

Prior to achieving these objectives, the three-dimensional numerical model is validated using laboratory data for simple rectangular open channel junctions with a 30° and 90° junction angle. The effect of discordant beds where one tributary of the confluence has higher channel bed is examined in the validation. In most confluences, the merging streams have differential bed heights, and the flow structure of confluence with discordant (dropping) bed is more complex than that of a concordant (flat) bed.

1.2 River confluence studies

Confluences are important in river, sewer, and irrigation systems, and proper understanding of their dynamics is of great importance. River engineers, earth scientists, and environmental managers need to understand the mixing of the flows in the immediate vicinity of the junction flow. This study is primarily motivated by the need to understand the mixing processes when two streams or channels merge. However, the flow structure must be understood first. Tuthill and Mamone (1997) classified confluences into four categories: confluences of rivers or channels of similar size, confluences of rivers or channels of different size, rivers entering lakes, and lakes drained by rivers. The present study is primarily concerned with the confluence of two similar size streams. When two rivers or open channels merge, they exhibit a variety of complex flow characteristics, and the flow patterns are directly related to the bed morphology and the ensuing mixing process. The bed morphology of the confluence affects the flow pattern, and the flow pattern in turn affects the river morphology by the mechanisms of erosion and deposition

of the bank and bed material. Knowledge of the detailed flow structure should be available to understand the mixing processes in confluences, since it is the direct result of the flow pattern.

Researchers have used different approaches to investigate and understand confluence flow dynamics. The methods of study can be divided into laboratory experiments, observation of natural confluences, and numerical modeling. In the most common and traditional approach, confluence characteristics are determined in prismatic channels of laboratories (e.g. Taylor, 1944; Webber and Greated, 1966; Lin and Soong, 1979; Ramamurthy et al., 1988; Biron et al., 1996 a,b; Hsu et al., 1998). However, there are several limitations in such studies due to the assumptions related to the idealistic flow conditions, the use of simplified channel geometries, and also the use of small-scale physical models.

Field investigations are largely based on point measurements of the velocity field. A large number of sample sites are required to obtain a reasonable representation of the spatio-temporal process characteristics (Lane et al., 1999). In recent times, more emphasis has been placed on computational studies to provide predictions of mixing characteristics that are directly applied to natural confluences. The trend in numerical modeling is to seek the three dimensional solutions to river confluence problems. Carefully calibrated three-dimensional models can overcome the limitations of laboratory and field experiments. Further, they also provide an improved insight into the complex flow dynamics of junction flows (Lane et al., 1999; Bradbrook et al., 2000a). The ability to

provide a realistic representation of the flow geometry representing natural streams involves increased complexities in numerical modeling, related to both grid generation and setting up the appropriate boundary conditions. When the difficulties of modeling are overcome, the result of the mixing characteristics of confluences can be directly applied to situations that are representative of field conditions. Details related to three-dimensional modeling are described in the next chapter.

1.3 Flow Structure

1.3.1 Experimental studies

Natural confluences have a complex geometry, and can be of varying scales. Their flow conditions are also unsteady and complex. Obtaining instantaneous flow information useful for research with an acceptable accuracy is quite difficult or even impossible in many cases. Therefore, researchers often turn to laboratory experiments using prismatic channels and steady flow conditions where it is easier to control variables. Most laboratory experiments have used fixed-bed experiments where the key characteristics of open channel junction flow such as the water depth variation, the separation zone, and the effects of discordant beds on the flow field were investigated. Mobile-bed experiments were also used in some cases to investigate the relationship between flow structure and bed morphology.

The main features of flow through a confluence are the flow separation zone, stagnation

zone, shear layer (or mixing layer), and flow recovery zone (Figure 1.1). When the two flows collide, water surface rises in the stagnation zone. The flow from the tributary separates at the downstream end of the tributary's mouth, and this reduces the cross-section area available for the combined flows. Thus, the flow accelerates in an adjacent maximum velocity zone (Best, 1987). Downstream of the separation zone, the flow expands in the flow recovery zone. The shear layer plays a critical role in the mixing process and will be discussed in detail in another section. On Figure 1.1., it is depicted as a simple curve, but this is a time-averaged representation of the plane between the two combining flows. It is characterized by strong vortices that initiate the mixing of the merging flows. These, combined with secondary circulation, are key features for the mixing processes.

Within the separation zone, a bar is formed by the deposition of sediment (Figure 1.2) (Mosley, 1976; Weerakoon, 1990). A scour zone is also present and is aligned with a portion of the shear layer between the two flows (Mosley, 1976; Best, 1987). The depth of the scour hole increases with an increase in junction angle due to the increase in the secondary circulation intensity. The depth and the location of the scour hole are also a function of the discharge ratio, as well as the sediment load (Mosley, 1976). The scour hole that moves into the junction area of the confluence acts as a step and may create bed discordance (De Serres et al., 1999).

The junction of two flows has been shown to produce significant changes in the flow depth, even for relatively small junction angles (Taylor, 1944; Webber and Greated, 1966; Lin and Soong, 1979; Ramamurthy et al., 1988). The greater head differences, however, occur

at relatively large junction angles (Webber and Greated, 1966). Several analytical models have been derived to estimate the changes in depth, as well as the energy loss through the junction (Taylor, 1944; Lin and Soong, 1979; Ramamurthy et al., 1988; Gurram et al, 1997; Hsu et al., 1998).

The separation zone at the downstream junction corner has been investigated thoroughly as it is a critical component of the flow dynamics in confluences (Figure 1.1). Its size and shape are determined by the discharge ratio between the tributary channels and by the junction angle (Modi et al., 1981; Best and Reid, 1984; Best, 1987). The geometry of the separation zone was calculated using conformal mapping by Modi et al. (1981). Best and Reid (1984), however, re-examined their model and concluded that they had overestimated the width of the separation zone and, in turn, underestimated the area of the channel occupied by the free stream.

The flow structure at junctions is complex and highly three-dimensional. The converging flows undergo three-dimensional separation before the confluence due to a high stagnant pressure at the junction apex (Fujita and Komura, 1979). In symmetrical (Y-shaped) confluences, two counter-rotating helical cells are observed in the contraction zone over the scour hole (Mosley, 1976; Ashmore, 1982; McLelland et al., 1996). Water surface superelevation has been observed in that zone (Mosley, 1976; Weerakoon, 1990). In nature, however, these junctions occur mainly in braided-river environment. Most confluences have an asymmetrical shape, in which only one of the tributary is angled compared to the main flow. Only a single helical cell develops in this case as, when the

flow and curvature of the tributary is dominant, the confluence becomes similar to a single meander (Fujita and Komura, 1979; Rhoads and Kenworthy, 1995; Bradbrook et al., 2000a). There are many difficulties in clarifying this complex flow structure with either visualization techniques or turbulence measurements. This complexity also is visible at the water surface which shows zones of superelevation and depressions (Weber et al., 2001).

Most of the experimental studies used prismatic open channel confluences with equal bed elevation (i.e. concordant beds) for the main and lateral channels. Most natural confluences, however, have different bed elevations (i.e. discordant beds) and this has a large influence on the flow structure at these sites. Bed discordance creates a distortion of the mixing layer towards the shallower tributary, with upwelling of flow from the deeper channel into the shallower channel (Best and Roy, 1991; Biron et al., 1996a;b). Furthermore, bed discordance limits flow deflection at the bed and the flow acceleration in the contraction zone is reduced due to the absence of a separation zone close to the bed (Biron et al., 1996a;b).

1.3.2 Natural confluences

Very few sets of data from field confluences are available compared to those of laboratory experiments, and most of them are very recent. Mamedov (1989) measured velocity field and sediment concentration of the flow, and identified the major characteristic zones of confluence flow such as the separation zone and stagnation zone in the Kura River. Rhoads and Kenworthy (1995, 1998), Rhoads (1996), and Rhoads and Sukhodolov (2001)

investigated a natural confluence in east central Illinois, and provided extensive information on the time-averaged flow structure of the asymmetrical stream confluence with various flow conditions. The temperature field shows that there is a well-defined mixing layer in the junction area, but the lateral mixing is limited in that zone. The lateral position of the mixing layer is a function of the momentum ratio between two combining flows. They also confirmed the existence of two counter-rotating helical cells that were reported in the earlier laboratory experiments (Mosley, 1976; Ashmore, 1982).

The presence and the effect of these helical cells are, however, still a matter of controversy (Best and Roy, 1991; Biron et al, 1996 a,b). De Serres et al. (1999) reported detailed three-dimensional data of mean and turbulent structure of flow for the natural discordant bed confluence of Bayonne River and Berthier River in Québec, Canada for various flow conditions using Electromagnetic Current Meters (ECM). They have identified the major characteristics of the confluence flow dynamics such as the acceleration zone, the stagnation zone, and the zone of flow deflection. A zone of separation was not detected although very low velocity was measured in the zone of the downstream junction corner. This contradicts Rhoads and Kenworthy (1995)'s report. The upwelling of the flow similar to the laboratory experiment with discordant bed from Biron et al. (1996a) was also noted close to the avalanche face at the mouth of the tributary. The shear layer region was characterized by high turbulence intensity and turbulent kinetic energy. Lateral distortion of the mixing layer, attributed to bed discordance, was observed and is in agreement with previous laboratory studies (Best and Roy, 1991; Biron et al., 1996a,b) and other observations at a discordant bed confluence (Roy and De Serres, 1989).

1.3.3 Numerical simulations

Numerical models have been increasingly used to improve our understanding of river flow dynamics, but the turbulent nature, irregular geometry of the open channels, time dependence, and complex sediment transport phenomena make the prediction of flow in natural channels a challenging task for even the most advanced computational fluid dynamics methods. Until now, predictions of flow and sediment transport in open channels and rivers have been mostly at the levels of 1D and 2D simulations (e.g. Andrew and Nelson, 1989; Shimizu and Itakura, 1989; Tingsanchali and Maheswaran, 1990; Bridge and Gabel, 1992; Lane et al., 1995). However, such models may not represent complex secondary flow structures such as those observed at confluences. Some models even neglect the influence of the secondary flow. This can only be accounted for realistically with three-dimensional models which are becoming more widespreadly used (e.g. Weerakoon et al., 1989, 1991; Lane et al., 1999; Bradbrook et al., 1998, 2000a,b; Meselhe and Sotiropoulos, 2000; Nagata et al., 2000; Wu et al., 2000).

The development of a sophisticated three-dimensional model requires a considerable increase in computational resources, and increasing sophistication also implies an increasing need to recognize the primary assumptions behind model development (Lane et al. 1999). The computing grid has to be constructed to represent the physical domain accurately, and the number of grid cells has to be large enough to capture a complex flow field accurately. Three-dimensional modeling also requires increased details in the

boundary conditions. Inadequate specification of boundary conditions will limit the quality of model predictions. Weerakoon et al. (1991) used elliptic three-dimensional model successfully, based on a finite volume method and standard k-ε turbulence model to investigate three-dimensional flow structures in a channel confluence with rectangular sections. Bradbrook et al. (1998) studied flow in a parallel confluence of unequal depth channels using a three-dimensional numerical model (PHOENIX). Lane et al. (1999) assessed the applicability of the three-dimensional numerical model to a river channel confluence in a gravel bed river. The results show that the model has limitations due to the difficulties of implementing certain boundary conditions. However, three-dimensional models generated more reliable results than two-dimensional models. The model predicted the flow field of a laboratory confluence with rectangular channel with better accuracy than that of a natural confluence due to the fact that the boundary conditions are simpler and relatively easier to implement. Validation is also easier with laboratory data with fixed flow conditions than with natural confluence data.

Experimental analysis shows that river confluences and open channel junction flow have zones of super elevation and depression of the water surface (Mosley, 1976; Ashmore, 1982; Weerakoon and Tamai, 1989, Bridge and Gabel, 1992; Rhoads, 1996). However, many three dimensional models apply the so called 'rigid-lid' or plane-of–symmetry condition at the free surface, not taking into account the free surface elevation changes caused by the pressure gradients along lateral and transverse directions. Ouillon and Dartus (1997) presented the porosity method to track the free surface geometry, and its application within a three-dimensional numerical model. Their model was able to predict water depth

around a groyne in a wide rectangular channel with a small error. They also point out that the porosity method can improve the estimation of the reattachment length, compared to results from the 'rigid lid' assumption. Meselhe and Sotiropoulos (2000) compared the results from three-dimensional numerical simulations and experiment for an open channel meander. The model was capable of predicting the variable free water surface allowing the computational mesh to deform during the iterative solution procedure. The results show good agreement with laboratory data. Bradbrook et al. (1998, 2000a) and Lane et al. (1999) applied successfully the porosity concept of free surface approximation similar to Ouillon and Dartus (1997)'s on a river confluence. Bradbrook et al. (2000b) also used Large Eddy Simulation (LES) for river channel confluences, allowing unsteady solutions that solve turbulent eddies at the scale of the computational grid and using the porosity concept.

1.3.4 Mixing processes

Despite the importance of the mixing processes at river confluences, there is a limited number of studies available. Confluences of two rivers are characterized by a shallow mixing layer. However, most of the shallow mixing layer studies are done using parallel channels which have a simpler velocity pattern than the confluence of streams or channels (e.g. Chu and Babarutsi, 1988; Tukker, 1997; Uijttewaal and Tukker, 1998). The velocity differences between both sides of the mixing layer gives rise to instabilities in the fluid motion resulting in the development of the mixing layer. The mixing layer is characterized by amplified turbulence intensities in lateral and vertical directions of flow rather than in the downstream flow direction (Chu and Babarutsi, 1988; Biron et al., 1993). In addition

to the lateral velocity gradient, other flow patterns in the confluence of channels are known to enhance the mixing process. According to the experiments of Biron et al. (1996a,b), the mixing layer that is represented by high turbulence intensity between the confluent flows exists for concordant and discordant bed cases. However, the pattern is quite dissimilar. For the concordant bed case, the location of the mixing layer does not change vertically. Only the intensity of turbulence increases towards the water surface. In the case of discordant beds, the base of the shear layer is distorted towards the shallow tributary flow, and this agrees with Best and Roy (1991)'s observation. Gaudet and Roy (1995) studied the effect of bed morphology on longitudinal mixing in a series of confluences. They measured the electrical conductivity to measure the concentration of ionic species, and showed that complete mixing is achieved at distances five to ten times shorter than previously published mixing lengths that were more than 100 channel widths (Rutherford, 1994). This enhanced mixing process was attributed to the effect of bed discordance at confluences.

2. COMPUTATIONAL MODELLING

One of the methods for studying fluid flow phenomena is the computational approach. This approach uses a limited number of assumptions and a computer code to solve the resulting governing equations. The terms in the differential equations are then replaced by appropriate finite differences at each grid point and the resulting equations are integrated. As mentioned in the previous chapter, the computational approach has advantages over experimental studies or field measurements. Laboratory experiments use models that are much smaller than the prototype. It is therefore not always possible to simulate the true condition of the actual model in such studies. On the other hand, numerical modeling can provide information not available by other means. The limitations of numerical modeling are computer storage capacity, speed and assumptions. Other limitations arise as a result of the inability to understand and mathematically model certain complex phenomena. None of these limitations of numerical modeling are insurmountable in principle.

This chapter reviews some of the principles of computational fluid dynamics used to study natural confluence flows including the mathematical concepts of the PHOENICS model used in this study and grid generation.

2.1 Governing equations

The model is based on the full three-dimensional form of Navier-Stokes equations that are based on fundamental physical principles. These equations relate the local pressures and

velocities within a body of moving fluid. They consist of the conservation of mass, momentum and energy. The Cartesian form of the continuity equation and full three-dimensional Navier-Stokes equations for an incompressible fluid are given below.

Conservation of Mass:

$$\frac{\partial u}{\partial x}+\frac{\partial v}{\partial y}+\frac{\partial w}{\partial z}=0, \tag{2.1}$$

where ρ is the density of the water (in kg/m^3), and u, v, and w are the components of velocity in the x, y (planform) and z (vertical) directions, respectively.

Conservation of Momentum in the three coordinate directions x, y and z:

$$x\text{-}direction: \quad \rho\left(\frac{\partial u}{\partial t}+u\frac{\partial u}{\partial x}+v\frac{\partial u}{\partial y}+w\frac{\partial u}{\partial z}\right)=-\frac{\partial p}{\partial x}+\mu\left(\frac{\partial^2 u}{\partial x^2}+\frac{\partial^2 u}{\partial y^2}+\frac{\partial^2 u}{\partial z^2}\right)$$

$$y-direction: \quad \rho\left(\frac{\partial v}{\partial t}+u\frac{\partial v}{\partial x}+v\frac{\partial v}{\partial y}+w\frac{\partial v}{\partial z}\right)=-\frac{\partial p}{\partial y}+\mu\left(\frac{\partial^2 v}{\partial x^2}+\frac{\partial^2 v}{\partial y^2}+\frac{\partial^2 v}{\partial z^2}\right)$$

$$z-direction: \quad \rho\left(\frac{\partial w}{\partial t}+u\frac{\partial w}{\partial x}+v\frac{\partial w}{\partial y}+w\frac{\partial w}{\partial z}\right)=-\frac{\partial p}{\partial z}+\mu\left(\frac{\partial^2 w}{\partial x^2}+\frac{\partial^2 w}{\partial y^2}+\frac{\partial^2 w}{\partial z^2}\right)-\rho g$$

(2.2a,b,c)

where μ is the coefficient of dynamic viscosity (in $kgm^{-1}s^{-1}$), g is the acceleration due to gravity (in ms^{-2}), and p is pressure.

2.1.1 General form of governing equations

The continuity equation (2.1) and the Navier–Stokes equations (2.2) can be written in a general conservation form, so they can be applied to numerical computer programming

conveniently. This helps to simplify and organize the logic in a given computer program. The basic balance or conservation equation is that the net source within the cell is the difference between the outflow from the cell and the inflow into the cell. The quantities being balanced are the dependent variables such as mass of phase, mass of a chemical species, energy, momentum, turbulence quantities, electric charges, etc.

There are four terms appearing in the balanced equation: convection, diffusion, time variation, and source terms. The single-phase conservation equation can be written as:

$$\frac{d(\rho\phi)}{dt} + div[(\rho u\phi) - \Gamma_\phi grad(\phi)] = S_\phi \qquad (2.3)$$

where: ϕ is the variable, u is the vector's velocity, Γ_ϕ is the diffusive exchange coefficient for ϕ, and S_ϕ is the source term.

For the momentum equations (Navier-Stokes equations), the variables are u, v, and w, which are the three components of velocity vectors.

$\phi = u, v, w$: Momentum equations (Navier-Stokes equations)

$$\Gamma_\phi = \rho(\nu + \nu t)$$
$$S_\phi = -grad(p) + gravity + friction$$

For the continuity equations, the variable is 1.

$\phi = 1$: Continuity equation

$$\Gamma_\phi = 0$$
$$S_\phi = 0 + boundary\_sources$$

where ν_t, ν_l are the turbulent and laminar viscosities respectively.

The balance equations cannot be solved numerically in differential form, hence the equations need to be transformed.

2.1.2 Discretisation

Analytical solution of partial differential equations involves closed form expressions that yield dependent variables that are continuous throughout the domain. However, numerical solutions can give answers only at discrete points in the domain termed as grid points. This is done by replacing the partial differential equations with a system of algebraic equations that can be readily solved for the values of the flow field variables at the discrete grid points only. This discretisation requires the definition of discrete time-steps and the division of space into discrete units. All methods in CFD utilize some form of discretisation. Finite difference, finite volume, and finite element methods are widely used discretisation techniques. This study uses finite volume method (FVM) with a structured grid. In this method, the physical space is split up into small volumes and the partial differential equations are integrated over each of these volumes. Then, the variables are

approximated by their average values in each volume and the changes through the surfaces of each volume are approximated as a function of the variables in neighboring volumes.

The three-dimensional grid cells have six faces. If a Cartesian grid is used, then these cells are cubic. For a more complicated geometry, they may be distorted in real space (x, y, z) but can still be treated as a cube in computational space (i, j, k). The convention of the nomenclature adopted in the model is shown below.

P cell center

N, S, E, W, H, L neighbor cell centers

S →N positive j direction

W→E positive i direction

L →H positive k direction

T cell center at previous time step

The finite volume equations (FVE's) are obtained by integrating the differential equation over the cell volume. Interpolation assumptions are required to obtain scalar values at the cell faces and vector quantities at cell centers. The FVE's have the following form after integration:

$$a_P\phi_P = a_N\phi_N + a_S\phi_S + a_E\phi_E + a_W\phi_W + a_H\phi_H + a_L\phi_L + a_T\phi_T + \text{source terms} \qquad (2.4)$$

where:

$$a_P = a_N + a_S + a_E + a_W + a_L + a_H + a_T \text{ (by continuity)}$$

The neighbor links, the a's, have the form:

$$a = \underset{\text{(convection)}}{A\,u\,\rho} + \underset{\text{(diffusion)}}{A\,\Gamma_{\phi}\,/\,dx} + \underset{\text{(transient)}}{V\,\rho\,/\,dt} \qquad (2.5)$$

where A is the area, u is the velocity component perpendicular to the face, V is the cell volume, dx is the distance between cell centers and dt is the time step.

The equation is cast into a correction form to obtain a solution. In the correction form, the sources are replaced by the errors in the original differential equation. The corrections tend to be zero as convergence is approached, reducing the possibility of round-off errors affecting the solution. An equation of this form is created for every variable and for every cell. These equations are solved using one of the equation solvers. The neighboring links increase with inflow velocity, cell area, fluid density and transport coefficient, decrease with internodal distance, and are always positive.

2.1.3 Interpolation in the Finite Volume Equation (FVE)

Depending on the variable, the location of storage in the cell is different. Variables may be thought of as being dependent, auxiliary, or derived from an algebraic equation. In each case, they can be subdivided into scalar and vector quantities. Table 2.1 summarizes the variables used.

Table 2.1 Variables used in the model

Dependent parameters	Scalar quantity	Pressure Temperature Mass fraction Volume fraction Turbulence quantities
	Vector quantity	Velocity resolutes Displacements
Auxiliary parameters	Scalar quantity	Density Viscosity Diffusivity Inter fluid transport
	Vector quantity	Various non-isotropic properties Gravity forces and other body forces
Geometric parameters	Scalar quantity	Cell volume Volume porosity factor Inter fluid surface area per unit volume
	Vector quantity	Cell center and corner coordinates Distance between a cell to an adjacent cell centers Cell face area Cell area porosity

The scalar are stored at the center points of the six-sided cells, with values supposed to be typical of the whole cell, and vectors are stored at the center points of the six cell faces. Interpolation assumptions are therefore required to obtain scalar values at cell faces and vector quantities at cell centres. A particularly important consideration is the discretisation of the convection terms in the finite volume equations (PHOENICS manual). The accuracy and stability of the solution depends on the numerical scheme used for these terms. If the convective (J) and diffusive (D) parts of the flux across a particular face (2.5) are separated then the FVE (2.4) can be written:

$$J_N - J_S + J_E - J_W + J_H - J_L + D_N - D_S + D_E - D_W + D_H - D_L = S_P \qquad (2.6)$$

where S_p is the source term for the control volume p, and J and D represent, respectively, the convective and diffusive fluxes across the control-volume face. The convection fluxes through the cell faces are calculated by:

$$J = C.f \tag{2.7}$$

where C is the mass flow rate across the cell face. If the convected variable, f, is a scalar quantity stored at the cell centre, its value must be determined by interpolation. The most natural interpolation assumption for the cell-face value of the convected variable f might be to average the values at the two cell centres on either side of the face:

$$f = 0.5(f_u + f_d) \tag{2.8}$$

where the subscripts u and d refer to the upwind and downwind cell centres respectively. This is known as the Central-Differencing Scheme (CDS) and is 2nd-order accurate (uses values at two other cells) but can lead to unrealistic oscillations in regions of strong convection. Therefore a Hybrid-Differencing Scheme (HDS) (Spalding, 1972) was used which only uses the CDS where numerical diffusion dominates, defined by a local cell Peclet number < 2. The cell Peclet number at a particular face is given by:

$$Pe = \rho|u|\frac{A}{D} \tag{2.9}$$

where u, A, and D are defined in equation 2.5. In high convection regions, (Pe > 2), the Upwind-Differencing Scheme (UDS) is used which assumes the convected variable at the cell face is the same as the upwind cell centre:

$$f = f_u \tag{2.10}$$

This is very stable, but is only 1st-order accurate and is therefore highly diffusive when the flow direction is skewed relative to the grid lines. Such numerical diffusion can be reduced by a careful design of a grid mesh, and by a higher grid resolution. However, for problems involving re-circulating flow, some error may still remain. A scheme with a higher order of accuracy could be used, but this can cause stability problems. This study focuses on the use of a developed model to investigate a particular problem, rather than on assessing the development of that model. It is also considered that the errors arising from the interpolation scheme used are not likely to be significant compared to uncertainty in the specification of boundary conditions in the complex problems to be investigated. More effort was placed on the grid generation and boundary conditions.

2.1.4 Solution methods

2.1.4.1 Point by point method

In this method, the algebraic equations reduce to:

$$\phi_p = (\Sigma(a_i\phi_i) + sources) / a_p \tag{2.11}$$

The computed corrections are added after the slab has been completely converted. Point by point solution method is most commonly used for the velocities, especially when viscosity is important. Point by point method is useful when equations are tightly coupled, and/or non-linearities are severe, because the rate of change of variables from sweep to sweep is low, and this introduces additional stability. However, this method leads to a long convergence time (PHOENICS manual).

2.1.4.2 Slabwise method

Values are obtained for all cells at a particular k location, those on the adjacent slabs being presumed to be known. If the number of the cells of the slab in any direction is 1, the solver does not require iteration. It is much more economical to sweep the domain many times. This solution is used for parabolic flows.

2.1.4.3 Whole field method

Whole field solution is preferable when non-linearities are slight, especially for heat conduction or velocity potential or other potential equations. This method is always recommended for the pressure correction equation, as this transmits effects of flow boundary conditions and blockages throughout the domain (PHOENICS manual).

2.1.5 Coupled equations

The momentum and continuity equations are linked, in that the momentum equations share pressure, and the velocities enter in the continuity equation. There is no direct equation for the pressure. So the task of all CFD codes is to join the variable without an equation (pressure), to the equation without variable (continuity). PHOENICS does this using SIMPLEST, a variant of the SIMPLE algorithm developed by Pantankar and Spalding (1972). The main steps in the SIMPLE and SIMPLEST algorithm are:

1. Guess a pressure field.
2. Solve the momentum equations using this pressure field, thus obtaining velocities which satisfy momentum, but not necessarily continuity.
3. Construct continuity errors for each cell: inflow - outflow.
4. Solve a pressure-correction equation. The coefficients are d(u)/d(p), and the sources are the continuity errors.
5. Adjust the pressure and velocity fields. Obtain velocities that satisfy continuity, but not momentum.
6. Go back to step 2, and repeat with the new pressure field. Repeat until continuity and momentum errors are acceptably small.

2.1.6 Convergence

Getting a solution in CFD takes iterations to reach the convergence starting from the initial guessed value. The non-linearity of the Navier-Stokes equations, and the pressure term which is an unknown variable included in the equations require this iterative approach. PHOENICS solves all variables using iterative methods. Modified strongly implicit procedure (SIP) is used as a solver for the matrix for a scalar like pressure. This SIP

procedure can get solutions at all grid points implicitly, so as to accelerate convergence. SIP is applied for each slab of the mesh in the three-dimensional grid (PHOENICS manual).

Relaxation is a commonly used device that promotes a convergence, and there are two types: Linear relaxation and false time step relaxation.

2.1.6.1 Linear relaxation

The new value of the variable is calculated from the following equation. It is called the linear relaxation since this has the form of a linear equation

$$\phi_{new} = \phi_{old} + \alpha(\phi^* - \phi_{old}) \tag{2.12}$$

where ϕ_{new} is the new value of the variable, ϕ_{old} is the value obtained from the previous iteration, and ϕ^* is the present value, after the current iteration. The models used in this study required about 0.3 as a linear relaxation value α. The value is recommended for the model using boundary fitted coordinate coupled with pressure (PHOENICS manual).

2.1.6.2 False time step relaxation

False time step relaxation is used to slow down computation by adding an extra term on the finite volume equations

$$\frac{\rho V}{dt_f}(\phi_{P\_Old} - \phi_P) \tag{2.13}$$

where ϕ_P is the cell-value to be computed, ϕ_{P_Old} is the cell-value from the previous iteration, V is the cell volume, and dt_f is a user-set false-time-step. Using larger dt_f makes the added extra term become smaller and the solution becomes under-relaxed. If the computation converges, ϕ_{P_Old} and ϕ_P become identical, so that the finite volume equation is unchanged (PHOENICS manual).

To promote convergence, two methods are used in PHOENICS. A variable can be prevented from overshooting, during the iteration procedure. The range of physically realistic values can be preset for upper and lower boundaries. Another way to control convergence is to control the relaxation factor to slow down the changes made to the values of the variable during the solution procedure. Relaxation involves, therefore, changing the values obtained form the solution algorithm, so that they are closer to the pre-existing ones.

2.2 Turbulence modeling

One of the most distinct characteristics of the confluence flow is the existence of a turbulent mixing layer, and selecting the most appropriate turbulent model is one of the key elements in this study. Turbulence is inherently three-dimensional, time dependent, dissipative and strongly diffusive. The complete description of turbulent flow requires enormous amount of information (Wilcox, 1988). The solution of the Navier-Stokes equations combined with the continuity equation is considered to be a valid description of

laminar and turbulent flows, and it is possible to simulate turbulent flow using the *direct numerical simulation* (DNS). However, DNS has been applied to a very small number of flows with low Reynolds number, since this requires an enormous amount of computer resource and an extremely fast computer to represent all the eddies from the smallest scale corresponding to the dissipative motions, to the largest scale, corresponding to the domain dimension of the model. Further, the time step chosen for the simulations must be sufficiently small to resolve the fastest fluctuations.

One of the other alternatives to DNS is *large eddy simulation* (LES). Large-scale structures are calculated directly by solving the three-dimensional time dependent Navier-Stokes equations, and only the effect of the sub-grid model for turbulence of scales smaller than the computational spacing. Although LES is more economical than DNS, its use is limited due to the prohibitive expense at high Reynolds number, and the difficulties in specifying initial and boundary conditions. It has been used, however, successfully at a river confluence to show periodicities in the mixing layer (Bradbrook et al., 2000b).

The other alternative is the Reynolds averaged Navier-Stokes (RANS) equation. The velocity is decomposed into a mean and a fluctuating part:

$$u_i = \overline{u}_i + u_i' \tag{2.14}$$

where u_i is the instantaneous value of one of the velocity component u, v, or w. $\overline{u}_i$ is the time averaged value and u_i' is the time variant component. The mean values are obtained

by averaging over a time scale, dt, which is long compared to that of turbulent motion, and in unsteady problems small compared with the unsteadiness of the mean motion. The definitions of instantaneous quantities are substituted into the equations of the instantaneous motion, which are then averaged to produce the equations of the mean motion.

The averaged equations using equation 2.14 are:

$$\frac{\partial \bar{u}}{\partial x} + \frac{\partial \bar{v}}{\partial y} + \frac{\partial \bar{w}}{\partial z} = 0 \tag{2.15}$$

$$\rho\left(\frac{\partial \bar{u}_i}{\partial t} + \bar{u}_i\frac{\partial \bar{u}_i}{\partial x} + \bar{u}_i\frac{\partial \bar{u}_i}{\partial y} + \bar{u}_i\frac{\partial \bar{u}_i}{\partial z} + \frac{\partial \overline{u_i'u'}}{\partial x} + \frac{\partial \overline{u_i'v'}}{\partial y} + \frac{\partial \overline{u_i'w'}}{\partial z}\right) = -\frac{\partial \bar{p}}{\partial x_i} + \mu\left(\frac{\partial^2 \bar{u}_i}{\partial x^2} + \frac{\partial^2 \bar{u}_i}{\partial y^2} + \frac{\partial^2 \bar{u}_i}{\partial z^2}\right) \tag{2.16}$$

The time-averaged conservation of mass, equation (2.15), is identical to the instantaneous equation (2.1) with the mean velocity replacing the instantaneous velocity (Wilcox, 1998). However, the statistical-averaging process has introduced unknown turbulent correlations ($\overline{u'_i u'_j}$) into the mean–flow equations which represent the turbulent transport of momentum and mass (Wilcox, 1998). The unknown turbulent correlations are called the Reynolds or turbulent shear stresses. The turbulence model is required to determine the turbulent shear stress.

The traditional modeling assumption, following Boussinesq in 1877, is to make this a gradient diffusion term, analogous to molecular shear:

$$\tau_t = -\rho\overline{u'v'} = \mu_t \frac{\partial \bar{u}}{\partial y} \tag{2.17}$$

where μ_t is the eddy viscosity. The eddy viscosity, μ_t, has the same dimension as the viscosity, but it is not a fluid property. It depends on the state of turbulence and must be determined by the turbulence model. This is called *effective viscosity concept* (EVC). PHOENICS has a number of turbulence models, and they can be classified depending on the use of *effective viscosity concept* (EVC) (Boussinesq, 1877) which is treating the behavior of a turbulent flow like that of a laminar flow with increased viscosity.

2.2.1 Classification of turbulence models

Turbulence models in PHOENICS fall into one of these three groups: Group I. Models adopting EVC: Group II. Models not using EVC; Group III. Models making some inessential use of the EVC. Group I can be further divided into several sub groups depending on the methods adopted for calculating the magnitude of the effective viscosity. Models based on the standard k-ε model fall into this subgroup using two differential equations. Reynolds stress model is in group II, and Smagorinski (1963)'s model which is one of the large eddy simulation (LES) method belongs to the group III.

This study adopted k-ε model with the renormalization concept, and this also belongs to the subgroup using two different equations in group II. The renormalization group (RNG) k-ε method adopted in this study is based on the version that Yakhot et al. revised in 1992.

PHOENICS manual recommends k-ε turbulence model, when re-circulation, or other strong elliptic effect, are dominant, and it is known that the RNG k-ε model is superior to the standard k-ε model. This model has been used successfully in the natural confluence studies such as Bradbrook et al. (2001) and Lane et al. (1999).

2.2.2. Renormalized group (RNG) k-ε model

RNG stands for renormalized group methods. It is an extension of the standard k-e model. The k-e model is known to be too dissipative (Wilcox, 1998). The turbulent viscosity in recalculation tends to be too high, thus damping vortices. It provides an improved performance for several classes of complex turbulent flows such as separated flows, flows in curved geometries, flows strained by impingement or stagnation, and flows with moderate swirl (Choudhury, 1993).

The RNG method is derived from mathematical methods as opposed to being empirical. It has additional terms in the transport equations. This model is free of adjustable parameters. However, two additional equations are derived for the turbulent kinetic energy k, and the rate of dissipation, ε (Yakhot and Orszag, 1986). In this approach, RNG method involves systematic approximations of the full Navier-Stokes equations that are obtained by using the perturbation theory to eliminate or decimate infinitesimal bands of small scale models, iterating the perturbation procedure to eliminate finite bands of modes by constructing recursion relations for the renormalized transport coefficients, and evaluating the parameters at a fixed point in the lowest order of a dimensional expansion around a certain

critical dimension. The decimation procedure, when applied successively to the entire wave number spectrum leads to the RNG equivalent of full closure of the Reynolds averaged Navier-Stokes equations. The resulting RNG transport coefficients are differential in character as opposed to ad hoc algebraic coefficients of conventional closure methods. All constants and functions appearing in the RNG closures are fully determined by the RNG analysis (Lam, 1992).

The RNG method provides an analytical method to eliminate small scales from the Navier-Stokes equations, thus leading to a dynamically consistent description of the large-scales. The formal process of successive elimination of small scales together with rescaling of the resulting equations permits the derivation of transport approximation in turbulent flows. At high turbulence Reynolds numbers, the RNG k-ε model of Yakhot and Orszag (1986) is of the same general form as the standard k-ε model, except that the model constants are calculated explicitly from the RNG analysis and assume somewhat different values (PHEONICS manual). Details of mathematical description of the model can be found in Yakhot and Orszag (1986) and Yakhot et al. (1992).

2.3 Grid generation

Grid generation is one of the most time consuming tasks when solving partial differential equations on an oddly shaped domain such as the geometry of a natural confluence. Depending on how the domain is discretised and grid points are controlled, the solutions

obtained using an appropriate solution scheme may not be so accurate, due to many errors, such as discretisation and interpolation errors. This study uses the boundary or body fitted coordinate (BFC) to cope with the high irregularity of the geometry at the natural confluence. However, this method has a drawback of additional computational and storage expense. BFC can provide good geometric representation and economical grid refinement close to the surface. It can also reduce numerical false diffusion errors by proper alignment of grid and flow direction (Knupp and Steinberg, 1993).

There are certain characteristics of the mesh to be controlled to produce accurate predictions from the simulation (Shin et al. 1991).

a. Local density of the cells

Higher density of cells in the domain can provide a great accuracy in the simulation, but this leads to longer computation time. Therefore the total number of grid points should be kept to the minimum needed to obtain solutions of the desired accuracy. The grid should conform to the physical boundary of the spatial domain so that finite approximations are accurate, and at the same time more cells should be placed in areas where gradients are large. The data from the lab experiments and field measurements show that there are several areas where the velocity field exhibits a large gradient in a confluence. This includes the separation zone and the mixing layer, and the grid has to be constructed considering those areas. This study used the personal computer version of PHOENICS, so the grid efficiency of the model was a very important factor to consider.

b. Smoothness of the grid distribution (aspect ratio)

The smoothness of the cell distribution is also to be controlled. The spacing between grid points should change gradually from a region where grid points are concentrated to a region where grid points are sparsely distributed, especially in regions where gradients of the flow are large, since large variations in grid density or shape can cause numerical diffusion. This might lead to inaccurate results or instability.

c. Angle of cells

Grid lines should intersect a boundary perpendicularly, so that the derivative boundary conditions can be implemented more accurately. Inside the spatial domain, the angle of intersection between grid lines needs to be nearly perpendicular, but must be somewhere between 45 and 135 degrees. This imposed challenges on the construction of the natural confluence mesh at the region of junction apex and river banks. Figure 2.1 shows the location of the geometric sampling points at the field site. The mesh was constructed following the boundary pattern, so that the grid angle in the apex zone **P** very closely approached 35° (Figure 2.2).

Figure 2.3 shows the shape of the cross-section at 20.0m from Figure 2.1with the grid lines. It is clear that the cells located at the shaded area in Figure 2.3 would be highly skewed without a grid control. Some of the cells in that region can have low intersection angles. The grid angles in the lighter area of Figure 2.4a need to be controlled by adjusting the size of the cells and by using curves instead of straight lines for grid lines, and Figure 2.4b

shows the improved gridlines for section A from Figure 2.3.

d. Alignment of the grid lines

One set of grid lines should align with the flow direction. This condition is important for convection-dominated flows when the aspect ratio of the control volume of each grid point is very high.

There are some problems using the FVM. First, slope discontinuities present in the boundaries of spatial domains propagate into the interior of the grid systems generated. These discontinuities in the slopes of the grid lines are undesirable since they can lead to errors in the solution. To correct this problem, some technique should be employed to smooth the grid. One way is to apply a Laplacian operator to the region near the discontinuity. When connecting curves are discretized to form grid points, the orthogonality, which was forced at the boundaries, may be lost. This is also a problem although satisfying all the control conditions stated above and avoiding the problems at the same time is almost impossible in every part of the spatial domain. The grid should be tested to meet the above conditions as much as possible to give the most accurate predictions.

2.3.1 Multi-blocking technique

The methods of grid generation are typically grouped as structured, multi-block, and unstructured grids. This classification is based on the description of the layout of the

physical cells and the neighborhood relationship between cells in a given grid. Grid generation was done for most of this study using the GEOGRID software, which is based on the structured multi-block method. Structured grids are built with a rigid topological framework, and the unstructured grids have no underlying structure. Multi-block grids are usually an unstructured collection of structured blocks. Structured grid is simpler to deal with for application development, computation, and visualization. The computational connectivity of the grid can also be simplified by using a structured grid to achieve an efficient computation. Figure 2.5 illustrates the concept of multi-block grid. The geometric component such as the tributary of the laboratory flume experiments can be dealt with nearly independently, so that the computational efficiency of the structured grid is still retained. However, fitting of the complex geometrical intersections within individual blocks and constructing blocks that properly share boundary surfaces require significant care.

Since geometric components can be dealt with nearly independently, it is easier to design a grid for a complicated geometry with a multi-block than with a structured grid, but filling in complex geometry intersections and building blocks that properly share boundary surfaces usually require a large amount of effort and partially offsets the benefits of the multi-block method (Steinbrenner et al, 1990).

Laboratory experiments of discordant bed confluence introduced the problem of satisfying the grid control conditions mentioned above at the sharp edge of the step and the junction apex area prompted the use of the multi-block technique. The configuration of the grid with two blocks for concordant case laboratory experiment is shown in Figure 2.6.

2.3.2 Mathematical model

Collocated Covariant Method (CCM) was selected as a solver for the multi-block grid. Essentially CCM is a segregated Navier-Stokes equation solver based on the collocated grid arrangement and covariant velocity projections as dependent variables. The coupling of equations is achieved by the global iteration algorithm, which employs SIMPLE-like procedure and Rhie-Chow like interpolation (PHOENICS). The linear equation solver CCM uses whether LU-, or 2-step Jacobi preconditioned conjugate residuals solver.

2.4 Free surface flow modeling

Most of the three dimensional modeling has been done using a rigid lid assumption. However, it is well known that the water surface has a depression at the separation zone and an elevation near the apex of the open channel junction flow, and this surely influences the flow field (Best and Reid, 1984; Weerakoon and Tamai, 1989, Rhoads, 1996). Although it is necessary to identify the relationship between water surface geometry and the flow field, it is quite difficult to collect actual free surface elevation data for large scale natural channels. One of the methods to trace the free surface geometry is to use the porosity correction concept (Ouillon and Dartus, 1997). The model stores velocities at the cell faces and pressures at the centers. Rigid lid assumption means that the H term in equation 2.4 disappears, but L term does not, and we can still have vertical velocities at the center of the cells. Instead of using the area of the cell face fixed by the grid definition, we

can use modified cell face areas, and let it evolve in response to the dynamics of the solution. Therefore, the fluxes change according to the evolving cell face area.

$$A = \text{porosity} \times \text{cell face area}, \tag{2.14}$$

where

$$\text{Porosity} = 1 + P_s/(\rho g h_c)$$

P_s is the pressure on the surface, g is the gravitational acceleration (m/s^2), and h_c is the surface grid cell thickness. This correction allows the free surface effects to enter the continuity equation by changing the effective discharge through a surface cell where the water surface is elevated or depressed. This correction is carried out when the solution has been obtained with a normal rigid lid treatment. Ouillon and Dartus (1997) used this method to trace water surface geometry around a groyne, and they obtained good agreement with experimental data. This method has also been used successfully at a confluence by Bradbrook et al. (2000a;b).

2.5 Boundary conditions

All mass flow boundary conditions are introduced as linealized sources in the continuity equation, with pressure as the variable. At an inflow boundary, the mass flow is fixed irrespective of the internal pressure. The sign convention is that inflows are positive, and outflows are negative. A fixed outflow rate is fixed by setting a negative mass flow.

It is known that integrating the k-ε models through the near wall region and applying the no-slip condition yields unsatisfactory results (Rodi, 1984). A way to overcome this is the use of wall functions. Wall functions use empirical laws to circumvent the inability in the *k-ε* models to predict a logarithmic velocity near a wall. With these laws, it is possible to express the mean velocity parallel to the wall and turbulence quantities outside the viscous sublayer in terms of the distance to the wall and wall conditions such as wall shear stress, pressure gradient and wall heat transfer. Hence, the wall functions can be used to provide near-wall boundary conditions for the momentum and turbulence transport equations, rather than conditions at the wall itself, so that the viscous sublayer does not have to be resolved and the need for a very fine mesh is avoided (Launder and Spalding, 1974). PHOENICS provides two types of wall functions: Equilibrium log-law wall functions; Non-equilibrium log-law wall functions. The present study adopted non-equilibrium wall functions.

The effect of roughness is taken into account by allowing the roughness parameter E, in the logarithmic law for the near-wall velocity, to vary according to the empirical laws proposed by Jayatilleke (1969) for sand-grain roughness. Details of the mathematical description of the wall-function can be found in literatures (Wilcox, 1998; PHOENICS manual)

3. MODEL VALIDATION

Laboratory experimental data were used to validate the numerical model, and the model was capable of predicting complex flow features of junction flow such as the separation zone and the secondary flow. In particular, the model was validated using the results of Biron et al. (1996a,b)'s experiment and Weber et al. (2001)'s experiment. Similar validation of the numerical model was successfully done by Bradbrook et al. (2001) for the Biron et al.'s experiments.

3.1 Validation of numerical model using the result of Biron et al.'s (1996a,b) experiment

Both the laboratory junction and natural confluence studies have shown that the junction angle and bed discordance play an important role in the flow structure (Mosley, 1976; Best 1986, 1988; Weerakoon, 1990; Best and Roy, 1991; De Serres et al., 1999). Biron et al. (1996a,b) experimented two different bed configurations to study the effect of discordant beds on the confluence fluid dynamics.

3.1.1 Biron et al.'s experimental setup and results

The setup of the experiments is shown in Figure 3.1. The junction angle was 30°, and the width of the main, tributary, and post confluence channels was 0.12m, 0.08m, and 0.15m respectively. The wider post confluence channel corresponds to many field cases where the post confluence channel is wider than the main channel upstream from the junction

(Mosley, 1976; Best, 1987). This widening also avoids a significant increase in the Froude number. The bed and the walls were made of material with smooth surface. The vertical step with a height, h, of 0.03m was put in the tributary channel to model a tributary mouth bar with an avalanche face. The main channel flow depth, Y, was 0.16m, and this produces a ratio of step height to flow depth (h/Y) of 0.19, and a depth ratio (Dr = depth of the tributary/main channel) of 0.81. The details of the experimental setup that are used as a boundary condition for numerical modeling are shown in Table 3.1.

Table 3.1 Flow characteristics for experiments of Biron et al. (1996a,b)

	Mean streamwise velocity U (m/s)		Reynolds number R_e		Flow depth, d (m)	
	Tributary	Main channel	Tributary	Main channel	Tributary	Main channel
Concordant	0.24	0.13	7400	5020	0.16	0.16
Discordant	0.27	0.14	7970	5400	0.13	0.16

The Reynolds numbers were calculated by:

$$R_e = \frac{U \cdot R}{\nu} \tag{3.1}$$

where U is the average velocity in the post confluence channel, R is the hydraulic radius defined by cross-section area divided by wetted perimeter, and ν is the kinematic viscosity.

The measurement of the flow field was done with a DANTEC two component fiber optic laser Doppler anemometer (LDA) (Biron et al., 1996 a,b). Flow field data for downstream and vertical velocities were collected with around 400 measuring points, and Figure 3.2 shows the location of the measuring points. Biron et al. (1996a,b) summarized the effect of

the bed discordance in four of the key flow dynamics regions of confluence (i.e. zone of separation, flow deflection zone, zone of contraction, mixing layer). Table 3.2 shows the summary of the differences.

Table 3.2 Summary of the comparison between concordant bed and discordant bed confluence

	Effects	Concordant bed	Discordant bed
Flow deflection zone	Deflection of the near bed main channel flow	• Up to 35°	• Negligible • Flow in deeper main channel entrained from near the upstream junction corner in the flow separation zone in the lee of the step and routed towards the d/s junction corner
Flow separation zone	Velocity toward the d/s junction corner	•Reduced streamwise mean velocities for both the bed and water surface	• No marked reduction near the bed • No trace of separation zone near bed
	Upstream motion of velocity in separation zone	• Not detected	• Upstream motion vectors are detected in the flow at the depth higher than the step
	Large vertical velocity immediately downstream from the tributary corner	• No significant vertical motion	• Very strong vertical motion (upwelling) destroying the separation zone near the bed.
Flow contraction zone	Acceleration of flow in this zone	•Small zone of acceleration exists for both the near bed and water surface	• Near bed: No marked flow acceleration zone near the downstream junction corner due to destroyed separation zone • Near water surface: The zone of flow acceleration exists
Mixing layer	Peaks of the turbulence intensity	• The peaks are present in the mixing layer between confluence flows • The vertical axis of the mixing layer is perpendicular to the bed • Larger peaks are near the tributary wall at the separation zone	•Deformation of mixing layer with the base of the shear layer being distorted towards the shallower tributary flow • The vertical axis of the mixing layer is inclined towards the shallower tributary

3.1.2 Numerical simulation of Biron et al.'s experiment (1996a,b)

A multi-bock technique with body fitted coordinates is used to generate the grid for both concordant and discordant bed confluence models. The multi-block technique was required to produce the 90° step for the discordant bed model, and body fitted coordinates are used to implement the 30° junction angle. The main block is constructed and then the block for the tributary channel is connected to the main block. The cells are mostly cubic with 90° angles, except the cells in the area where the two blocks are joining, so the grid lines were adjusted to have cell angles as close to 90° as possible. Grid skewness was checked, and all the cells met the condition that the angle of intersection between grid lines must fall into the range of 45 to 135 degrees.

The grid dimensions are 70x24x45 and 70x24x38 for the concordant bed and the discordant bed respectively, and the plan view of the grid is shown in Figure 3.3. The discordant bed model has slightly less cells than the concordant model, since the tributary has a smaller volume. The upstream bend of the tributary was provided for both models to simulate the effect of the bend on the flow field. The upstream curvature has been shown to have an impact on the simulation (Lane et al., 1999).

The RNG k-ε model, non-equilibrium log-law wall functions, and porosity based free surface model that were explained in chapter 2 were used to investigate the flow field and to trace the geometry of the free water surface. Numerical tracers of different concentrations were also implemented as inlet conditions to study mixing processes.

Proper inlet conditions were required, so separate straight channel models with uniform inlet conditions that correspond to the values in Table 3.1 were prepared for both the main and the tributary channels. The results of the simulations at the cells located at the outlet were transferred to the main confluence models in order to be applied as the inlet conditions. Both of the models converged for all the variables with residual errors of less than 1.0 %.

3.1.3 Comparison

The downstream and vertical velocity data were collected in the laboratory experiments, so the comparison is done for these two variables. The values for the downstream velocity and the vertical velocities were extracted from the simulation corresponding to the original (x, y) coordinates from the laboratory experiments. However, the center of the cell volume where the vectors are stored does not necessarily coincide with the exact coordinate of the sampling point used from the laboratory experiments, so there could be slight errors in sampling coordinates. If the coordinates of the cell center was too far off from the exact coordinates of the measuring points from the experiments, interpolation was used between adjacent cells to minimize the errors.

Concordant bed model

Two simulations were tested for the concordant bed case. First, the free surface approximation (section 2.4) was not used to test the effect of this approximation, and then

it was activated in the second simulation. The improved predictability using the free surface approximation was previously reported by Ouillon and Dartus (1997) and Bradbrook et al. (2001).

Figure 3.4 shows the results of the second simulation. The plot of the vector composed of the vertical and lateral velocities, and the contour plot of the downstream velocity are shown. A very weak single helical cell formation is shown at the bottom of the channel, and this helical cell weakens rapidly going downstream. The flow accelerates as the flows from both tributaries merge around section **B** (Figure 3.4).

The correlation values are given in Table 3.3. They show that the first simulation not using free surface approximation produced a poor prediction for both downstream and vertical velocity compared to the second simulation with free surface approximation. However, the downstream velocity predictions generally agree well with the measurements for both simulations, and the correlation with the vertical velocity is poor for both simulations in spite of the slight improvement in the second simulation. Ignoring 5 outlier points labeled **L** on Figure 3.5a and the 5 points with black mark on Figure 3.5b, the correlation values with the downstream velocity and vertical velocity are improved from 0.83 to 0.89 and 0.30 to 0.61, respectively. The predicted downstream velocities are higher than observed values in this area. On the other hand, the predicted vertical velocities are lower than observed values. These points are located in a small zone around 4cm downstream of the downstream junction corner and 0.7cm from the wall and are therefore in the separation zone where rapid changes in velocity occur. Therefore even a slight difference between the

cell center and the (x, y) coordinate of the measuring points can give rise to significant differences in this zone.

.

Table 3.3 Correlations for concordant bed experiments of Biron et al. (1996 a,b)

	Downstream velocity	Vertical velocity
Without free surface approximation	0.68	0.11
With free surface approximation	0.83	0.30
Free surface without outliers	0.89	0.61

The contour plot of the downstream velocity from the laboratory measurements and the simulation for concordant bed is shown in Figure 3.6 for Zd = 0.06 and 0.81, where Zd is the non-dimensional vertical distance from the main channel bed (Zd=z/d, where z is the height above the bed, d is flow depth). Downstream velocity contour for both experiment and simulation show good agreement, and the flow pattern does not change significantly from the bed to the water surface. The penetration of flow from the tributary is noticeable in both results. The flow accelerates at the downstream junction corner and the zone of stagnation is identifiable with low downstream velocity at the junction apex. The separation zone at the downstream junction corner is obvious from the laboratory measurements, but the model underpredicts the size of the zone, and the predicted velocities are higher than the measured ones.

The poor prediction of the vertical velocity (Table 3.3) can be due to the errors from both predicted and measured velocities, since the magnitude of the vertical velocity was very

small compared to the downstream velocity (Figure 3.5b). The range of vertical velocities from the simulation was from –0.22cm/sec to 0.85cm/sec, and it was from –0.16cm/sec to 1.7 cm/sec from the experiments. Another possible explanation of these low correlation coefficients for vertical velocity is again due to small difference between cell centers and coordinates of measured points. The region with relatively high vertical velocity was located near the bed area close to the junction corner for both the experimental results and the simulation.

The predicted water surface profile from the simulation for concordant bed is shown in Figure 3.7. The model was able to locate the zone of the superelevation corresponding to the stagnation zone, and the depression at the separation zone (in blue). The total variation of water surface elevation was only 0.6mm. Considering the simplicity of this water surface approximation method and the low computational cost, it has proven to be effective.

To investigate the problem of the water surface further, the predicted water surface profile was used as the physical boundary of the model. As mentioned in section 2.4, most of the three-dimensional models use the 'rigid-lid' assumption. One might measure the detailed water surface profile, and use it as the actual geometry of the grid. Here, the predicted water surface profile cannot be validated since no data are available. However, it was used to construct the mesh of the concordant bed simulation. All the conditions for the simulation were kept the same, but the free surface approximation routine was deactivated. The correlation coefficient for the downstream velocity has improved to 0.93, and it was

0.4 for the vertical velocity. It indicates that detailed measurement of the water surface topography may be required to achieve more accurate and reliable predictions from the numerical model. However, the benefit of this procedure is offset by the increased difficulty in grid generation. The time required to generate the grid was significantly increased. Hence, the use of this procedure requires caution considering the fact that acquiring reliable data of the water surface geometry from the laboratory or field might also be difficult and costly.

Discordant bed model

The RNG k-ε model, non-equilibrium log-law wall functions, and free surface approximation were also used for the discordant bed case, as well as the multi-block technique to generate the mesh. The grid dimension of the main channel was identical to the concordant bed model, and the block for the tributary channel that has a step height of 0.03m was linked to the main channel block.

The contour plot of predicted water surface profile from the simulation is shown in Figure 3.8. The water surface profile is similar to the result from the concordant bed confluence simulation. However, the predicted depression in the separation zone is larger and deeper than in the concordant bed confluence. Figure 3.9 shows the vector plot of the lateral and vertical velocity components and the contour plot of the downstream velocity at chosen cross-sections predicted from the simulation. A stronger single helical cell develops, and the contour of the downstream velocity is more complex than the results from the

concordant bed with a distortion of the zone of higher velocities towards the shallow channel close to the bed. This corresponds to the observation of Biron et al. (1996b).

The correlation values for the discordant bed experiment were 0.88 and 0.78 for downstream velocity and vertical velocity, respectively. These values are higher than the result from the concordant bed simulation, particularly for the vertical velocity. The flow separation, which is represented with very low values of the downstream velocity from the experiment labeled **M**, is not predicted from the simulation (Figure 3.10a). The predicted downstream velocities in the zone was higher, as with the concordant bed experiment (Figure 3.10a). The vertical velocities are much larger than for the concordant bed experiment due to the existence of the step, and the correlation between the simulation and the experiment is improved significantly (Figure 3.10b). However, the magnitude of the predicted vertical velocities downstream of the tributary entrance near the tributary side bank is under-predicted.

The contour plot of the downstream velocity from the laboratory measurements and the simulation for discordant bed is shown in Figure 3.11 for Zd = 0.06 and 0.81. The contour of the downstream velocities for both the experiment and simulation show relatively good agreement. The clear difference in downstream velocity pattern between the channel bed and the water surface observed from the experiment is well predicted from the discordant bed simulation.

3.2 Weber et al.'s experiment (2001)

The previous validation shows that the model is capable of predicting the flow field accurately. However, free water surface geometry data was not available for Biron et al. (1996 a, b)'s experiment, so the model's capability to track the actual water surface height was tested using available data from Weber et al.'s experiment (2001). Weber et al. (2001) also provided detailed flow field data for several sets of flow conditions. The validation of the model was carried out using one of the flow condition $q^*=0.75$, where q^* is defined as the ratio of the upstream main channel flow to the total flow.

3.2.1 Numerical simulation of Weber et al (2001)'s experiment

Multi-bock technique with boundary fitted coordinates was also used instead of Cartesian coordinates to have a similar grid condition than that of Biron et al.'s simulation. However, the junction angle is 90°, so the conditions for mesh mentioned in the section 2.3 were easily met. Figure 3.12 shows the grid for the 90° open channel confluence for Weber et al. (2001)'s experiment. The grid dimension is 74 x 32 x 41. Grid lines are denser close to the walls and the junction corner as shown in Figure 3.2. The RNG k-ε model, non-equilibrium log-law wall functions, and porosity based free surface model were used.

3.2.2 Comparison

The flow field was compared visually, and it showed good agreement. The non-dimensional separation length (distance form junction corner/ width of main channel) was also compared near the bed and near the surface (Figure 3.13). The separation lengths observed were 1.35 and 1.1 for near the surface and near the bed, respectively. The values from the simulation are 1.25 and 1.0 respectively as shown in Figure 3.13. The model therefore underestimates this length with an error of less than 10 %.

A total of 375 points were used to collect the water surface topography in the experiment, and the water surface height data from corresponding coordinates from the simulation were compared to these values. The correlation coefficient is 0.95, representing a very good agreement. Three-dimensional topography of the free surface was constructed using the data from the experiment and the simulation in Figure 3.14.

3.3 Summary of validation

The numerical model has been shown to predict the flow field and water surface geometry accurately, even with the complex features of confluence flow. Two separate laboratory data sets with a low and high junction angle were successfully simulated. Accurate geometry shape of the domain was achieved effectively by the use of curvilinear coordinates with a multi-block technique, and RNG k-ε model, and porosity based free

surface model improved the accuracy of the model. The model can therefore be applied confidently to more complex natural confluences.

4. MECHANICS OF FLOW AT A NATURAL CONFLUENCE

There has been a number of studies on stream junction flows investigating the complex flow characteristics and mixing process of natural river confluences (Roy and Bergeron, 1990; Ashmore et al., 1992; Biron et al., 1993a,b; Bristow et al., 1993; Rhoads and Kenworthy, 1995; Gaudet et Roy, 1995; McLelland et al., 1996; Rhoads, 1996; De Serres et al., 1999; Rhoads and Sukhodolov, 2001). These studies were able to identify key features such as the three-dimensional flow field, the helical cells, the turbulent characteristic in the mixing zone, and the strong upwelling close to the avalanche face in the case of discordant bed confluences. However, it is still difficult to collect large quantities of reliable data in such a complex flow using available methods of field measurements. Most of the field investigations were based on two-dimensional data except McLelland et al. (1996), De Serres et al. (1999), and Rhoads and Sukhodolov (2001) who used three velocity component measurements to obtain data. Although McLelland et al. (1996) and De Serres et al. (1999) collected three-dimensional flow field data, these were not measured simultaneously. They used two-dimensional current meters to collect three-dimensional flow data. For example, De Serres et al. (1999) used an array of two-component Electromagnetic Current Meters (ECM). They measured longitudinal and vertical velocities, and then the mounting rods were rotated 90° to measure lateral and vertical velocities. This method is effective, but it can introduce unnecessary errors. Rhoads and Sukhodolov (2001) provided true three-dimensional flow fields measured with an Acoustic Doppler Velocimeter. However, all the field studies are limited by the number of measuring points that can be sampled while flow conditions remain stable. A final

limiting factor is the fact that data could not be collected simultaneously for the whole domain.

Despite these intensive field studies, there is still a debate over the nature and the cause of observed flow structures. One of the unsolved problems is the existence of the two counter rotating helical cells. Two dimensional flow measurements of Ashmore et al. (1992), Rhoads and Kenworthy (1995, 1998), and Rhoads (1996) and three-dimensional measurements of McLelland et al. (1996) and Rhoads and Sukhodolov (2001) have confirmed the existence of the two counter rotating helical cells which were compared to two meander bends placed back to back (Ashmore, 1982; Ashmore et al.,1992; Bridge, 1993; Rhoads and Kenworthy, 1995). However, other studies show that it is not a feature of all confluences (e.g., De Serres et al., 1999). It has been recognized that pronounced bed discordance between the tributaries characterized by the avalanche face at the mouth of the shallower tributary is responsible for the absence of the two counter rotating helical cells (Bradbrook et al., 2000a).

To close the above debate, a systematic approach is required to understand the controlling factors such as bed shape of confluence and momentum ratio between the main channel and the tributary flows. However, unlike a laboratory confluence, each field confluence has its specific geometry and flow conditions that vary with time. This makes such a systematic study difficult. Researchers have begun to use numerical models to investigate complex three-dimensional flow structure in field confluences in a variety of environments (Weerakoon and Tamai, 1989; Weerakoon et al., 1991; Lane et al., 1999; Bradbrook et al.

2000a,b). Numerical modeling can help researchers obtain a better understanding of the confluence dynamics such as shear stress at the river bed, pressure, and free surface height which are difficult to get from the conventional field or laboratory measurements. Furthermore, by changing boundary conditions such as the inflow rate, the effect of changes can be readily implemented in numerical modeling.

The data for the confluence of the Bayonne-Berthier Rivers, 90 km NNE of Montreal, Quebec were used in this study. The data from this site also have been used successfully in other numerical models (Lane et al., 1999 and Bradbrook et al., 2000).

4.1 The Bayonne-Berthier confluence

Both the Bayonne and Berthier rivers are sand bedded (D_{50}=0.23 and 0.31mm for the Bayonne and Berthier rivers, respectively), and form a confluence with a junction angle of approximately 65° (Figure 4.1). The average channel width is about 8m. Before reaching the confluence, both rivers have a curvature upstream, and the channel remains relatively straight after the junction. The Berthier is shallower than the Bayonne with a depth ratio (depth of tributary/depth of main channel) of 0.26 at the lower flow condition and 0.66 at high flow condition (Biron et al., 1993b). A tributary bar ends at an avalanche face and a bar exists at the downstream corner of the junction (Figure 4.1).

As seen in Figure 4.2, Bayonne River carries a high-suspended load coming from agricultural land usage upstream. This provides a visual marking of the turbulent shear

layer between the two merging rivers. De Serres et al. (1999) collected morphological data at 14 cross sections spaced at 2m intervals and a lateral spacing of 0.5m (Figure 4.3). Details of the measuring method and measured data are given in De Serres et al. (1999). Originally, the velocity field data were collected for seven flow conditions using two-dimensional ECMs that were rotated to provide three-dimensional measurements. Two sets of data representing a high flow condition and a low flow condition were chosen for this study to compare the effect of discordance in a natural confluence. The flow characteristics of the Bayonne River and the Berthier River for low and high flow conditions are given in table 4.1.

Table 4.1 Flow characteristics at Bayonne- Berthier confluence (from De Serres et al., 1999)

	D_{Bay} (m)	D_{Ber} (m)	D_r	U_{Bay} (m/s)	U_{Ber} (m/s)	Mr	Re_{Bay}	Re_{Ber}
Low flow (October 2)	0.87	0.45	0.52	0.14	0.26	1.79	74000	73000
High flow (October 12)	1.24	0.81	0.65	0.48	0.22	0.18	137200	113000

Mr denotes the momentum flux ratio between the Berthier and the Bayonne River. D is the mean flow depth, U is the mean velocity, Re is the Reynolds number, Dr is the depth ratio ($D_r = D_{Ber}/D_{Bay}$), and the subscripts Bay and Ber refers to the main channel (Bayonne) and the tributary (Berthier), respectively.

The most apparent differences between the low and high flow condition are the depth ratio, D_r, which gets close to unity at high flow condition (relative decrease in the importance of bed discordance) and the domination of the Bayonne flow at high flow (much faster velocity).

4.2 Numerical simulation

Bradbrook (1999) performed a grid dependency test using the Bayonne-Berthier confluence model for the low flow condition identical to this study. She chose a grid of 82 x 56 x 12 covering a domain of 30m x 20 m x 0.75 m. The present study also adopted a similar grid dimension (85 x 55 x 12) for both low and high flow condition simulations. The grid was generated using the multi-block technique to isolate the areas where the grid angles and spacing are problematic. The isolated blocks were modified several times to satisfy the grid conditions which are explained in section 2.3 such as cell angles as close as possible to 90° and spacing to control the cell aspect ratio. The geometry of the confluence was reconstructed using the data of 14 cross-sections provided by Biron who was one of the authors of De Serres et al. (1999)'s study. Figure 4.4 shows the geometry of the cross-sections. The difficulties in generating a suitable grid came from the shape and the location of the cross-sections. The cross-sections are parallel to each other, but the flow direction is not necessarily perpendicular to the cross sections. This is especially a problem in the junction apex area where the grid lines intercept the cross-section at an angle close to 30°. The other problem has arisen at the cross-sections where the bed height decreases very steeply towards the banks. This made it difficult to control the grid angles. Furthermore, it was difficult to control the cell aspect ratio in the region near both side banks where the water depth is very shallow. This problem, however, is not related to the confluence but to the modeling of all natural rivers. Several grid types had to be tested before running a simulation. The model used the RNG k-ε model, non-equilibrium log-law wall functions, and the porosity based free surface model used in the validation models.

4.3 Low flow (October 2)

As shown in Table 4.1, the momentum flux ratio, Mr, is 1.79. This indicates that the tributary is dominant. The discordant effect is strong with a depth ratio (Dr) of 0.52.

4.3.1 Simulation of approaching rivers (Bayonne River and Berthier River)

As mentioned previously, the Bayonne River and Berthier River have a curvature upstream of the junction. This effect had to be considered to provide accurate boundary conditions for confluence simulations. The number of velocity sampling points was 36 at the cross section of 26.5m (Figure 4.3), and the coordinates of these points are shown in Figure 4.5. The density of the measuring points is very low so that they could not be used directly as an inlet condition, especially for the Berthier River side. Also, the effect of the curvature of both the Bayonne River and the Berthier River is expected to influence the flow pattern of the river prior to the merging. Using uniform inlet condition in the main confluence simulation would not be realistic.

Separate simulations to predict the flow pattern for the Bayonne River and Berthier River were required for both high and low flow. However, there were no bed topography data available for the Bayonne and Berthier rivers upstream of the junction. Hence, the cross-section at x =26.5m was divided into two segments along AB in Figure 4.5. These two sections form the cross-sections of the grids for the Bayonne and Berthier Rivers. The

curvatures and locations of the two rivers were approximated from photographs and a map of the region. Although the river beds of the two rivers are not strictly speaking uniform, the grids were constructed with uniform cross-sections due to the lack of precise bed topography data. Figure 4.6 shows the grids for each upstream section. Inlet conditions were specified using the mean velocity in each channel (Table 4.1) and a turbulence intensity of 15 %.

The simulations using **abcd** and **efgh** (Figure 4.7) were carried out first, and then the predicted flow fields with three velocity components and turbulence quantities at **cd** and **hg** were used as inlet conditions at **ij** and **kl,** respectively (Figure 4.7).

4.3.2 Results of the tributary simulations

Figure 4.8 shows the mean flow pattern predicted from the simulations for the Bayonne River and the Berthier River. Four different cross-sections for each simulation are shown. Note that the vertical scale is 7 times the horizontal scale in these sketches. The plots display the velocity vectors formed by the vertical and lateral components. The vector plots show that the secondary flow is intensifying going downstream in both rivers. The length of the channel measured from the centerline for the Berthier River simulation along **pq** is 2.5 times the channel width **dd** (Figure 4. 8 a)). Considering the relatively short length of the Berthier River simulation, it is clear that the effect of the curvature plays an important role in characterizing the flow pattern. Although the result of the flow pattern may be prone to errors due to the use of approximated geometrical data, one might expect improved

predictions for the main confluence simulation using realistic inlet conditions with a curvature as in the field streams.

4.3.3 Confluence simulation

Figure 4.9 shows the grids used for the confluence of October 2 simulations. In Figure 4.9a, the grid is similar to that in Bradbrook (1999)'s study, and Figure 4.9b is a grid using smoother curves at the junction area. Clearly, grid 2 allows a better control on the cell angles in the junction area. The tributaries in grid 1 are extended approximately 12m upstream from the first cross-section at the confluence apex. The length of the tributaries in grid 2 is approximately 5m. Three simulations were conducted in order to compare grid 1 and grid 2. The setup for each simulation is shown in Table 4.2.

Table 4.2 Setup for low flow simulations

Simulation	Grid	Inlet condition	Wall function	Free Surface	Turbulence model
(a)	1	Uniform	Yes	Yes	k-ε RNG
(b)	1	From separate simulation	Yes	Yes	k-ε RNG
(c)	2	From separate simulation	Yes	Yes	k-ε RNG

All the three simulations use the non-equilibrium wall function and k-ε RNG turbulence model. The free surface approximation was also used. Simulation (a) used uniform inlet conditions from Table 4.1 without the use of the inlet bends 1 and 2 (Figure 4.7). The inlet conditions obtained from the simulations from section 4.3.2 which included the bends 1 and 2 (Figure 4.7) were used for simulation (b) and (c). The use of a longer length of the extended tributaries of grid 1 was to obtain fully developed flow field near the junction

apex for simulation (a) using uniform inlet condition.

4.3.4 Results

4.3.4.1 Correlation

From the apex of the junction to a downstream distance of 26.5 m (Figure 4.4), five cross sections were surveyed, with five or six velocity profiles taken along each section (De Serres et al., 1999). The total number of velocity sampling points was approximately 150. The flow field data from these points were compared with the values from the simulations. The calculated correlation, the measured and the predicted values of u, v, w and the k values are shown in Table 4.4. The highest correlation value is found for simulation (c), where inlet conditions are generated from the separate simulation considering the effect of curvature of both the tributaries. The controlled grid angles in the apex area seem to improve the correlation coefficients of the simulation. Judicial adjustment of the gridlines to ensure orthogonality of the grid structure improved the result of the simulation. The improvement in the simulated results is traced to the reduction in the adverse effects of the skewness of the cells.

The correlation for the downstream velocity component is slightly higher that that of Bradbrook's (1999) simulation. She used tributary channels with rectangular cross-sections, and calculated the distribution of velocity parallel to the channel banks and of turbulence quantities assuming the flow was fully developed (Bradbrook, 1999).

However, unlike the present study, the effect of the curvature of the tributaries was not considered in that simulation.

Table 4.3 Correlation coefficients for low flow condition simulation

Simulation	U	V	W	*k*
(a)	0.75	0.79	-0.115	-0.002
(b)	0.782	0.817	-0.109	-0.005
(c)	0.80	0.83	-0.01	0.34
Bradbrook (1999)	0.71	0.83	-0.12	0.35

Based on these results, the rest of the analysis will rely on simulation (c). The model predictions for both the downstream and lateral velocities are good (Figure 4.10 a, b). However, the correlation for vertical velocity is low (Table 4.3). This can be due to the fact that the field measurements from De Serres et al. (1999) show high vertical velocity with high temporal fluctuations in the shear layer, but the result of the present simulation did not show any such flow pattern (Figure 4.10 c). The high temporal fluctuation of velocity in the shear layer of the Bayonne-Berthier confluence is well illustrated in Figure 4.11.

4.3.4.2 Velocity vectors in the horizontal plane

Figure 4.12 shows the velocity vectors of the downstream and lateral velocity components across a horizontal plane at the surface and at the bed measured in the field and predicted by the simulation. The velocity vectors from the field measurements show a distinct

difference in the orientation for the near bed and near surface vectors. At the cross-section X=26.5m, the flow directions of the bed and surface vectors for the Bayonne side are almost parallel (Figure 4.12c). However, this is not true for the Berthier side. In fact, here (Berthier side), the flow at the bed is slightly towards the right bank looking downstream at the bed. It is almost parallel to the bank at the surface. The flow is also faster in the center of the channel for both the Bayonne and Berthier at the junction entry. The zone of low velocity at the apex is identifiable. These features are accurately predicted from the simulation (Figure 4.12a, b).

At X=20m, there is a zone of relatively lower downstream velocity in the center of the channel. This zone corresponds to the high turbulent energy zone. This zone is predicted in the simulation, but the location of the zone at the surface is slightly closer to the Bayonne side. The near-bed vectors are oriented more towards the Berthier side, and this is also the case for the predicted flow pattern.

At X=15m, the zone of reduced velocity becomes less pronounced in the measured velocity, and this is similar to the predicted velocity pattern. The flow pattern over the downstream junction corner bar near the bed shows divergence of flow at the surface and bed in the field measurements. The simulation was able to predict this flow pattern precisely (Figure 4.12 a, b). The width of the cross-section increases where the downstream junction corner bar is located, and the simulation shows the development of a small separation zone in this area, which is not obvious in field measurements. This is probably due to the lack of field data close to the Berthier bank.

At X=7.0m, the velocity vectors near the surface are almost parallel to the banks. The near-bed vectors are oriented towards the Berthier side bank, particularly close to the Bayonne side (Figure 4.12c). The simulation shows a similar flow pattern. However, simulated velocity vectors at the surface close to the Bayonne bank are lower. Once again, the comparison with field data is limited by the absence of sampling points very close to the Bayonne bank.

At X=0.0m, the mean bed and surface vectors are close to being parallel to each other in field data as well as in the simulation. At both the surface and the bed, the velocity appears to be slightly smaller at the center of the stream. The flow pattern predicted by the model is similar, but the magnitude of the reduced velocity in the middle is less.

Except for the fact that the reduction of the velocity in the center section is not as marked as in field data, the model is reasonably accurate, as was shown by the correlation values.

4.3.4.3. Velocity vectors, contour, and turbulent kinetic energy at cross-sections

The downstream velocity pattern is similar for both the model prediction and the field measurements (Figure 4.13). At X=26.5m, the direction of the flow is mostly towards the junction apex in the Berthier River. A low velocity stagnation zone, measured in the field, is also identifiable in the model prediction (Figure 4.13). The measured velocity vectors near the bank of the Bayonne River have a smaller vertical component compared to the

component predicted by the model. Model predictions show the velocity vectors are oriented towards the water surface, whereas this is not apparent in field measurements.

At X=20.0, the most identifiable flow pattern from the field measurements is the flow towards the surface in the shear layer. The model prediction matches the lateral direction of the velocity vectors reasonably well. It shows the upward movement of the flow in the middle, but there is also a downward movement of the vectors on the Berthier side. This downward flow direction is not identified in the field measurements.

The plot of velocity vectors at X=15.0m from measurements also shows the upward flow in the middle, but the simulation shows a downward flow direction at the same location. The simulation shows the development of a single helical cell. This is not identified from the field measurement data clearly. This tendency of upward flow direction continues downstream, but the model predictions at X=7.0m and X=0.0m show flow patterns that are similar to field measurements for downstream velocity contours.

Figure 4.14a is the plot of non-turbulent kinetic energy for the above cross-sections. Turbulent kinetic energy is divided by U^2_{max} (where U_{max} is the maximal downstream velocity for October 2). U_{max} value measured was 0.419m/s which is located at X=0.0m (De Serres et al., 1999). The field observations show that high turbulence kinetic energy corresponds to zones of low downstream velocity in each cross-section in Figure 4.11. The core of high turbulent energy extends down to the bed in the upstream sections, and then it moves away from the bed towards the water surface further downstream in the field

measurements. However, this upward movement of the high turbulence energy zone is not observed in the simulation. Figure 4.14 shows that the zone of high turbulence intensity is widening downstream both in field data and in the simulation. Another important feature is the distortion of the shear layer, particularly at X=15.0m. This is well depicted in the simulation. Although the simulation predicts high turbulent kinetic energy in the shear layer in the middle, the intensity is much lower than that measured in De Serres et al. (1999).

The predicted free surface profile is shown in Figure 4.15. It shows that the water surface elevation on the Bayonne side is higher than the Berthier side. Although the variation of water surface height is only about 2cm, the prediction shows that it has a complex geometry. The main features do corresponds to recent measurements of the water surface for a similar flow condition (Biron et al., 2002)

4.4 High Flow (October 12)

The momentum flux ratio, Mr, is 0.18 at high flow, and the avalanche face has receded and forms an extension of the right bank of the Bayonne River looking downstream. This shape of the tributary bar and the higher depth ratio (Dr=0.65) make the effect of bed discordance less significant, compared to the low flow condition.

4.4.1 Simulation of approaching rivers

The same procedure used in low flow simulation is applied. In order to obtain proper inlet conditions for the main confluence simulation, two grids for the Bayonne River and the Berthier River were constructed. The cross section **aa'** (Figure 4.16) was divided into two segments. Those sections formed the cross sections for the two incoming rivers. The simulations also use the non-equilibrium wall function and the k-ε RNG turbulence model. The inlet velocities are 0.48m/s and 0.22m/s for the Bayonne river simulation and the Berthier river simulation, respectively. Figure 4.17 shows the grid of the Bayonne River and the Berthier River and the secondary flow pattern represented with the lateral and vertical velocity vectors at the cross sections along **aa'** and **bb'**. The velocity field of the three velocity components and turbulent quantities at **aa'** and **bb'** were used as inlet conditions for the main confluence model.

4.4.2 Confluence simulation

Figure 4.18 shows the grid used for the confluence of October 12 simulation. The grid was generated using smooth curves near the junction area, since the simulation for low flow condition demonstrated that this type of grid produces a better prediction. The field survey was conducted for three cross sections for this flow condition (Figure 4.16).

The velocity vectors composed of downstream and lateral velocities are shown in Figure 4.19. The velocity vectors near the surface and near the bed at zone A show that there are

orientation differences at the bottom of the avalanche face in the field confluence (Figure 4.19c). This feature was precisely predicted in the simulation (Figure 4.19a,b). The simulation correctly shows that the magnitudes of the velocity vectors are significantly reduced on the right side looking downstream of the confluence. Field measurements show a zone of reduced velocity vectors in the middle of the confluence at X=15.0m and 0.0m (Figure 4.19c). The model predicted this zone near bed (Figure 4.19a), but it is not obvious near the surface (Figure 4.19b).

The simulation also shows the development of a recirculation zone at X=0.0m where the river expands. However, this is not monitored in the field measurements.

Figure 4.20 shows the contours of the downstream velocities and velocity vectors composed of v and w. The downstream velocity contour pattern for all three sections matches well with the field measurements including the stagnation zone at the junction. The downstream velocity is faster towards the Bayonne side going downstream. At X=15.0m, the model prediction shows some upwelling in zone **B**. This trend is similar to the field observation. The zone of flow upwelling is also detected in the field further downstream at X=0.0m, but this it is not obvious from the simulation result. However, the magnitude of the upwelling is much smaller compared to the low flow condition. The result from simulation does not show the development of a helical cell that was one of the features from the low flow simulation.

The contour plot of turbulent kinetic energy (Figure 4.21) from the simulation shows that the generation of turbulence is high in the center of the confluence at X=15.0m, where the lateral velocity gradient is high. The magnitude and size of the high turbulence zone decreases moving downstream. The simulation shows also a very high turbulence zone at X=0.0m of the Bayonne side. This is not a feature noticed from the field survey and may be due to a local contraction on the Bayonne side just upstream of the cross-section at X=0.0m (Figure 4.16). Figure 4.22 shows the predicted water surface elevation from the high flow condition simulation.

5. MIXING PROCESS AT CONFLUENCES

In the previous chapters, the effect of a discordant bed on the flow dynamics of confluences has been studied using the three-dimensional numerical model. The merit of the three-dimensional numerical model has been shown as a tool to investigate the complex flow structure not only in simple laboratory confluences but also in natural confluences with a complex geometry. This chapter extends the use of the model further to study the mixing characteristics in confluences.

As seen in chapter 1, there have been several studies on confluences due to the important environmental implications of river confluences for pollutant dispersion in a river system. The conclusions of studies using prismatic channel confluences with discordant bed in the laboratory is that the distortion of the mixing layer towards the shallow tributary enhances the mixing process (Best and Roy , 1991, Biron et al., 1996 a, b). Gaudet and Roy (1995) studied three natural river confluences to verify the role of discordance at confluences on river mixing. The studied sites include the Bayonne-Berthier confluence that has a bed discordance characteristic similar to the laboratory experiment of the discordant bed confluence (Biron et al., 1996a, b). Their study also supports the enhanced mixing due to the discordant bed configuration of confluences. They measured the electrical conductivity to trace the mixing pattern at cross sections located at distances ranging from 0.5 to 50 times of channel width. They measured the confluence characteristics for different flow conditions. At low flow conditions, the height difference between the beds relative to the mean flow depth is more important, so that the effect of discordance is more dominant. The

width to depth ratio is also higher for the low flow condition. The result shows that the high width to depth ratio leads to a higher mixing rate. Mixing between the confluent rivers is almost completed in a distance close to 25 times the channel width downstream from the junction in their study.

This chapter examines the results from the simulations using a numerical tracer to predict the mixing pattern for both laboratory and natural confluences. Additional simulations were performed for longer distances downstream of the confluences.

5.1 Mixing processes at laboratory confluences

The results from the original simulation as well as additional simulation for distances up to 55 times the channel width are presented to study the importance of the enhanced mixing process created by bed discordance.

5.1.1 Comparison of mixing processes between different bed configurations

Different concentrations of 0.0 and 1.0 are applied as the inlet conditions for the tributary and the main channel, respectively to predict the mixing rate of a pollutant. The pollutant is assumed to be neutrally buoyant and conservative. As such, it does not influence the mean density field.

The mixing layer created by the merging two streams is characterized by increased turbulence intensities. Biron et al. (1996 a,b)'s experiments show distinctly different patterns of turbulence intensity distribution for concordant bed and discordant open channel confluences.

The peaks of turbulent intensities are associated with the mixing layer between two merging streams. Figure 5.1a shows the contours of turbulent kinetic energy (ke) values for selected cross-sections for the concordant bed confluence. Large ke values are found at the center of the channel and close to the tributary wall, where a separation zone is present. For the concordant bed, the mixing layer immediately downstream of the junction is nearly perpendicular to the bed, and this pattern is maintained downstream without significant change. Figure 3.4 showed a weak helical cell developing at the bottom of the channel near the wall of the tributary side, and this slightly distorts the base of the mixing layer inwards towards the wall of the tributary side. However, this distortion is minimal. Figure 5.1a also shows the contour plots of concentrations from the concordant bed confluence simulation. The mixing interface is vertical at the center of the channel, and it remains this way further downstream except for the minor inward movement at the bottom of the channel towards the wall of the tributary channel side. This pattern follows the ke pattern at the center of the channel. The rate of the mixing interface expansion is relatively low as the flow proceeds downstream.

In the case of a discordant bed, the result from the simulation shows the distortion of the mixing layer represented by the high turbulent kinetic energy (Figure 5.2a). Figure 5.2b

shows the greatly enhanced mixing in the presence of bed discordance with the clear distortion of the mixing interface. As seen in Figure 3.9, the flow from the channel below the step is entrained below the step and a narrow zone of upwelling near the tributary wall immediately downstream of the step is formed. Figure 5.3 shows the plot of streamlines close to the step. Streamlines (4), (5), and (6) start from the bed of the deeper channel, and the upwelling flow is mostly from the deeper channel. The flow from the main channel below the step almost reaches the water surface near the tributary wall. The remaining of the upwelling flow is from the flow from the tributary that arises from the bed after reattachment in the leeward side of the step as shown by streamlines (1), (2), and (3). This flow pattern distorts the mixing layer and enhances the mixing rate. The base of the shear layer is distorted towards the shallow tributary flow. This pattern was also observed in the laboratory experiment with turbulent intensity measurements (Biron et al., 1996b). The magnitude of ke values from the discordant bed simulation is clearly much higher than in the concordant bed simulation.

Figure 5.4 presents the comparison of the mixing rates between concordant bed and discordant bed confluences using the plot of the standard deviation values for the pollutant distribution from the simulations. The standard deviation values were calculated using the concentration values taken from each cell of a cross-section. Each cross section has 24 x 22 cells. The length of the channel from the junction apex is about six times the channel width, and the value of standard deviation is reduced from 0.37 to 0.26 (30%) for the discordant bed confluence within a distance of 5 times the channel width. On the other hand, the value has only decreased from 0.42 to 0.38 (10%) for the concordant bed

confluence. It clearly indicates that the geometry of confluence characterized by bed discordance significantly enhances the mixing process.

5.1.2 Mixing process of extended confluence simulation

The original downstream extent of the laboratory confluence grid (1.5m) was short, as this corresponds to the surveyed section in Biron et al. (1996a,b). This also limited the computational expense to a reasonable value. The post confluence length for both concordant bed and discordant bed confluences was about 5 times the channel width. However, it is desirable to investigate the mixing process for longer distances downstream to understand the significance of the enhanced mixing process of the discordant bed confluence.

Additional grids were prepared to add a length of 7.5m to the channel, and this corresponds to about 50 times the post confluence channel width. The predicted values of the velocity field, turbulent quantities, and the concentration values from the cells at the outlet of the confluence simulations were stored and used as the inlet condition for this extended channel simulations.

The prediction from the extended channel simulation for the concordant bed confluence is shown in Figure 5.5. The flow pattern presented with the velocity vector plot and the contour plot of downstream velocities indicates that the weak helical cell shown in Figure 3.4 is no longer visible. The shear layer represented with high ke values is no longer

apparent. It also shows that the mixing process is getting slower as the flow travels downstream. The range of concentration (C1) value at section E is from 0.23 to 0.68, and the expected C1 value assuming complete mixing for discordant bed confluence simulation is 0.55. The mixing process is therefore not completed at a distance of 50 times the channel width.

Figure 5.6 shows the result from the extended channel simulation for the discordant bed confluence. The velocity vector plot shows that the upwelling and secondary circulation still exist although they weaken rapidly proceeding farther downstream. The C1 values at section E in Figure 5.6 range from 0.37 to 0.58, and the plot of contours of C1 indicates that the mixing process is almost completed. Figure 5.7 compares the mixing rate between concordant and discordant bed for the extended channel simulations using standard deviation. The standard deviation values for the discordant bed confluence simulation clearly indicate that the mixing process is much faster compared to the concordant bed confluence. However, the slope of mixing rates for two conditions are almost same after 10 times of channel width, so the effect of the discordance in mixing process is limited to the downstream zone near the confluence area.

5.2 Mixing process at natural confluences

The position of the mixing layer is clearly shown at the Bayonne-Berthier confluence with the high turbidity in the Bayonne River. Gaudet and Roy (1995) measured the electrical conductivity at the Bayonne Berthier confluence to monitor the mixing rate. They

measured several flow conditions on the 8 transects of Figure 5.8. The electrical conductivity values at transect 1 and 2 are applied as the inlet conditions for the current numerical simulations.

A natural confluence does not have a distinctive discordant characteristic as the laboratory confluence does with an abrupt drop of channel bed elevation. The bed changes more gradually. However, the effect of discordance can be studied using different flow conditions. As the water level drops, the depth ratio between the main channel and the tributary decreases and the role of bed discordance becomes more significant. In other words, the height difference between beds relative to mean flow depth becomes more important. Comparing the results from different flow conditions allows the effect of relative bed discordance to be verified. To compare the results for transect 5 to 8, extra simulations were required to study the relative importance of bed geometry of confluence on river mixing.

5.2.1 Mixing process closed to the junction

Two data sets from Gaudet and Roy (1995)'s measurements were selected to compare with the numerical simulations for high and low flow conditions. The numerical tracer was used in the numerical simulations to predict the pattern of mixing measured with electrical conductivity probes. For low flow condition, the values of the electrical conductivity for each tributary are 183.1 and 132.7 (μS/cm) for the Bayonne River and the Berthier River, respectively. For high flow condition, the values are 169.1 and 107.1 (μS/cm).

Figure 5.9 and 5.10 show the predicted mixing patterns from the numerical simulation for low and high flow conditions. Both figures have a vertical exaggeration factor of 7.0. Within the center of the confluence at cross section A from Figure 5.9 and 5.10, the mixing interface has a vertical alignment and is narrow. However, the results show a quite different mixing pattern for the two simulations. For the low flow condition simulation, as the flow enters the downstream channel, the bottom part of the mixing interface starts to expand inwards and upwards towards the Berthier side bank (Figure 5.9). The result from the numerical simulation for high flow condition shows a similar pattern of expansion in the mixing interface at the bottom of the channel, but the mixing interface remains almost vertical until flow reaches cross section C, and the mixing interface remains relatively narrow (Figure 5.10).

Figure 5.11 is the plot of the standard deviation values at several cross-sections. For high and low flow condition, it confirms the fact that mixing rate is faster for low flow condition, where the relative bed discordance is higher.

5.2.2 Mixing further downstream

Additional simulations were performed to study the relative importance of bed discordance of confluences on mixing in a river system. The geometry data of the river downstream of the Bayonne-Berthier confluence from Gaudet (1995) are used to construct the additional grids. The length of the channel from transects 4 to 8 is approximately 580 m. The whole

channel length is divided into 10 segments to reduce the size of the grid for the numerical simulation. Figure 5.12 shows the combined 10 grids altogether to reproduce the map of Figure 5.8. Each grid has a dimension of 80 x 56 x 12 cells.

The contour plots for the predicted electrical conductivity are shown in Figure 5.13 and 5.14 for low and high flow conditions. Both cases show similar mixing patterns downstream of the confluence, and the similarity increases as the flow reaches the downstream cross-sections. The contour plot shows that the mixing process of high flow condition is slow downstream of the main confluence until the flow reaches transect 6. However, mixing is nearly completed at transect 6 for low flow condition. The mixing interface widens not only at the bottom of the channel but also at the water surface. The mixing rate increases markedly as the flow passes through the bend between transects 6 and 7. Mixing is almost completed after transect 7.

Figure 5.15 shows the standard deviation calculated from the simulations results. It shows that the mixing rate is large close to the junction, particularly at low flow, then it decreases downstream from the confluence, and increases again in the bend at non-dimensional distances close to 30 downstream of the bend. The standard deviation values for high flow condition are slightly higher compared to the low flow condition in the confluence area, and this might be due to the lower relative depth difference.

Gaudet and Roy (1995) used the deviation concept to calculate complete mixing. The deviation is defined as:

$$D = \frac{(C_o - C_E)}{C_E} x100 \qquad (5.1)$$

where C_o is the observed value of the concentration and C_E is the expected value of concentration. The predicted value is calculated by the formula of Bencala et al. (1987).

$$C_E = \frac{(C_1 Q_1 + C_2 Q_2)}{Q_3} \qquad (5.2)$$

where C_1 and C_2 are the concentrations of the main and secondary tributaries, Q_1 and Q_2 are the flow rates of the main and the secondary tributaries, and Q_3 is the total flow rate of the confluence, which is the sum of Q_1 and Q_2.

Following Gaudet and Roy (1995), the maximum and the minimum values of the electrical conductivity of each transect are chosen and the deviation values were calculated for those maximum and minimum values. The comparison between predictions from the simulations and the field measurements is shown in Figure 5.16 and 5.17 for low and high flow condition. For high flow conditions the data available are limited to only transects 3, 4, 6, and 8 with a limited number of sampling points. Hence, the comparison is not clear. However, Figure 5.16 shows that the predicted pattern of the deviation change is similar to the observed one. Gaudet and Roy (1995) defined the complete mixing as deviation values below 10 %. According to that definition, the field data and the numerical simulation for low flow condition show that the complete mixing is reached at a distance of 25 times the channel width. This distance corresponds to a position upstream from the bend. Figure 5.17 shows the complete mixing is reached about 30 times the channel width, which is slightly longer than the result from the low flow condition.

The prediction from the simulations of the laboratory confluence and the natural confluence shows that the discordance of the confluence plays an important role in enhancing the mixing process in the river system. However, the role is local. The comparison with field measurements also indicates that the model can accurately predict mixing rates at a natural complex river confluence.

6. BRIEF DISCUSSION OF RESULTS

Confluences are very common features in natural rivers and hydraulic structures. They function as nodes where the mixing processes are intense. Therefore, the understanding of confluence flow is essential to use and control open channels in river engineering. However, there have been only a limited number of studies on these sites due to the complexity of the flow and the difficulty in obtaining reliable data with the available measuring devices and methods. Consequently, the recent trend of using numerical models for confluence studies is very promising.

The main objective of this study was to investigate the mixing characteristics in river systems, especially in the vicinity of river confluences, using a three-dimensional numerical model. This chapter summarizes the procedures adopted for the study of confluence flows and discusses some of the results obtained on mixing rates with regards to other mixing studies.

6.1 Numerical modeling

A three-dimensional numerical model has been applied to laboratory confluences for purposes of validation. After the successful validation, the three-dimensional numerical model was applied to a natural confluence. The application of the model to both the laboratory and natural confluences showed the advantages of the numerical modeling.

The level of detail of the data obtained from the model was only limited by the number of cells in a grid pattern and by the computer memory. The ease of visualization providing streamline presentation, vector plots and contour plots aided the interpretation of the results from the model prediction greatly. However, the boundary conditions had to be described accurately and a proper modeling procedure had to be chosen. There were several aspects of the modeling effort that had to be considered carefully for the present study due to the use of assumptions in the model to simplify the problem such as turbulence closure, grid generation, and boundary conditions.

6.1.1 Turbulence closure model

The model of the present study used the RNG k-ε turbulence model that is known to be more accurate than standard k-ε model. In particular, flows in curved geometries, stagnation flows, separated flows, and swirling flows are situations which the RNG k-ε turbulence model has been reported to be more accurate than the standard k-ε model (e.g., Benim, 1990; Widmann et al, 1999). However, the results from the present study showed that RNG k-ε turbulence model usually underestimated the magnitude of the turbulent kinetic energy in the mixing layer. This could be due to the fact that k-ε models are based on the use the isotropic eddy viscosity concept. However, non-isotropic characteristics might play important role because of significant streamline curvature and secondary circulation. Other more complex turbulence models, such as Reynolds Stress Transport

Model (RSTM) and Large Eddy Simulation (LES) might improve the accuracy of the prediction. It is known that Reynolds Stress Transport Model (RSTM) has the advantage that terms accounting for anisotropic effects are introduced automatically into the stress transport equations. However, both RSTM and LES may be still too expensive in terms of storage and execution time for practical engineering applications of three-dimensional flows (Rodi, 1984; Speziale, 1991).

6.1.2 Grid generation

Cell skewness

The first step in the modeling procedure was to generate proper grids. As described in section 2.3, the principles of grid generation are straightforward. However, satisfying all the required conditions at the same time was difficult. The present study used the finite volume method with body-fitted coordinates, so the physical domain was divided into cubic cells. The grid for the laboratory confluences in chapter 3 with rectangular cross-sections was constructed without major problems except for the cells around the junction apex where the junction angle was 30° (Figure 3.3). On the other hand, the grid generation for the natural confluence with a complex geometry required numerous trials to meet the conditions stated earlier. In particular, the skewness of the cells at the junction apex and at the riverbanks, and the cell aspect ratio at the riverbanks had to be optimized to satisfy the conditions explained in section 2.3 as much as possible.

Geometry of the confluence

In addition to the difficulty in generating grids due to the irregular shape and the junction angle of the natural confluence, obtaining large amounts of data to describe the details of confluence geometry was one of the key factors to be considered in grid generation. Also, the input of large amount of geometric data into the model to generate a grid had to be done without any error. Slight changes in the grid geometry from faulty input of data can cause significant variations of the model predictions, especially in the region where the velocity field is complex.

Interpolation of the data

The geometry of the field channel is composed of coordinates of discrete points. The interpolation of the coordinates between field data points was necessary, since the cell size is much smaller than the spacing between the measuring points in the field. The grids of Bradbrook (1999)'s study was generated using smooth curves with linear interpolation only in the lateral direction of the channel. Hence, the presentation of the channel geometry was unrealistic in the downstream direction. The grid lines in the downstream direction between the cross-sections were straight lines (Bradbrook, 1999), creating sharp edges between the straight lines. The grids for the present study were constructed with smooth curves using linear interpolation in both downstream and lateral directions, so that the adverse effects of skewness of the cells was greatly reduced in the junction area.

A combination of reliable geometric data, realistic presentation of the physical model in the grid generation, and careful grid control was crucial in generating grids for the present study.

6.1.3 Boundary conditions

As stated earlier, a proper description of the boundary conditions was also an important factor to be considered. The boundary conditions for the laboratory confluences used in the present study were relatively simple and easy to implement. However, the boundary conditions for the natural confluence were much more complex. The effect of the curvature of channels upstream of the junction on the velocity field had to be taken into account. The results from the simulations of the flow in the curved channel upstream of the apex provided the velocity field at the outlet of the curved channel. These were used as the inlet conditions for the main confluence model. The comparison between the simulations with and without flow in the upstream curved section **abcd** and **efgh** (Figure 4.7) showed that the accuracy of the prediction of the model was substantially increased, when the flow in the upstream curved section was considered.

Another effort to improve the prediction of the model was the adoption of the free surface approximation described in chapter 2. Inclusion of the free surface effects in the computation provided correlation coefficients between velocities (model data and field results) much higher than for the case where the model had a rigid surface. One can use measured free surface profiles during test as inputs to the simulation model. This is also found to improve the correlation between measured and computed velocities as mentioned in section 3.1.3. However, this method requires a great deal of effort to collect detailed water surface profile data from the laboratory and the field. Fairly accurate measurements

can be obtained in the laboratory, but this is much more complicated in the field where flow conditions may vary, giving rise to temporal variations of the water surface (Biron et al., 2002).

6.2 Mixing process

There are a number of numerical models that can predict the mixing rate in natural confluences. These include CORMIX and ELHADI. However, most of them are one- or two-dimensional models. CORMIX model uses two-dimensional calculations, and it can predict mixing processes up to 400meters downstream of the pollutant discharge location. It provides three different types of pollutant discharge; single port, multiport, and surface. The natural confluence can be modeled as a single port type with variable settings of the junction angle, the mean velocities of the main and tributary channel, and the concentration of pollutant in the tributary. However, the prescription of complex three-dimensional bed geometry at the confluence is limited to the junction angle and the Manning's roughness coefficient. Lane et al. (1995) applied a two-dimensional depth-averaged model, which had a capability to present secondary circulation, to a braided river system that included a number of confluences. Their model showed limitation in representing the secondary flows in confluence zones properly. Gaudet (1995) used CORMIX and ELHADI model to compare the mixing rate at the Bayonne-Berthier confluence with the field measurements. The comparison showed that both models underestimated the mixing rate in the confluence zone for a low flow condition significantly. This was attributed to the fact that bed discordance (which is more important at low flow) was not taken into account by the model.

The reliability of a two-dimensional model is limited by the assumptions to represent the three-dimensionality of a flow.

The three-dimensional numerical model might not have so many advantages over the one- or two-dimensional models for the prediction of the flow field and mixing processes for relatively straight and simple river sections. However, the complex flow dynamics and mixing processes at a confluence are closely related to the bed geometry. Hence, the use of a three-dimensional numerical model is essential.

The present study applied a three-dimensional numerical model with a numerical tracer of different concentrations in the main and tributary channels. The mixing process was monitored using contour plots of the downstream cross-section and standard deviations from the expected concentration values. When water levels are high and bed discordance is less important, flows from each merging channel of a confluence remain segregated along their respective sides. For low flow condition, the effect of discordance is relatively important. The water from the shallow tributary tends to flow above the water from the deeper main channel. This intensifies the helical cell development as shown from the simulation results, and this process is responsible for the enhanced mixing process at confluences The distance to reach a complete mixing was about 25 times the channel width for the simulation of low flow condition where the effect of discordance is significant, and this agrees well with Gaudet (1995)'s field measurements. The present study showed that the three-dimensional numerical model is able to produce accurate predictions of the complex flow field and mixing process at confluences.

The use of a three-dimensional numerical model requires a significant increase in computing cost and in the complexity of the model. However, the current rapid development of computing technology is also making these problems less significant. Also, the development of technology in measuring field data with greater accuracy and efficiency will provide better data to prescribe the boundary conditions for three-dimensional numerical models.

7. CONCLUSION AND SCOPE OF FUTURE RESEARCH

7.1 Conclusion

1. The quantitative and qualitative analysis of the present study showed that the proposed model is capable of capturing the important features of the confluence flow such as the zone of separation, the zone of stagnation, and the development of helical cells (secondary flows) accurately. The predictions of the numerical model for the natural confluence showed good agreement with field measurements of the natural river confluence.

2. Judicial adjustments of the gridlines to ensure orthogonality of the grid structure improve the result of the simulation markedly. The improvement in the simulated results is traced to the reduction in the adverse effects of the skewness of the cell configuration.

3. It is extremely important to incorporate the flow structure upstream of the confluence to get meaningful mixing flow characteristics of confluences. The boundary conditions upstream for the tributaries control the mixing characteristics. As such, one should obtain these upstream boundary conditions by starting the simulation at a section which is farther upstream of the confluence that includes features such as bends and meanders.

4. Simulations which incorporates free surface effect lead to improved predictions of the flow field.

5. Bed discordance clearly enhances mixing in the vicinity of the junction. The three-dimensional model can incorporate this effect related to bed geometry and the comparison between the simulated mixing rates and those measured at a natural confluence is good. Distances to reach complete mixing are about 25 times the channel width.

7.2 Future research

Although the three-dimensional numerical model was able to capture most of the important features of confluence flow dynamics with reasonable accuracy, the details it can provide were limited by the number of cells in the grid. The resolution of the grid could be increased substantially to study the complex flow pattern in the mixing layer more closely.

The present study used steady-state simulations. However, the periodicity of flow in the mixing layer can be studied using unsteady simulations. Also, more complex and advanced turbulence models such as RSTM and LES can be applied as the computer expense are further reduced. A combination of a better turbulence model and unsteady-state simulations will help to understand the periodic nature of the mixing layer of confluences, which is critical in terms of mixing.

The numerical tracer used in the present study was assumed to be conservative and non-reactive, and this was sufficient to represent the behavior of simple contaminants and ionic species in a natural river system. However, the behavior of contaminants which can be found in a natural system, is more complex in most cases. The model used in the present

study could be modified to predict the fate of such contaminants.

The relationship between the bed form development and the sediment transport in a confluence is also an important characteristic of confluence to be understood. Coupling the model with a sediment transport model would provide a better insight in the nature of confluence dynamics and would allow the changes in bed geometry occurring during a flood event and their effect on mixing to be taken into account.

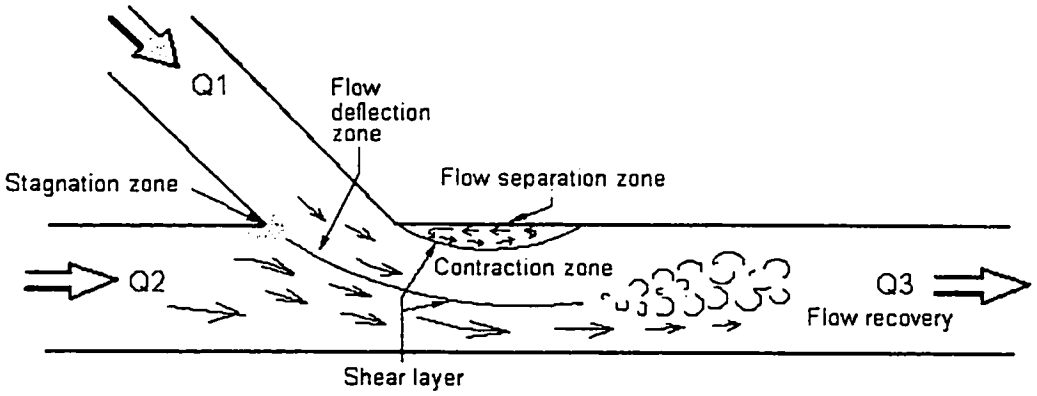

Figure 1.1 Flow features of confluences (modified from Best (1987))

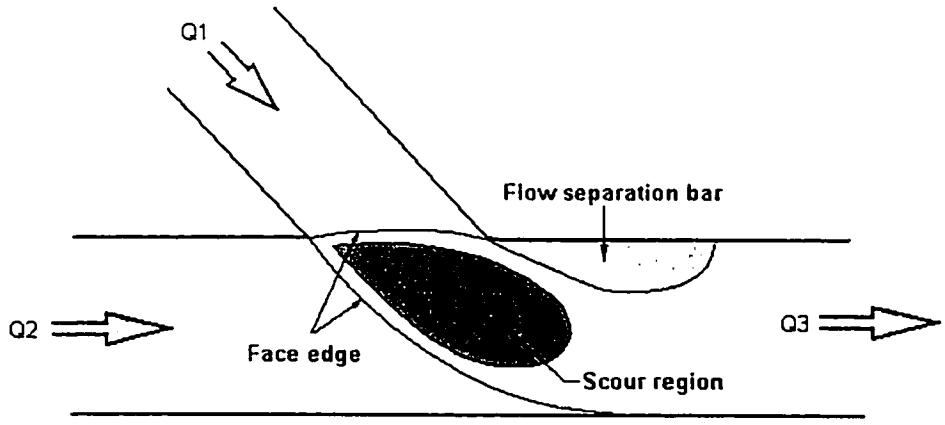

Figure 1.2 Simplified bed topography of an asymmetrical confluence

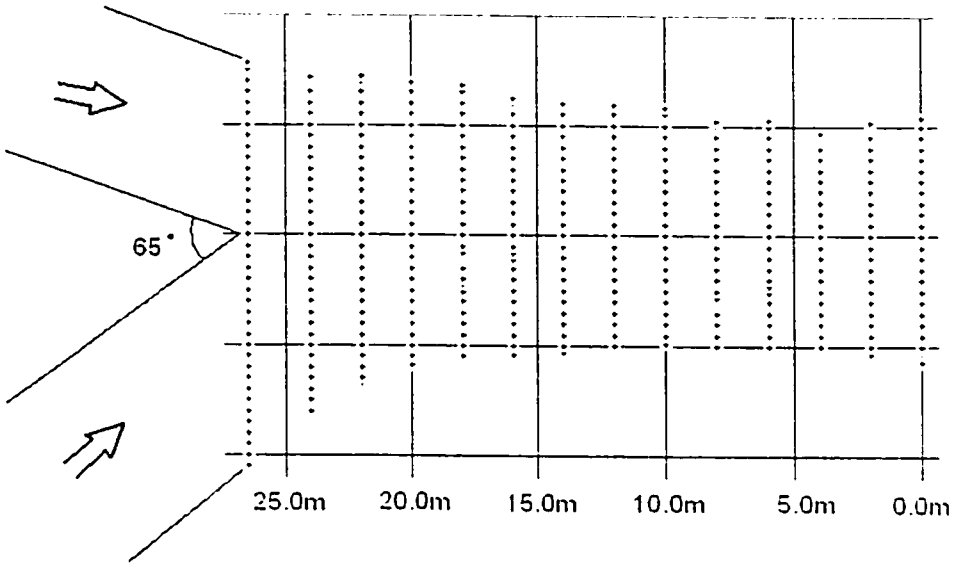

Figure 2.1 Location of the geometric sampling points for the Bayonne-Berthier confluence

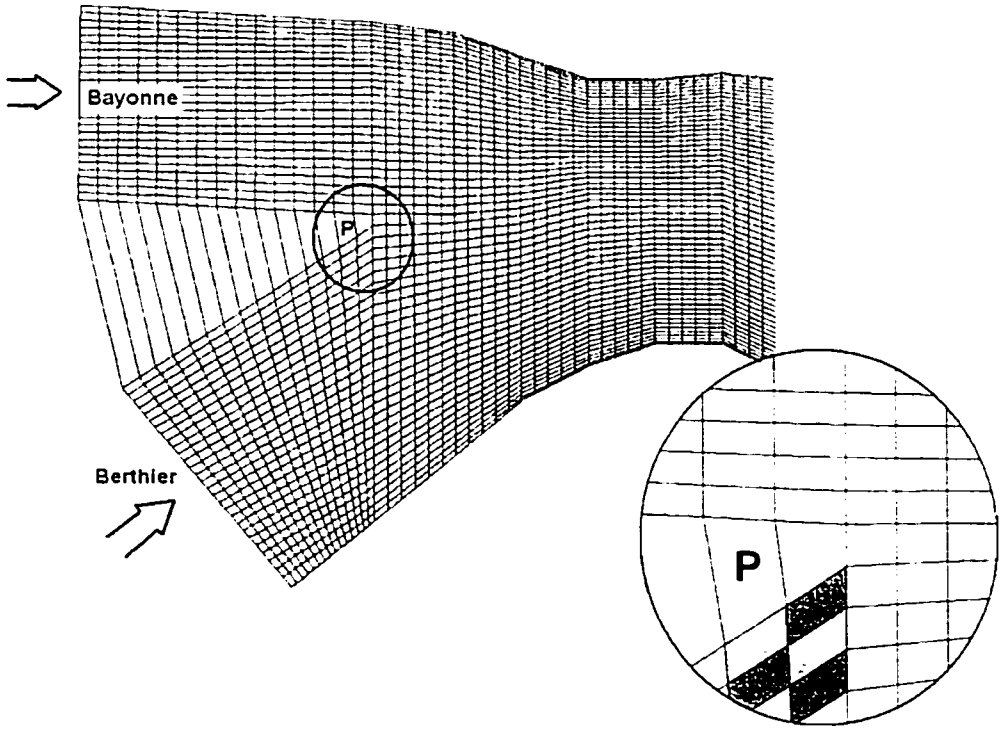

Figure 2.2 Cells at the junction apex

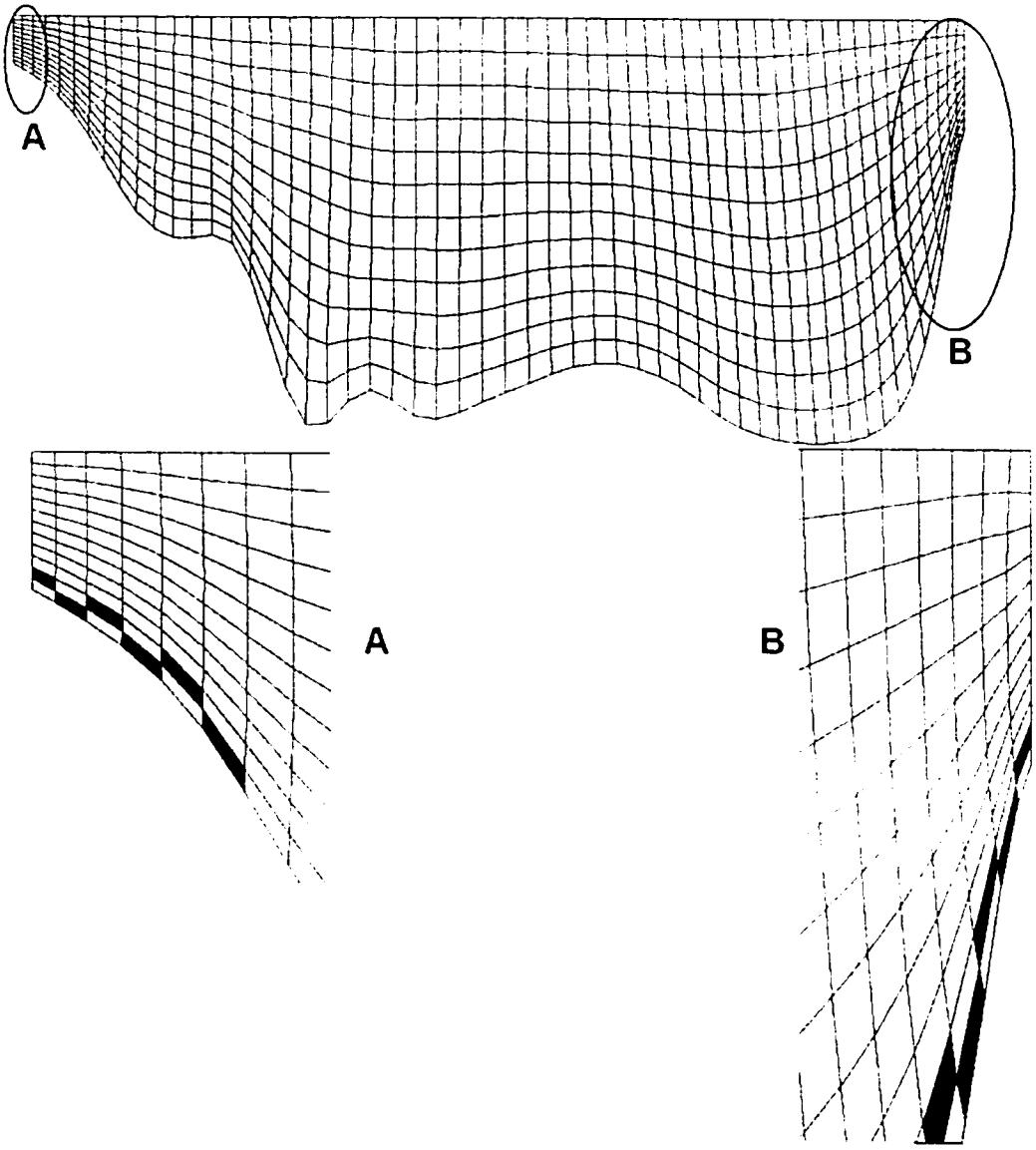

Figure 2.3 Cross-section at 20.0m (vertical exaggeration factor of 5.0)

a) Prior to gridline control

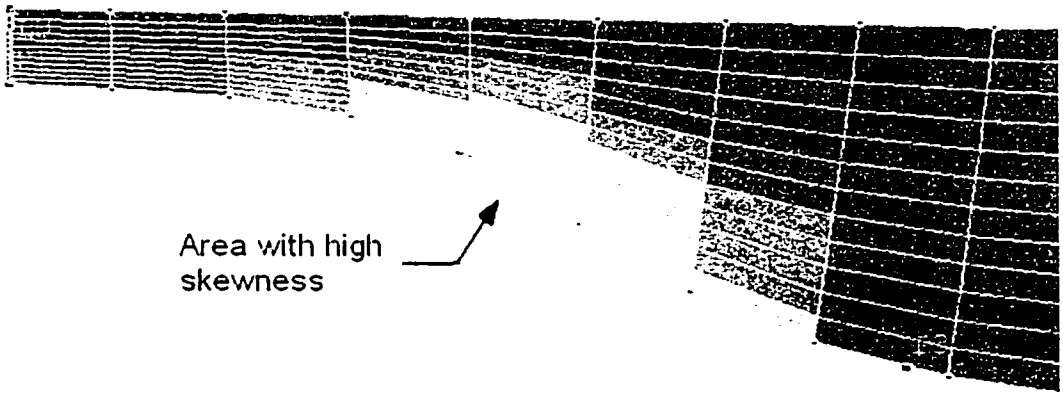

b) After the gridline control

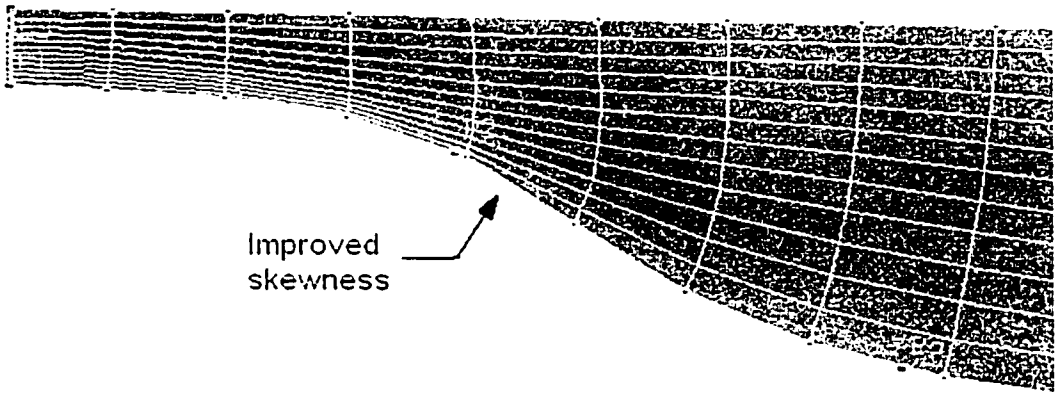

Figure 2.4 Grid control

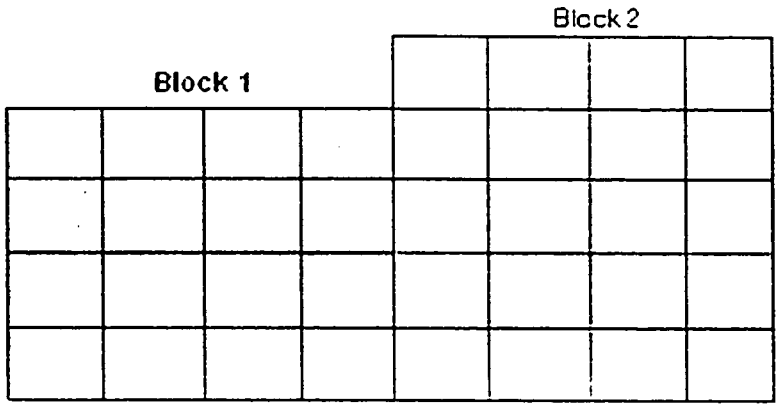

Figure 2.5 Concept of multi-block method

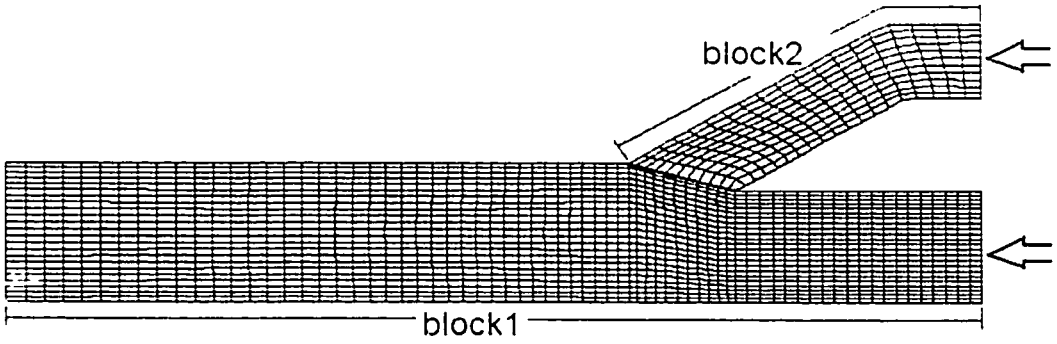

Figure 2.6 Multi-block grid for concordant bed simulation

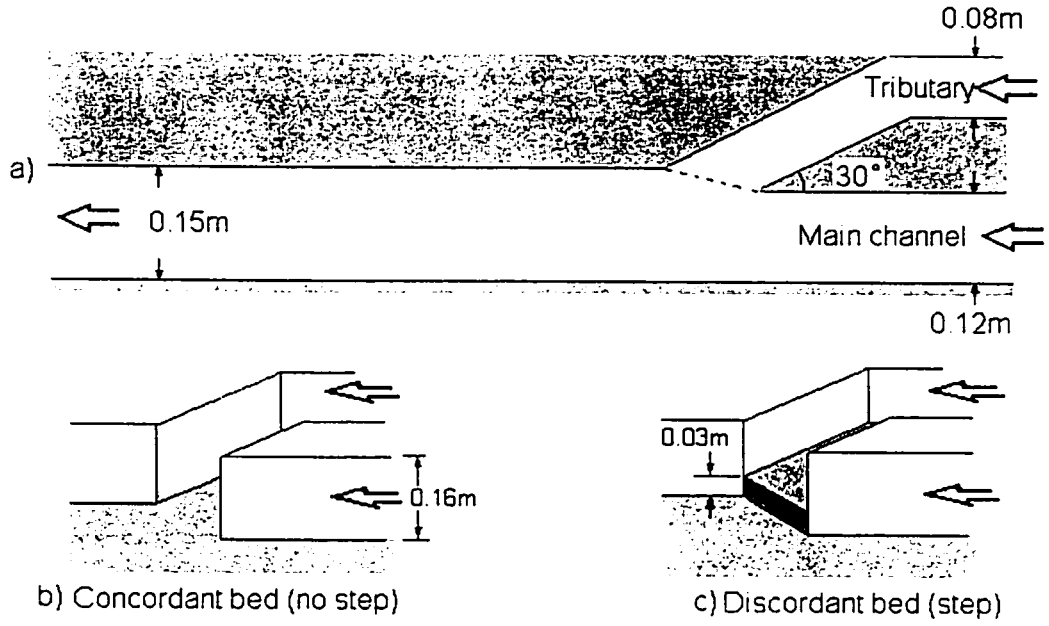

Figure 3.1 Laboratory experiments of Biron et al., (1996a,b): a) plan view; b) concordant bed configuration; c) discordant bed configuration. (Modified from Biron et al., (1996a,b))

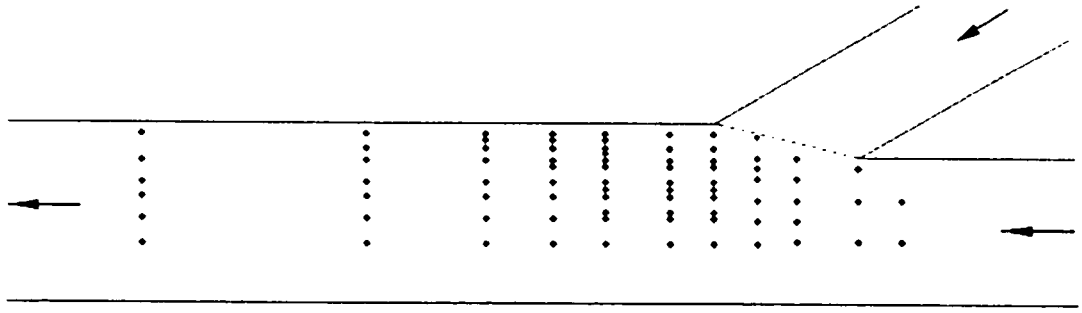

Figure 3.2 Position of the measuring points in Biron et al.'s (1996a, b) experiments. Five different heights above the bed were sampled.

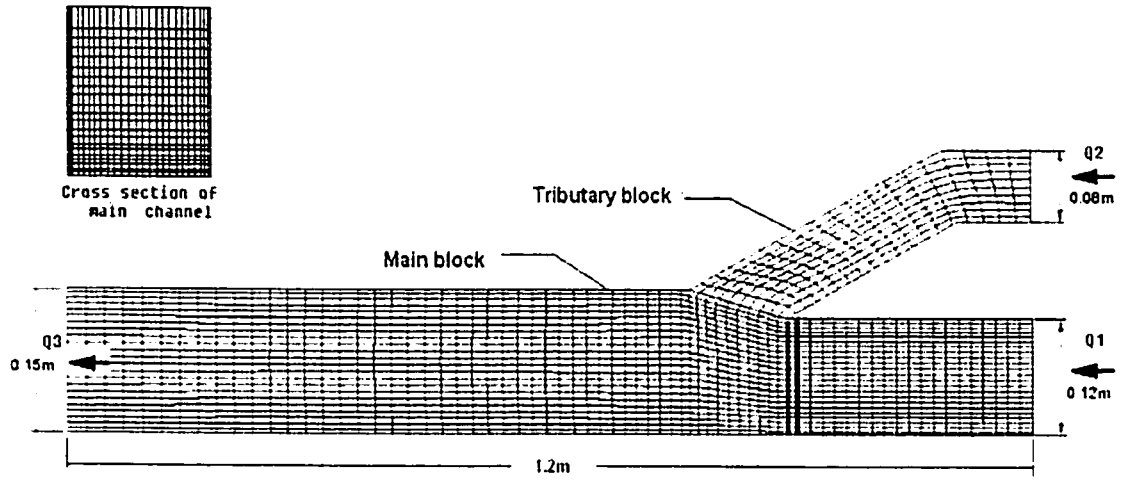

Figure 3.3 Grid for both the concordant bed and discordant bed model

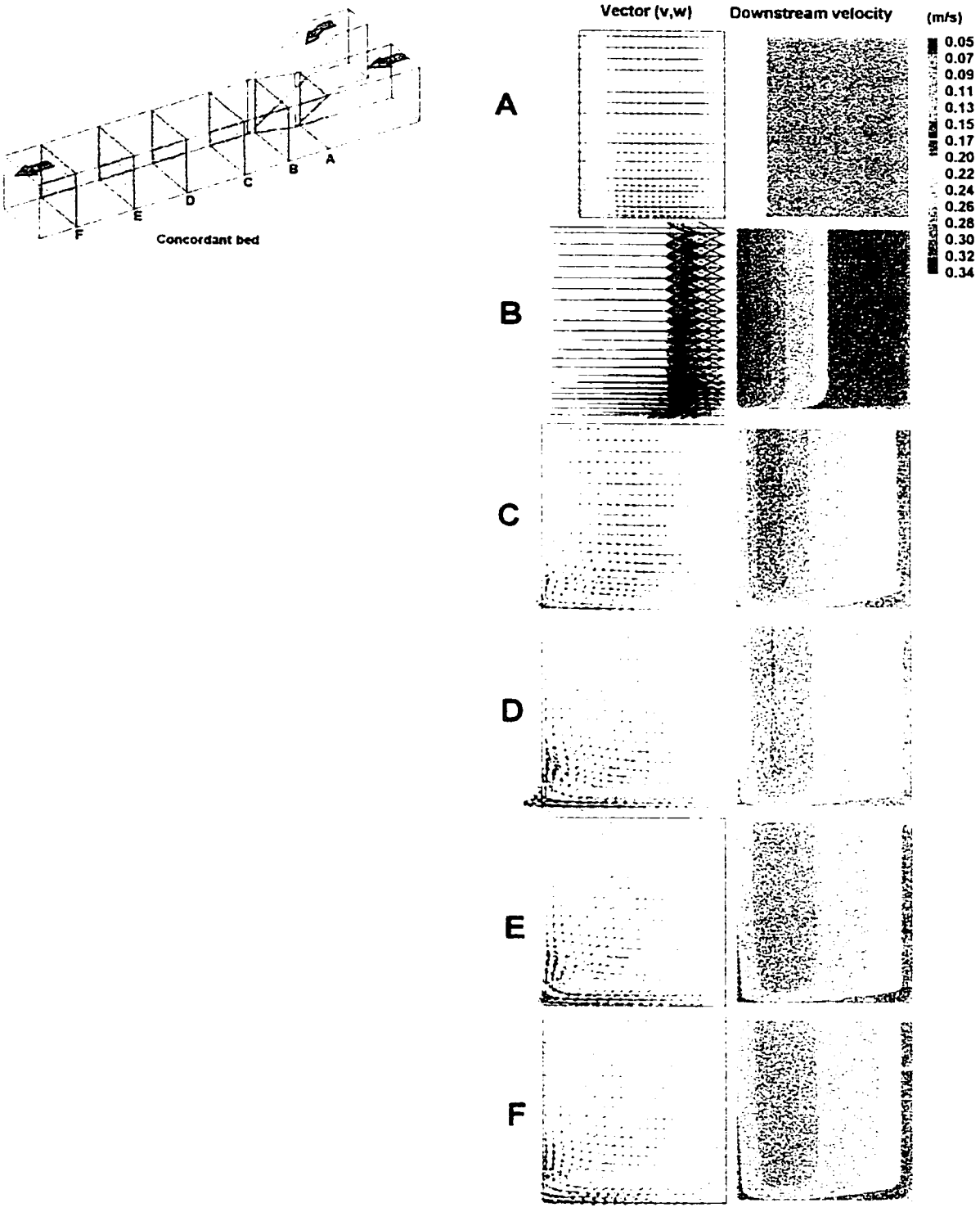

Figure 3.4 Vector plot of the lateral and vertical velocity components and the contour of downstream velocity for the concordant bed simulation

(a)

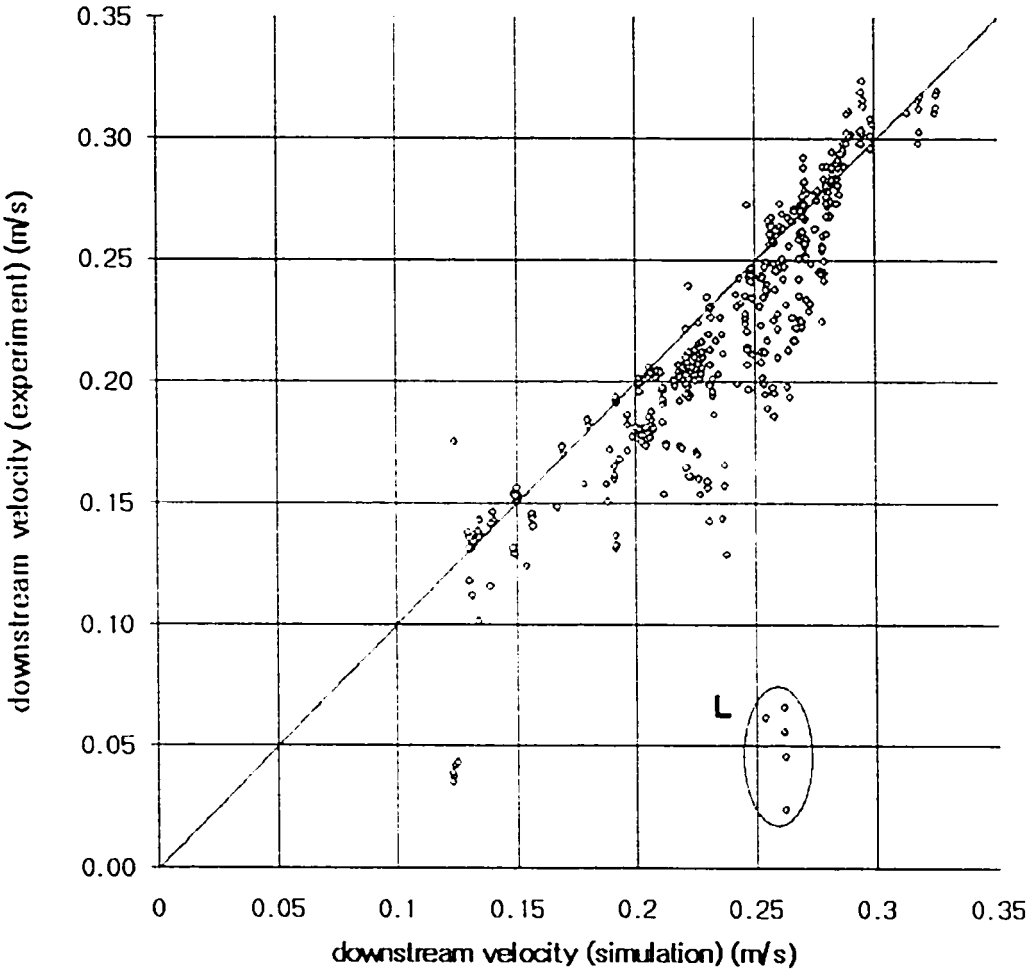
0.35
0.30
0.25
0.20
0.15
0.10
0.05
0.00
0
0.05
0.1
0.15
0.2
0.25
0.3
0.35
downstream velocity (experiment) (m/s)
downstream velocity (simulation) (m/s)
L

(Continued)

(b)

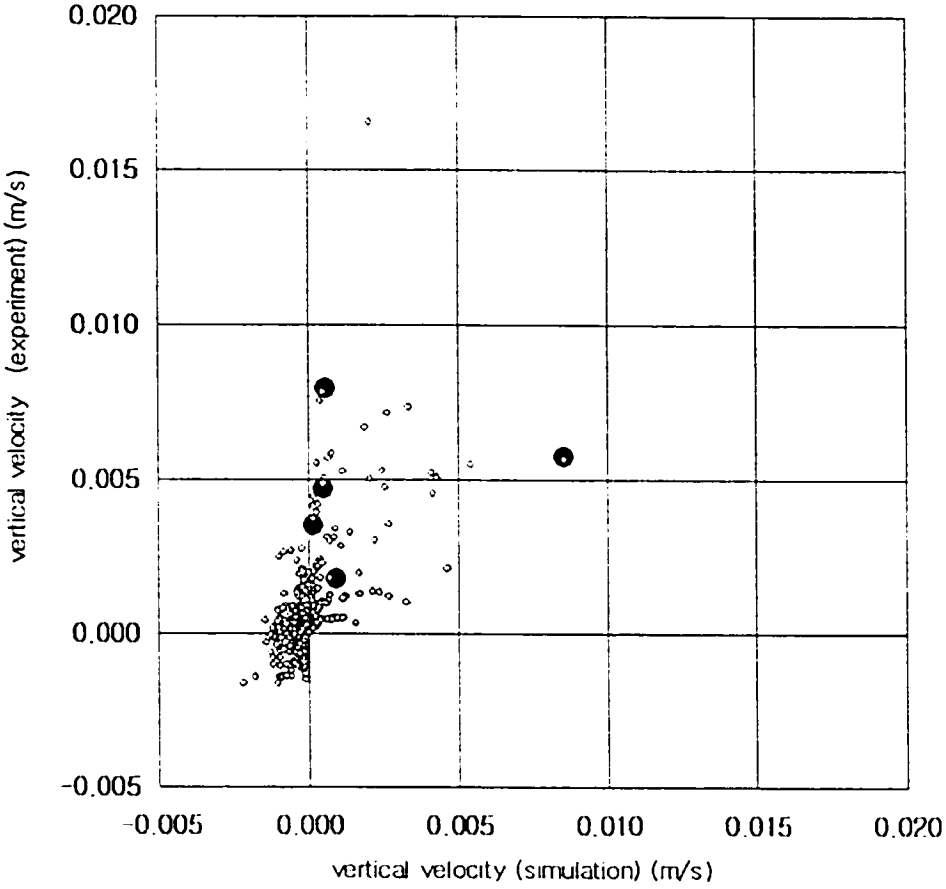

Figure 3.5 Comparison of laboratory measurement (y-axis) and model prediction (x-axis) for concordant bed experiment of Biron et al. (1996 a,b); (a) downstream velocities; (b) vertical velocities

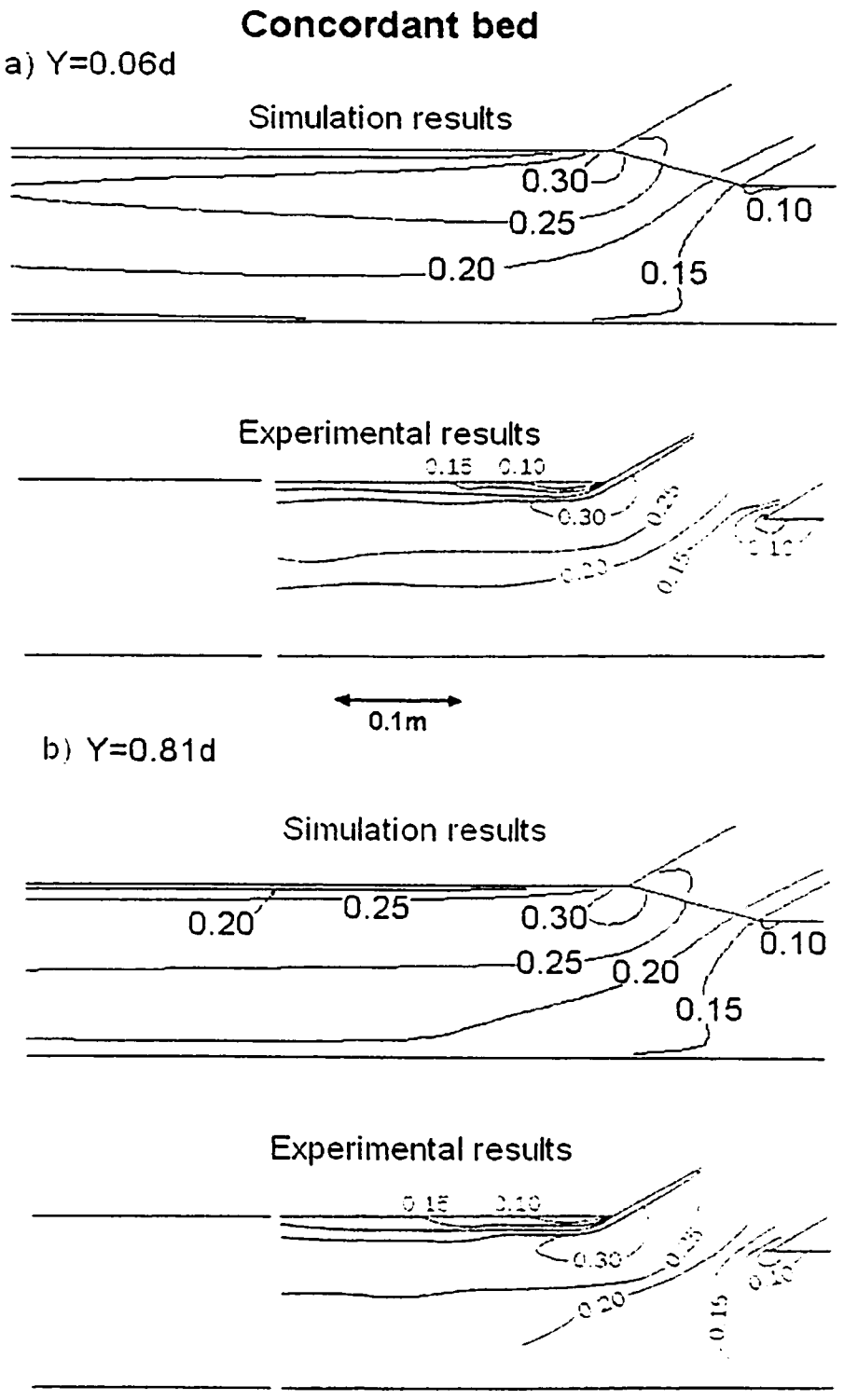

Figure 3.6 Comparison between simulation results and experimental results of Biron et al. (1996a,b) for concordant bed experiment-contours of downstream velocity;(a) 0.06d above bed; (b) 0.81d above bed. Where d=Maximum depth (Experimental results are taken from Biron et al. (1996a))

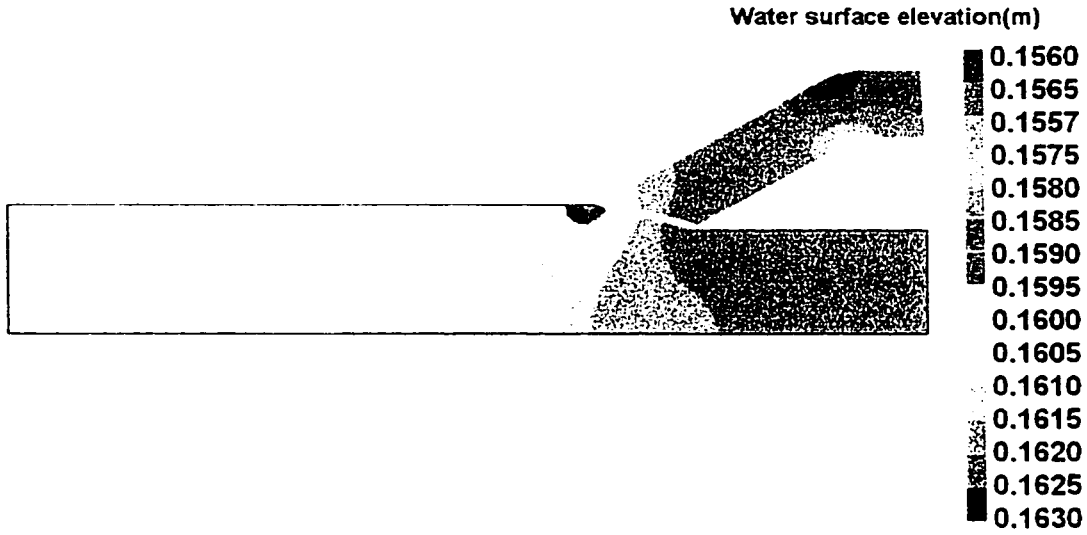

Figure 3.7 Predicted water surface elevation of concordant bed confluence

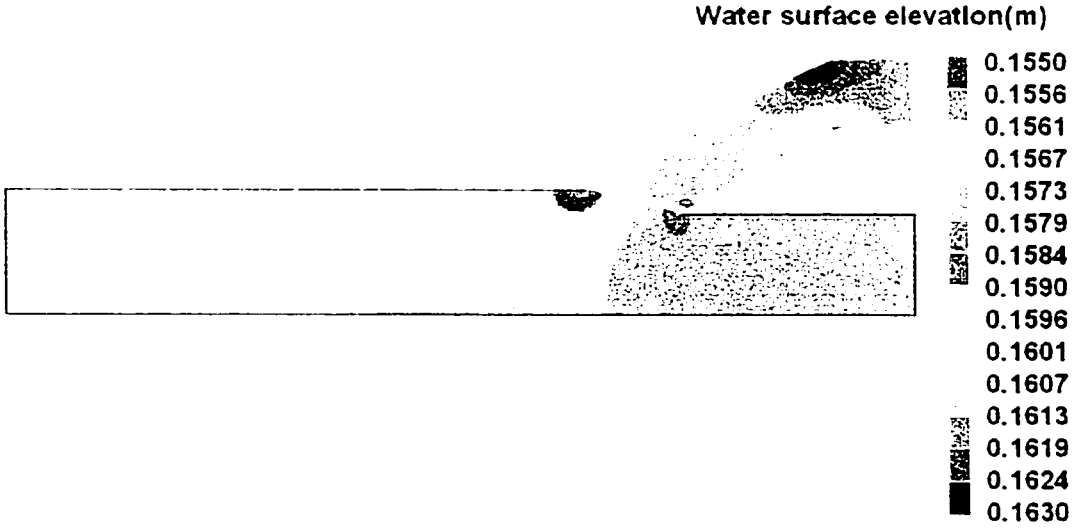

Figure 3.8 Predicted water surface elevation of discordant bed confluence

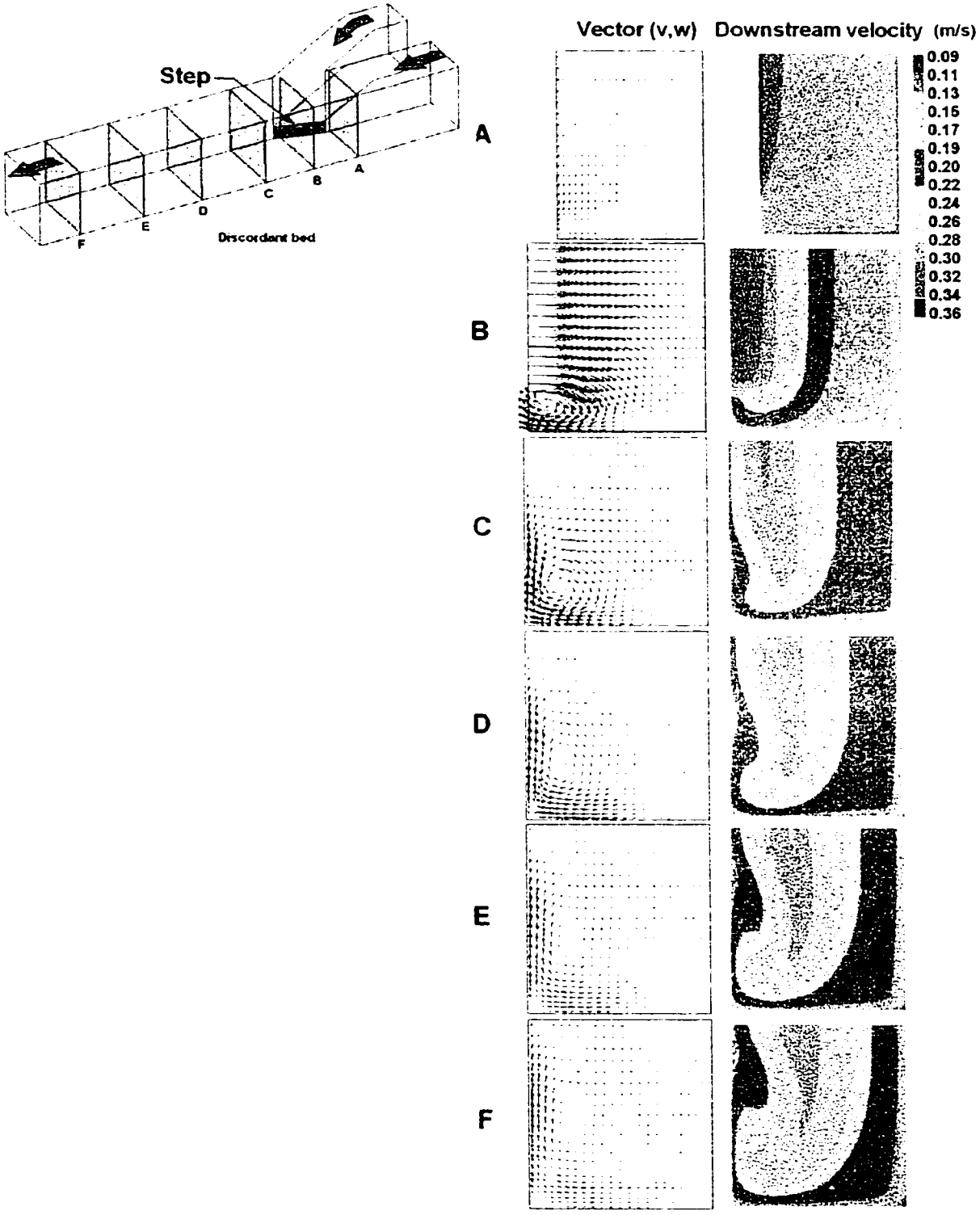

Figure 3.9 Vector plot of the lateral and vertical velocity components and the contour of downstream velocity for discordant bed simulation

(a)

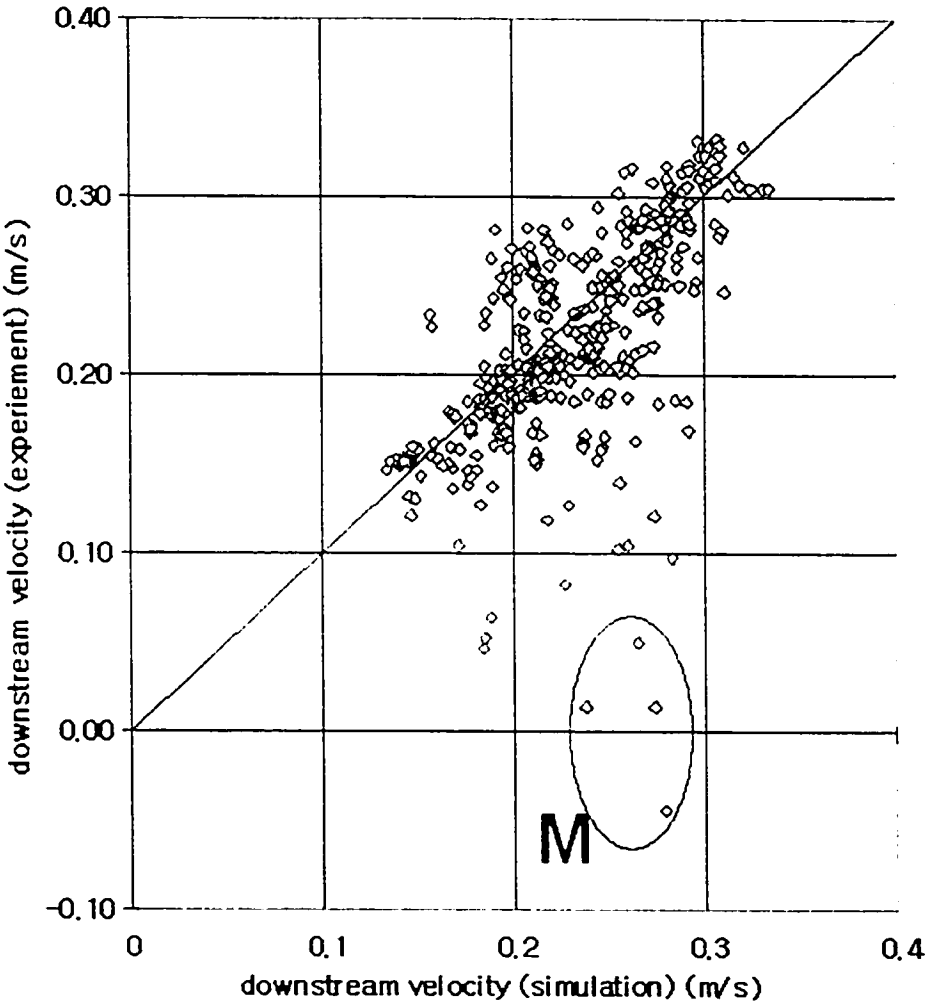
0.40
0.30
0.20
0.10
0.00
-0.10
0
0.1
0.2
0.3
0.4
downstream velocity (experiement) (m/s)
downstream velocity (simulation) (m/s)
M

(b)

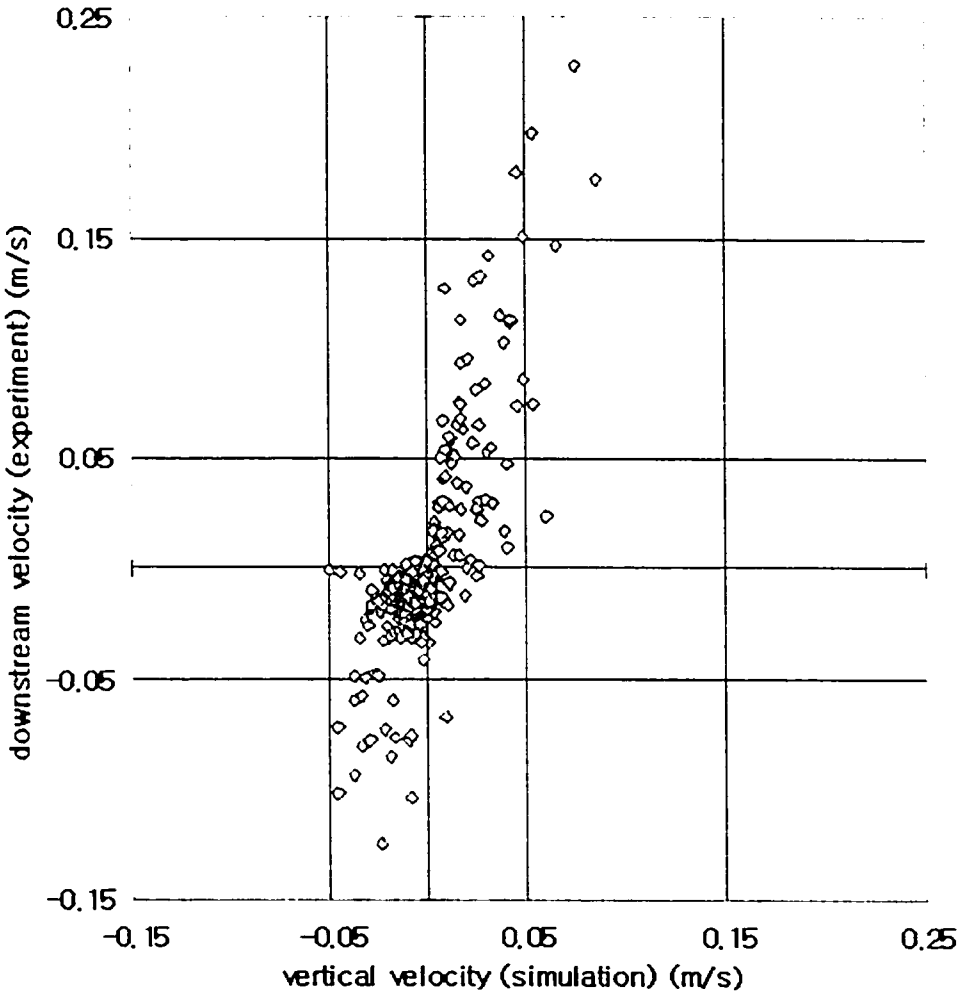

Figure 3.10 Comparison of laboratory measurements (y-axis) and model prediction (x-axis) for discordant bed experiment of Biron et al. (1996 a, b); (a) downstream velocities; (b) vertical velocities

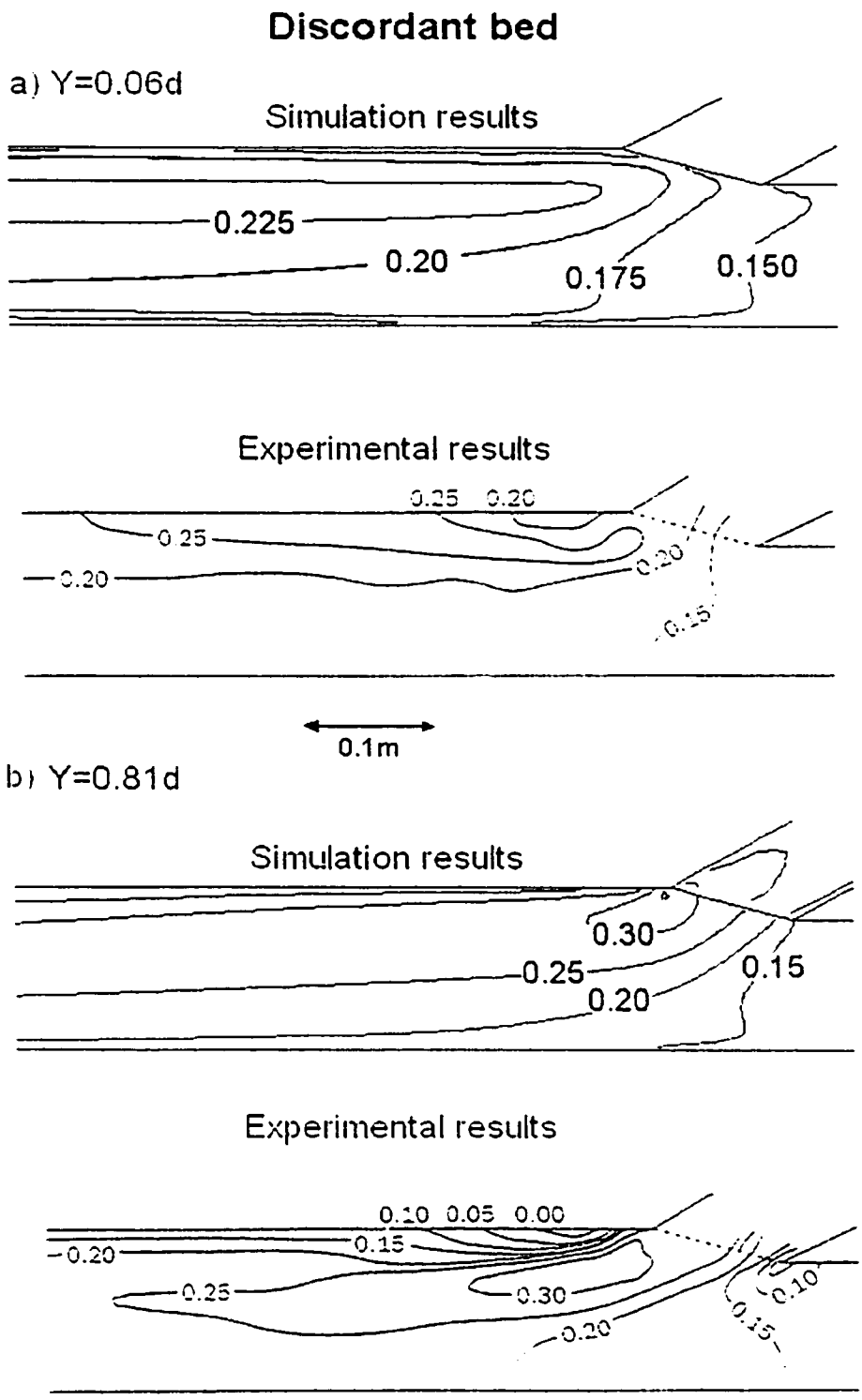

Figure 3.11 Comparison between simulation results and experimental results of Biron et al. (1996a,b) for concordant bed experiment-contours of downstream velocity;(a) 0.06d above bed: (b) 0.81d above bed. Where d=Maximum depth (Experimental results are taken from Biron et al. (1996a))

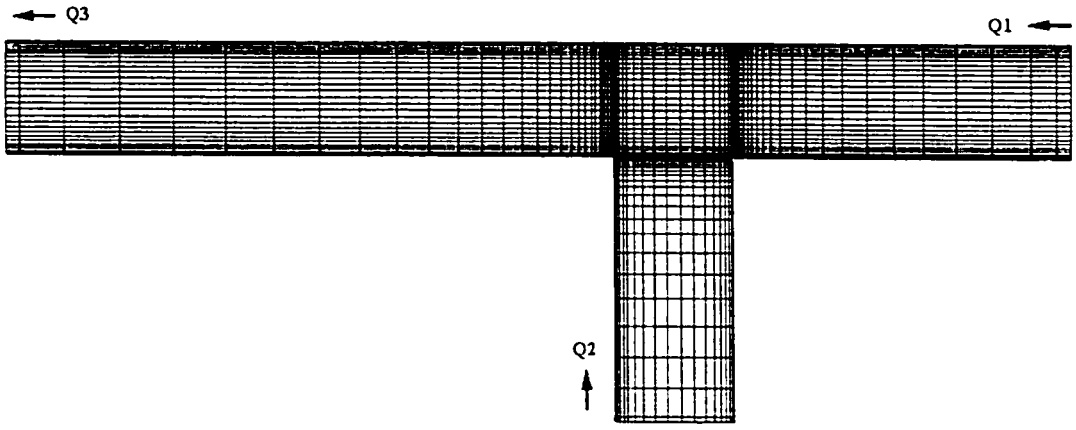

Figure 3.12 Plan of grid for Weber et al (2001)'s 90° open channel junction

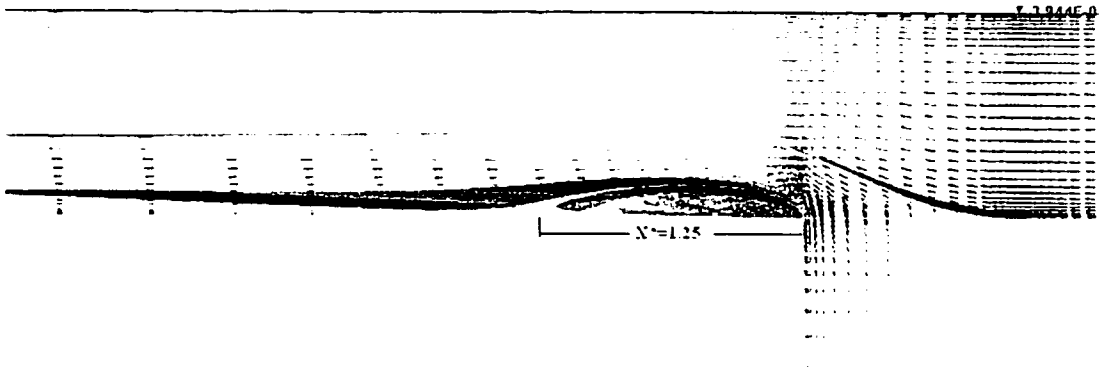

a) Near surface (Z*=0.014)

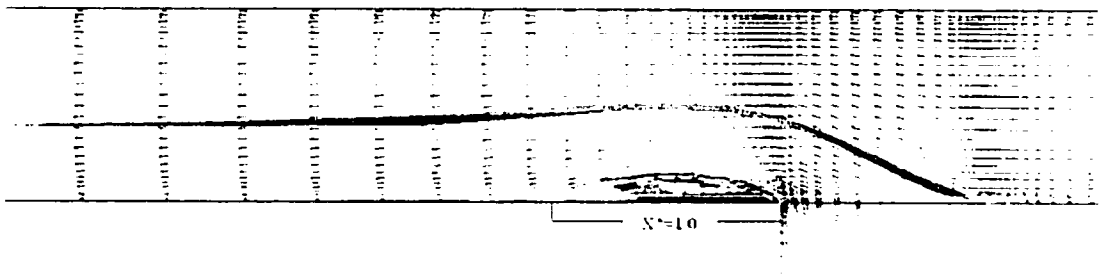

b) Near bed (Z*=0.278)

Figure 3.13 Velocity vectors and streamlines from the simulation of Weber et al.(2001)'s experiment (Where X*, and Z are the non-dimensionalized coordinates for x/W, z/W, respectively. W is the channel width.)

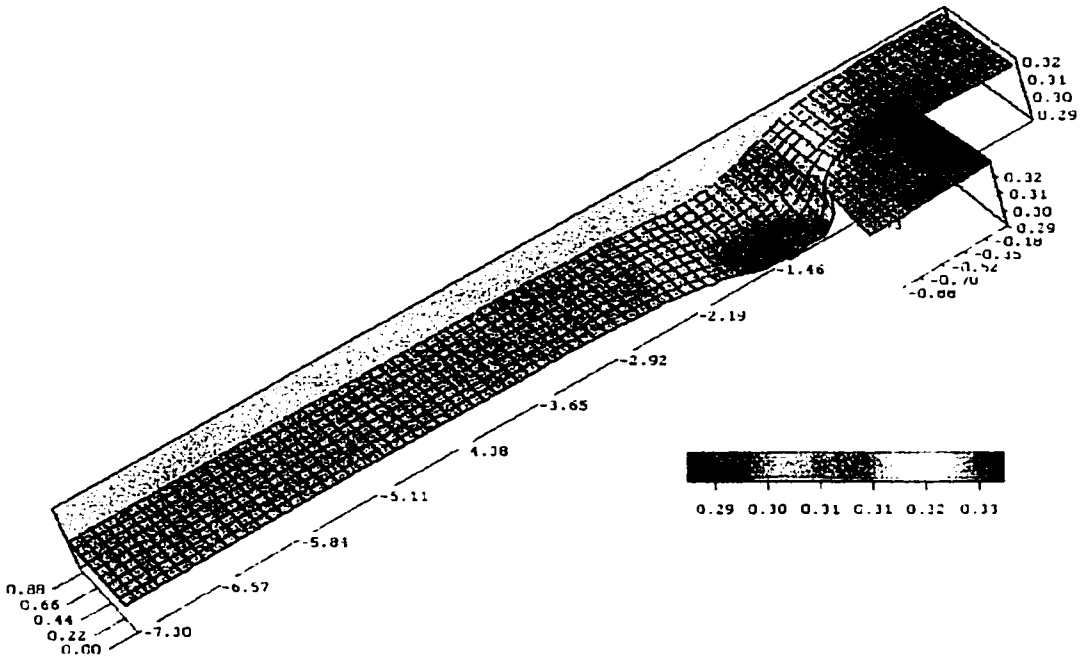

a) Free surface geometry from experiment (Weber et al., 2001)

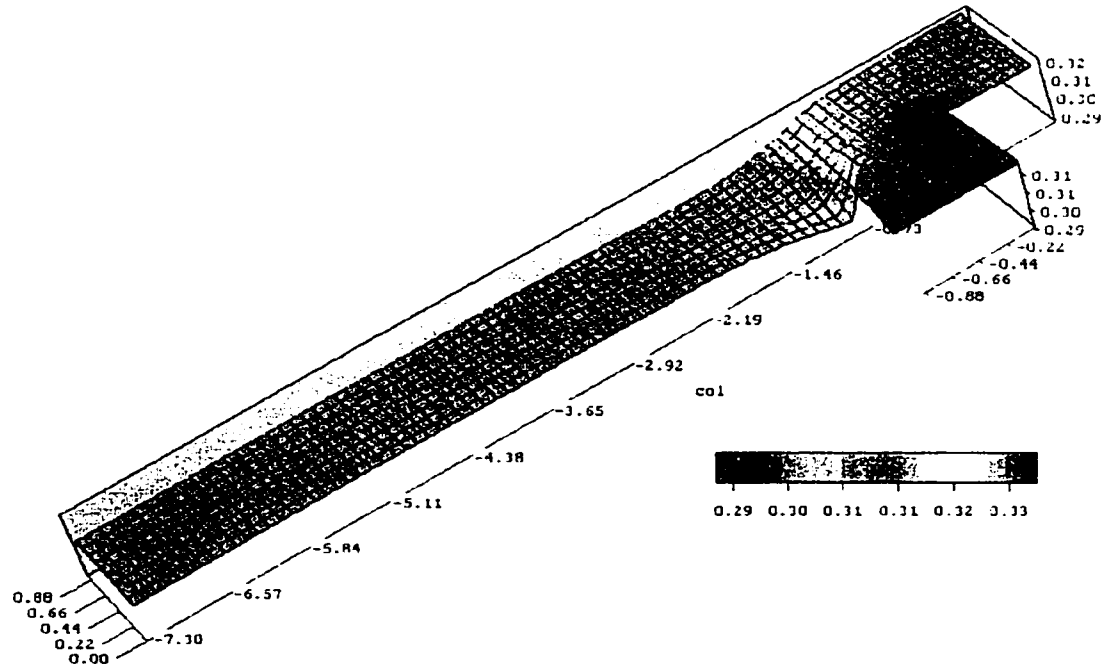

b) Free surface geometry from simulation

Figure 3.14 Comparison of water surface profile between (a) measurement from the laboratory and (b) model prediction

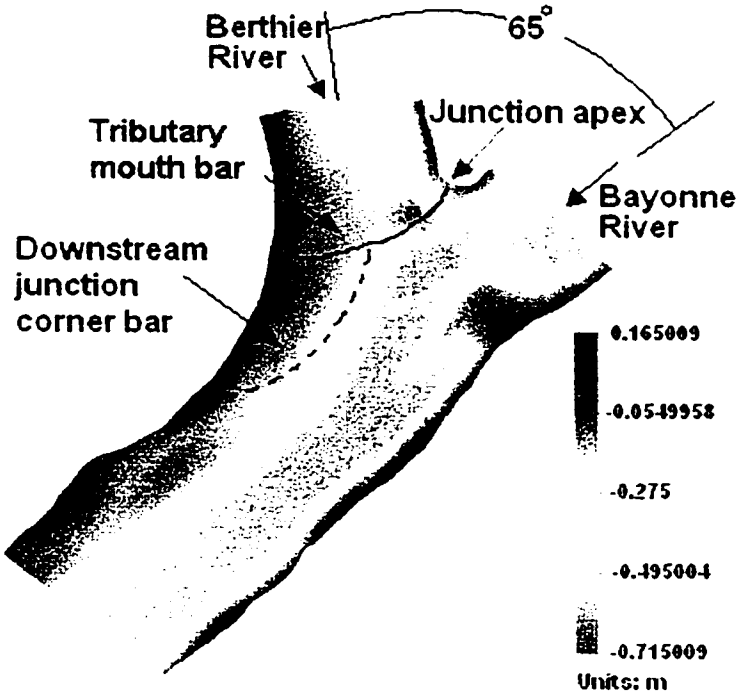

Figure 4.1 Morphological features of the Bayonne-Berthier confluence (arbitrary datum)

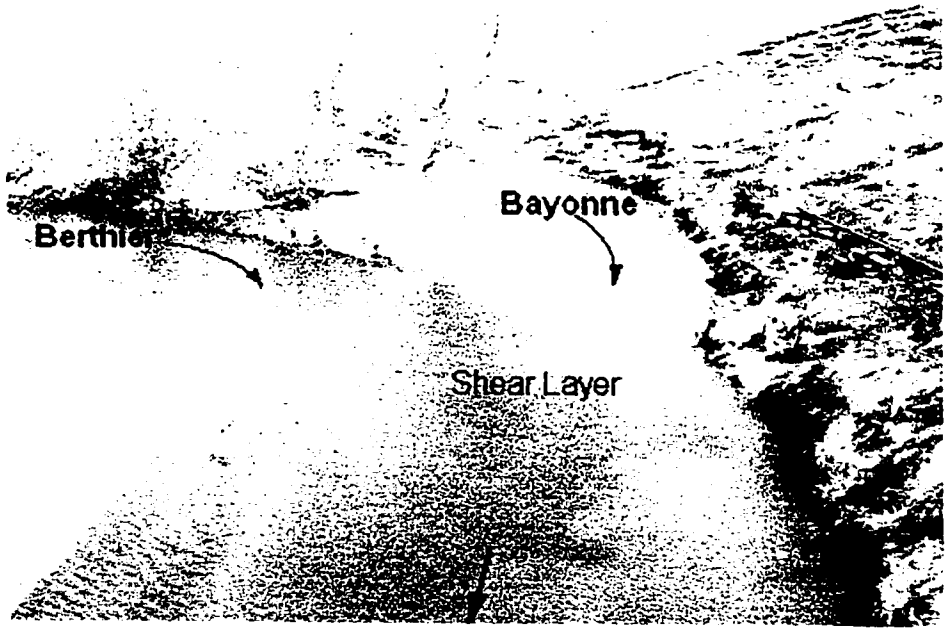

Figure 4.2 Bayonne-Berthier confluence

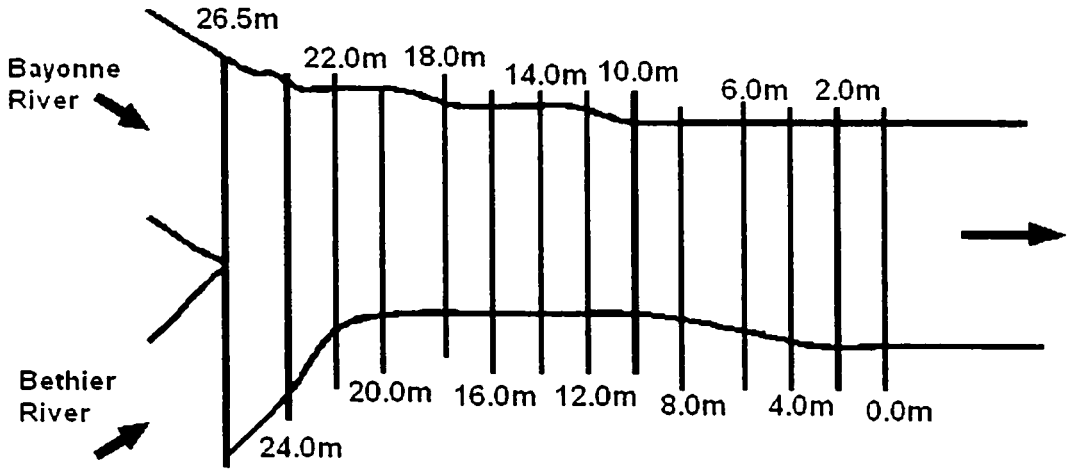

Figure 4.3 Cross-sections of the Bayonne-Berthier confluence where bed topography data were collected

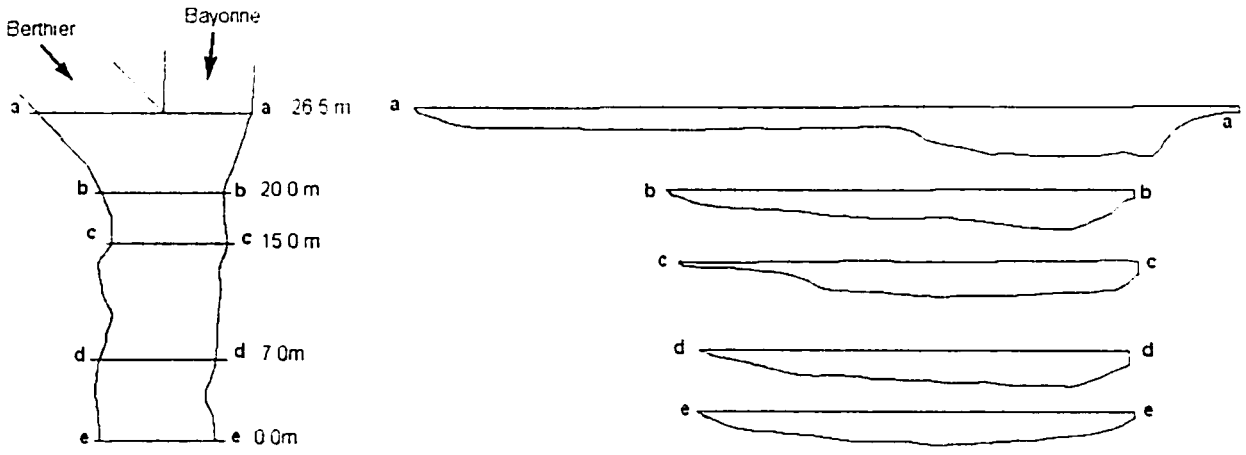

Figure 4.4 Geometry of the cross-sections where velocity data were collected

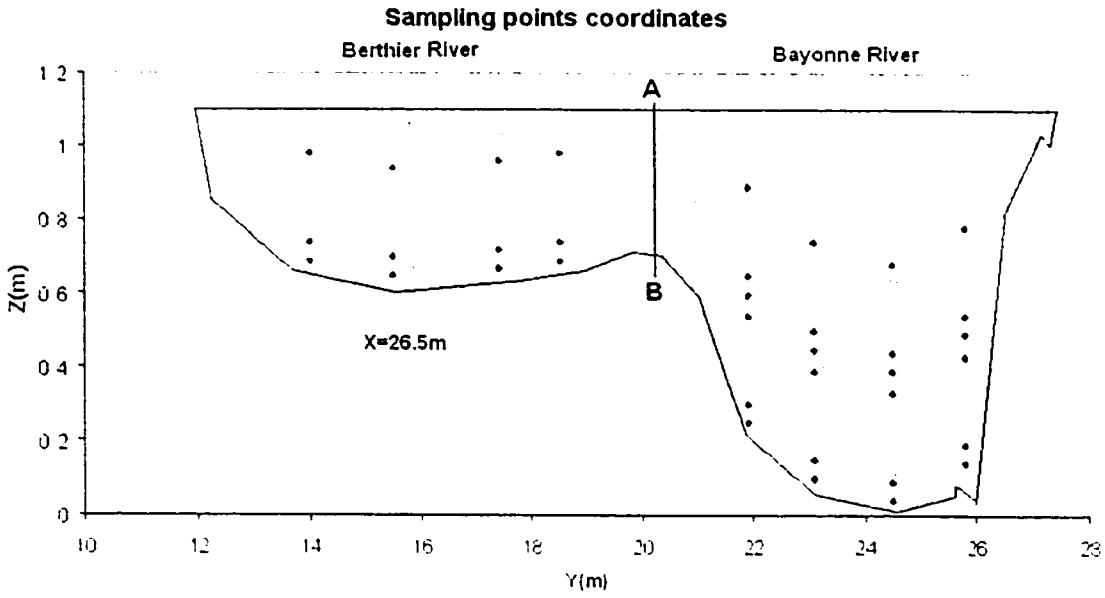

Figure 4.5 Coordinates of sampled velocity (x=26.5m)

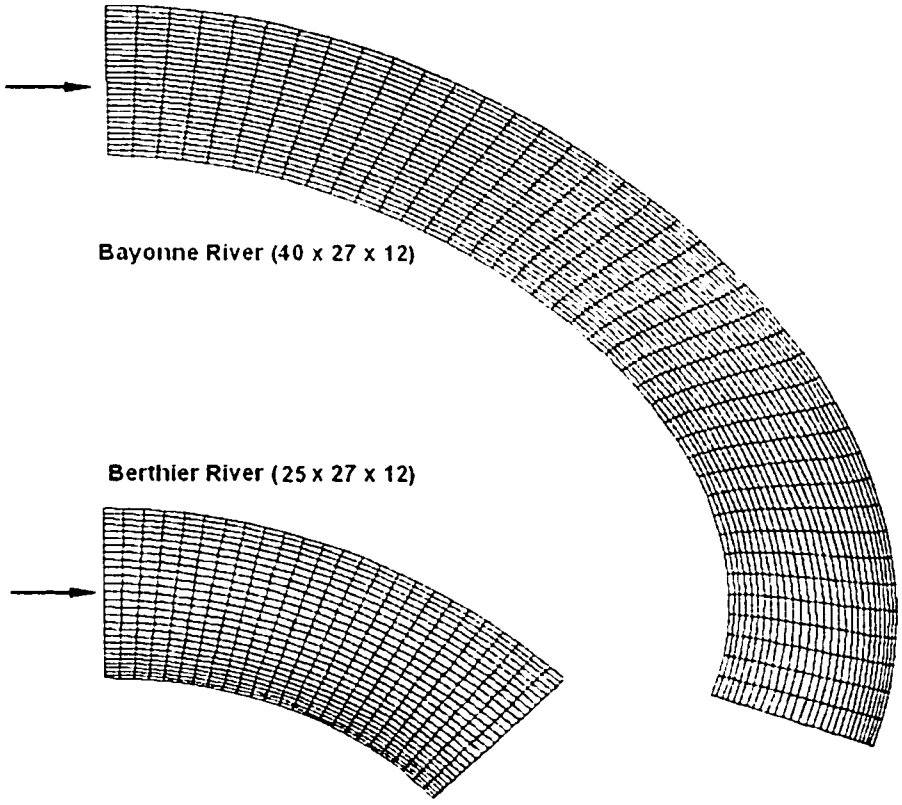

Figure 4.6 Grids of the Bayonne and Berthier rivers

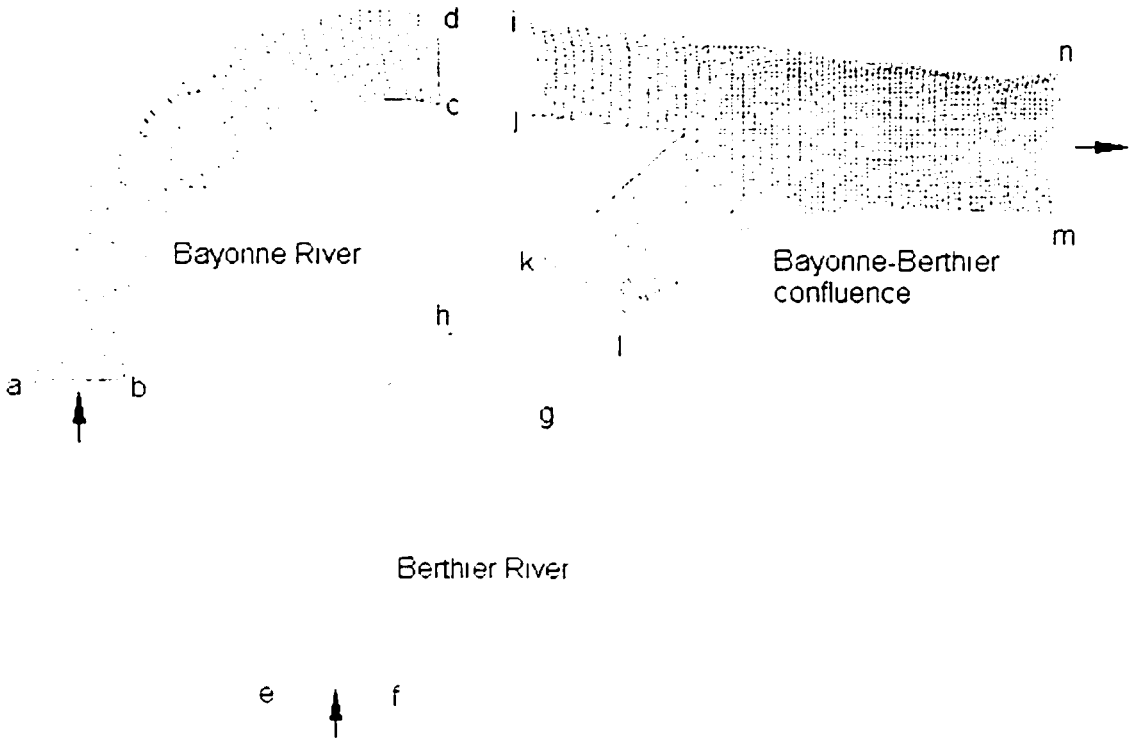

Figure 4.7 Grids of approaching rivers and the main confluence for Bayonne-Berthier confluence

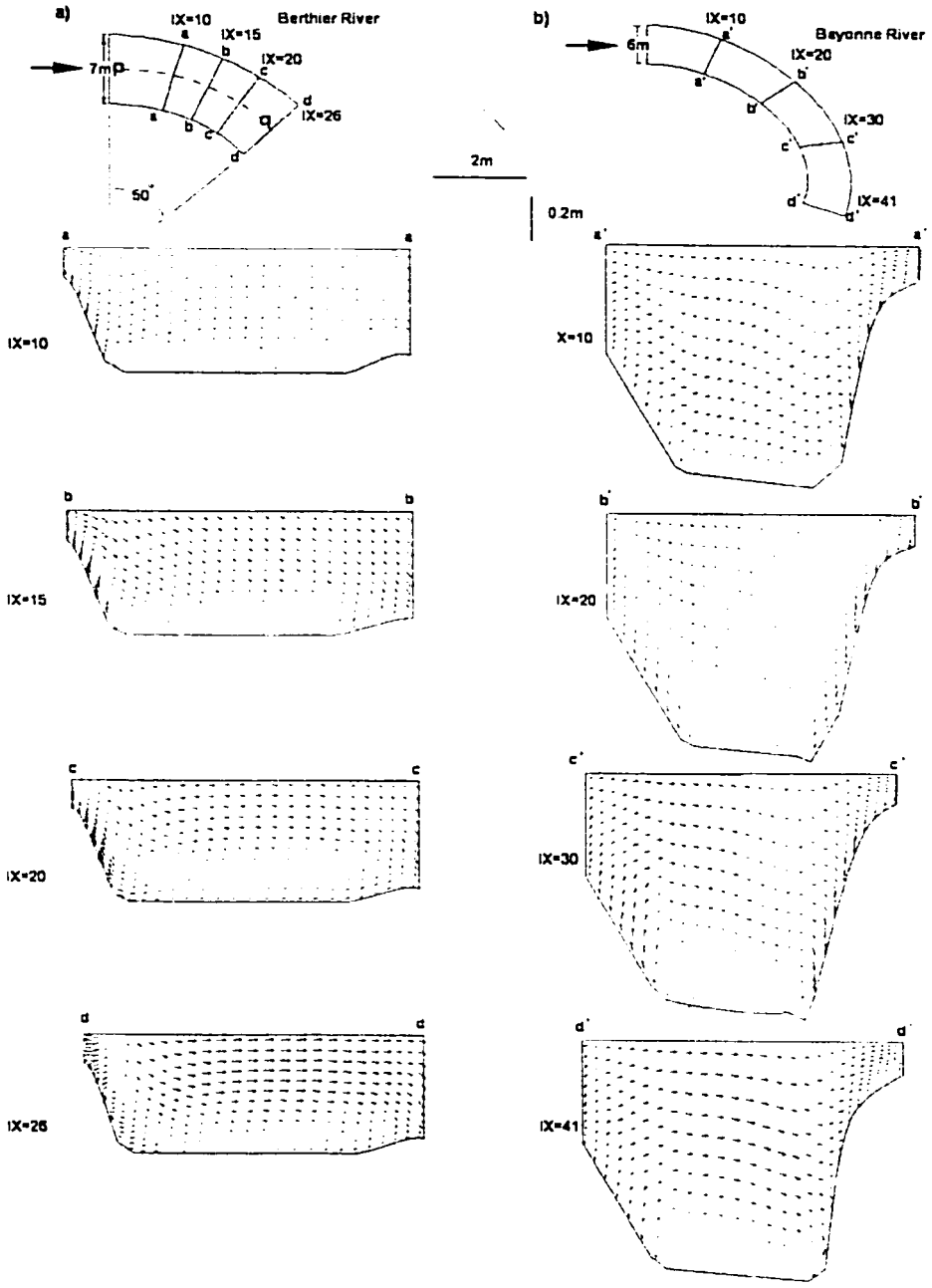

Figure 4.8 Velocity vector plots from the Bayonne and Berthier River simulation

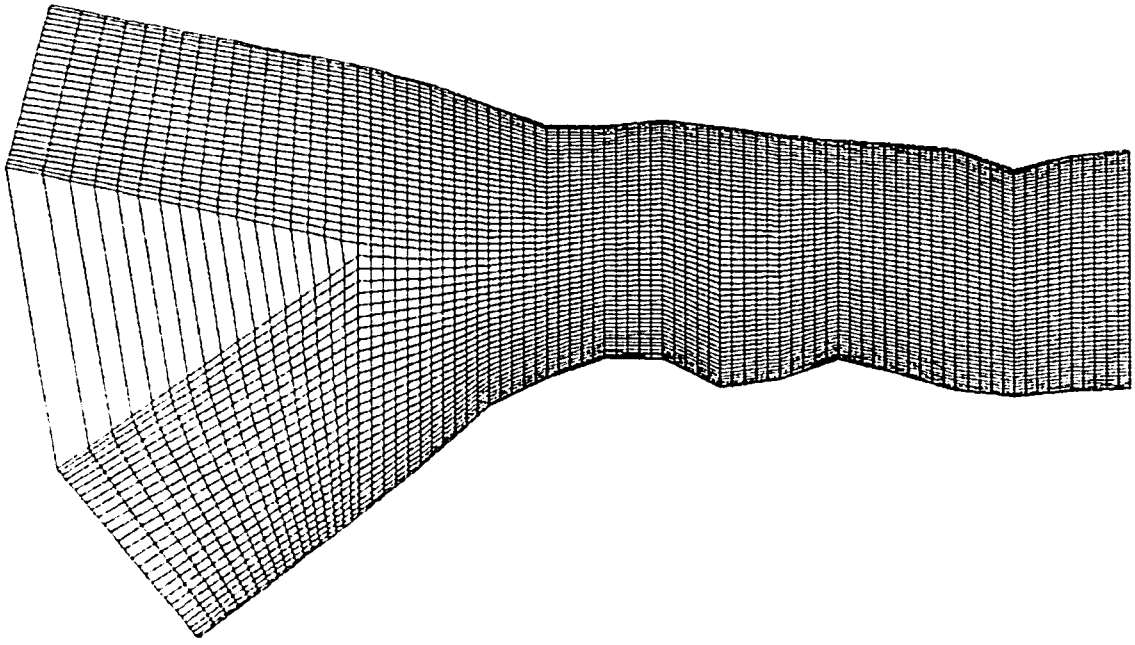

a) Grid 1

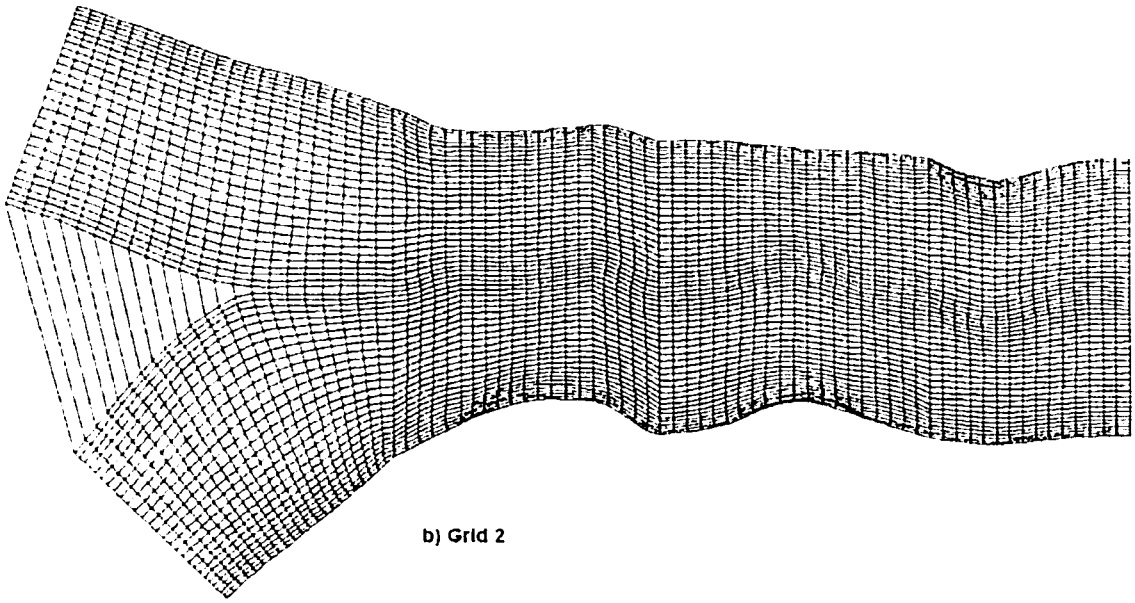

b) Grid 2

Figure 4.9 Two types of grids used for low flow condition simulation

a)

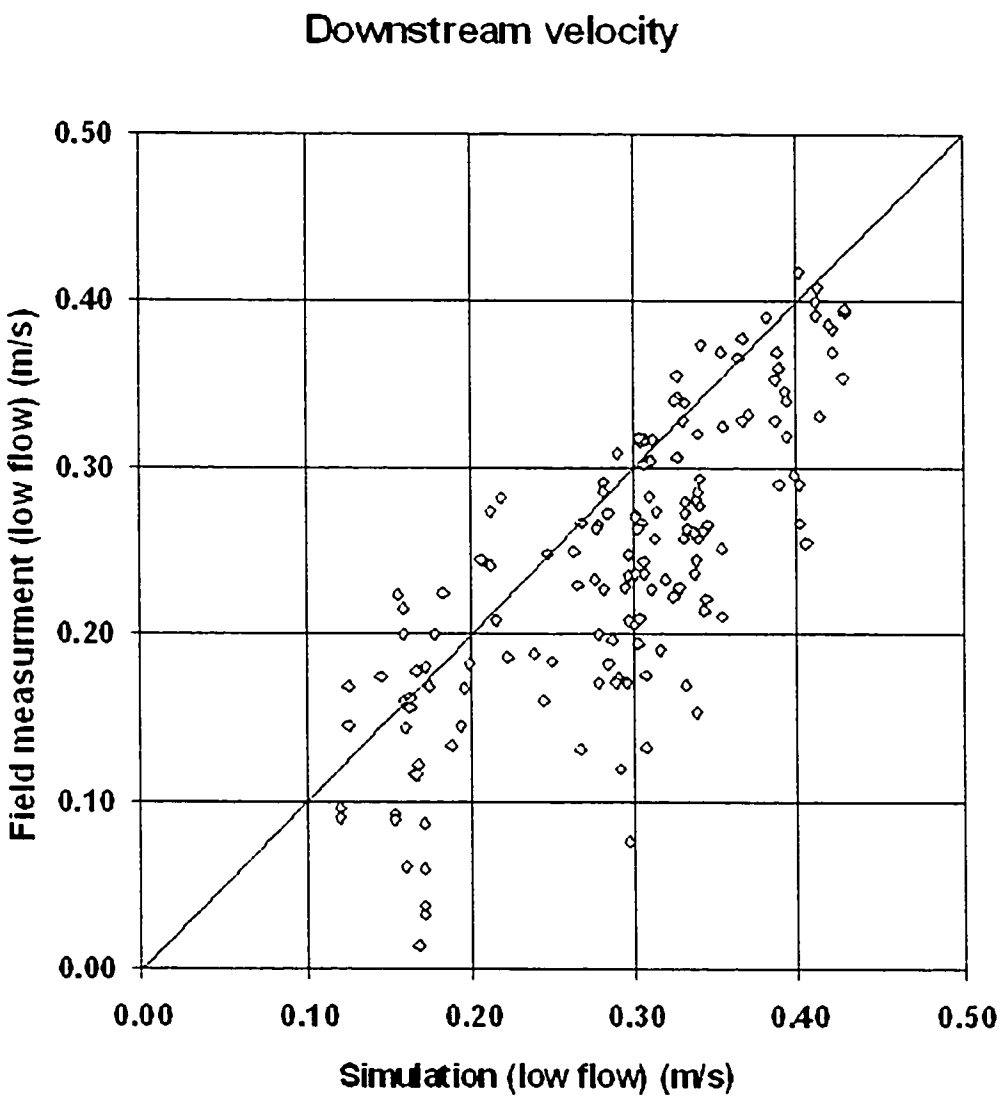
Downstream velocity
Field measurment (low flow) (m/s)
0.50
0.40
0.30
0.20
0.10
0.00
0.00
0.10
0.20
0.30
0.40
0.50
Simulation (low flow) (m/s)

b)

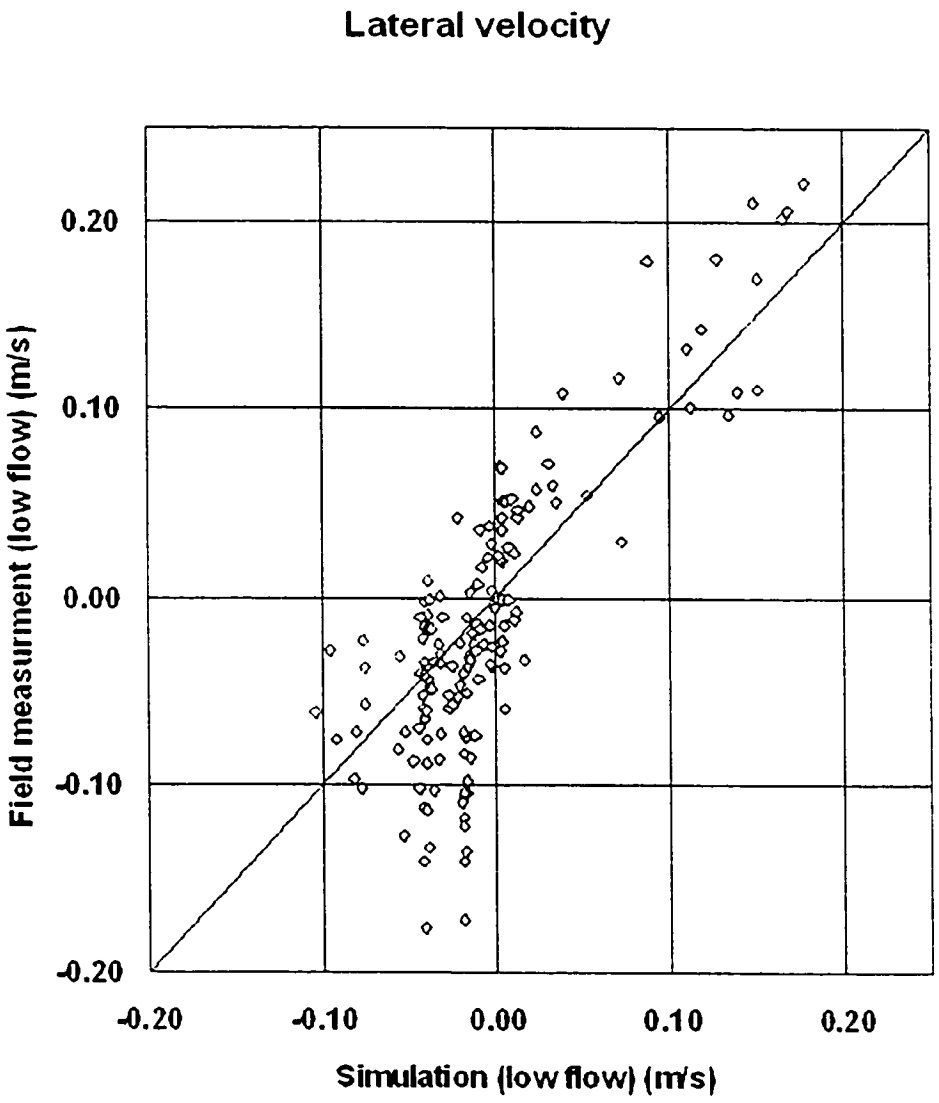
Lateral velocity
0.20
0.10
0.00
-0.10
-0.20
Field measurment (low flow) (m/s)
-0.20
-0.10
0.00
0.10
0.20
Simulation (low flow) (m/s)

c)

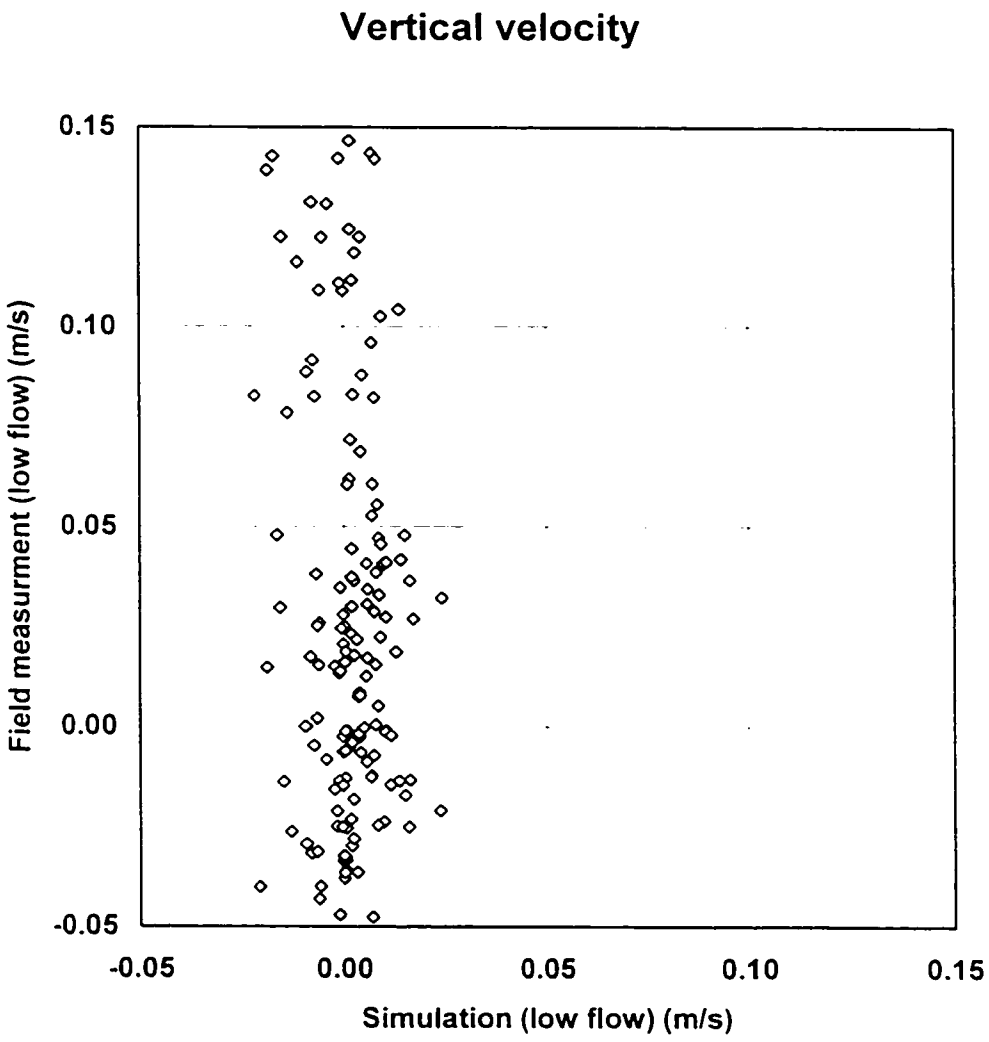

Figure 4.10 Comparison between simulation results and the field measurements for low flow condition; (a) downstream velocity; (b) lateral velocity; (c) vertical velocity

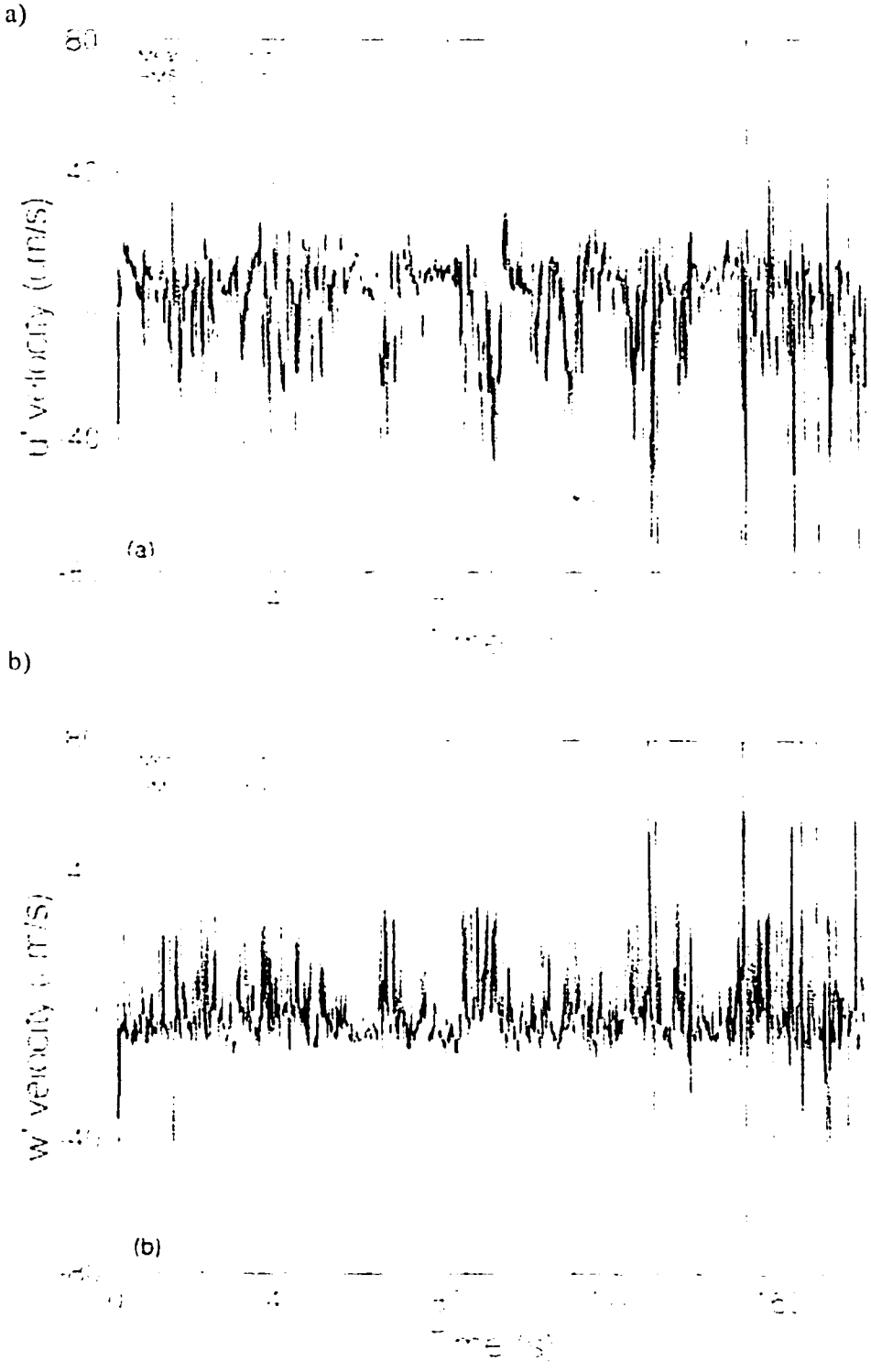

Figure 4.11 Simultaneous downstream (a) and vertical (b) components records for a sensor within the shear layer (Biron et al., 1993)

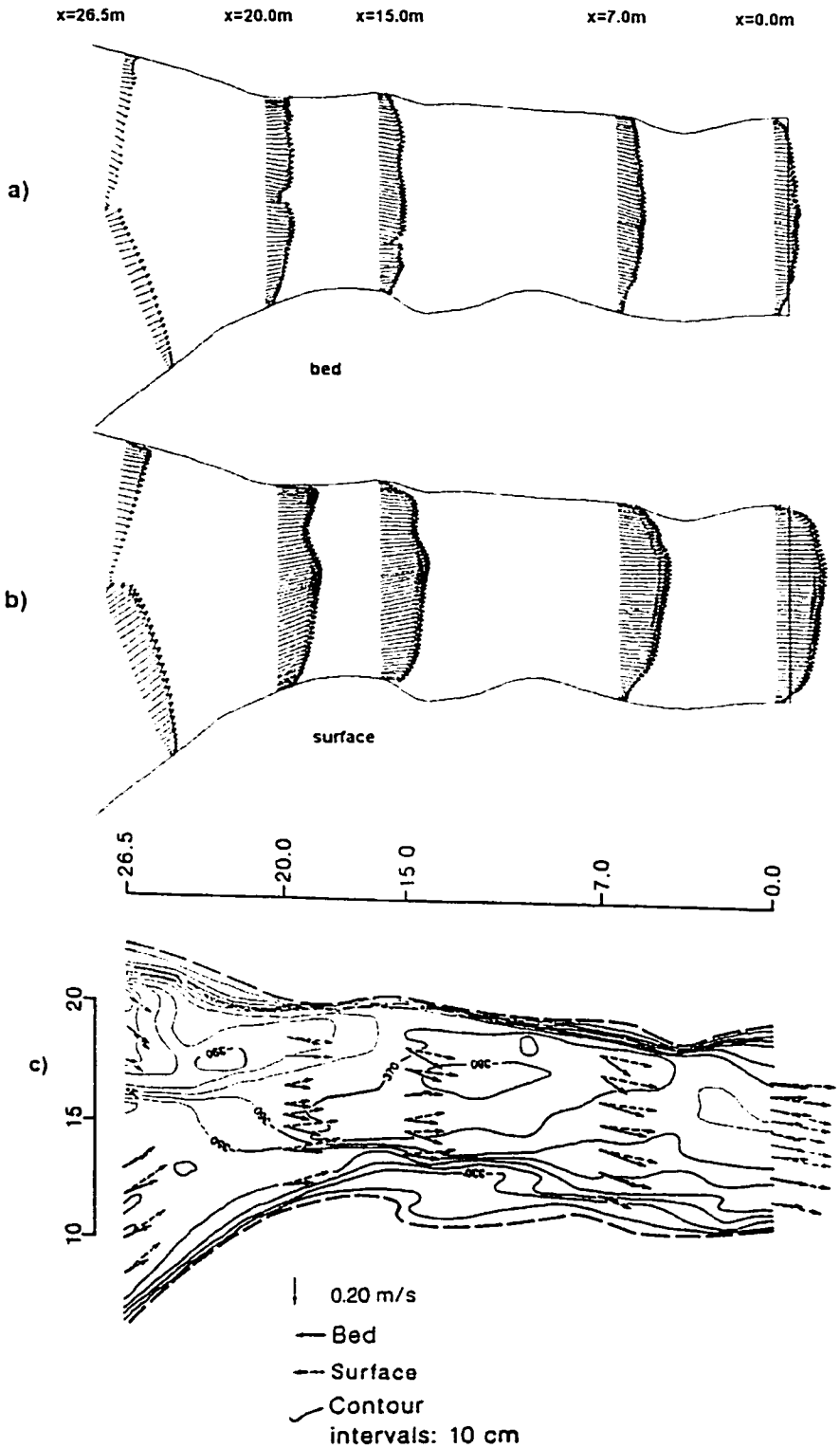

Figure 4.12 Comparisons of velocity vectors at the river bed and the water surface (low flow condition); (a) simulation at the bed; (b) simulation at the water surface; (c) field measurements at the bed and surface (De Serres et al., 1999)

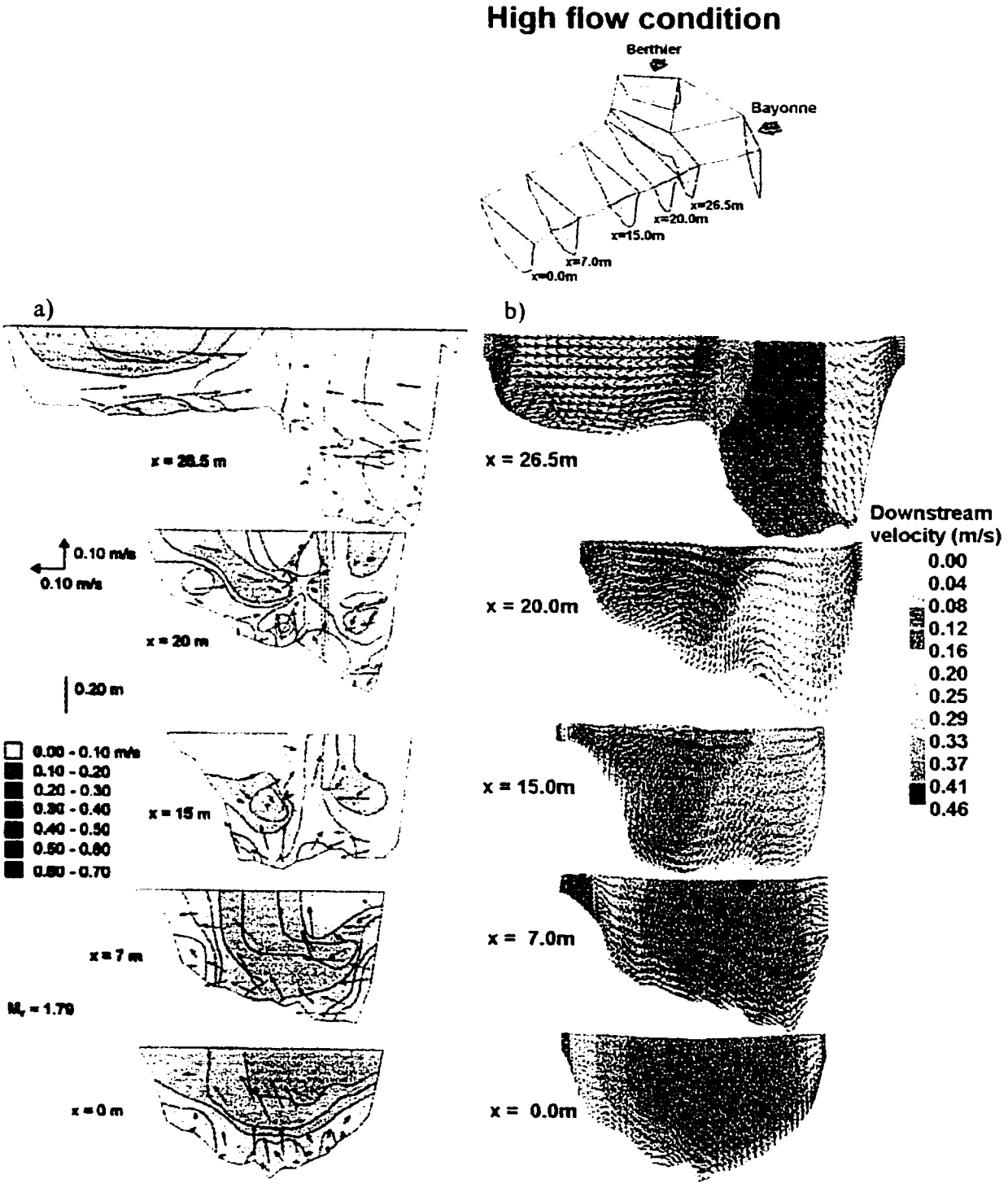

Figure 4.13 Comparison of three-dimensional velocity between a) field measurements (De Serres et al., 1999) and b) simulation for low flow condition (vectors: lateral and vertical velocity, contours: downstream velocity)

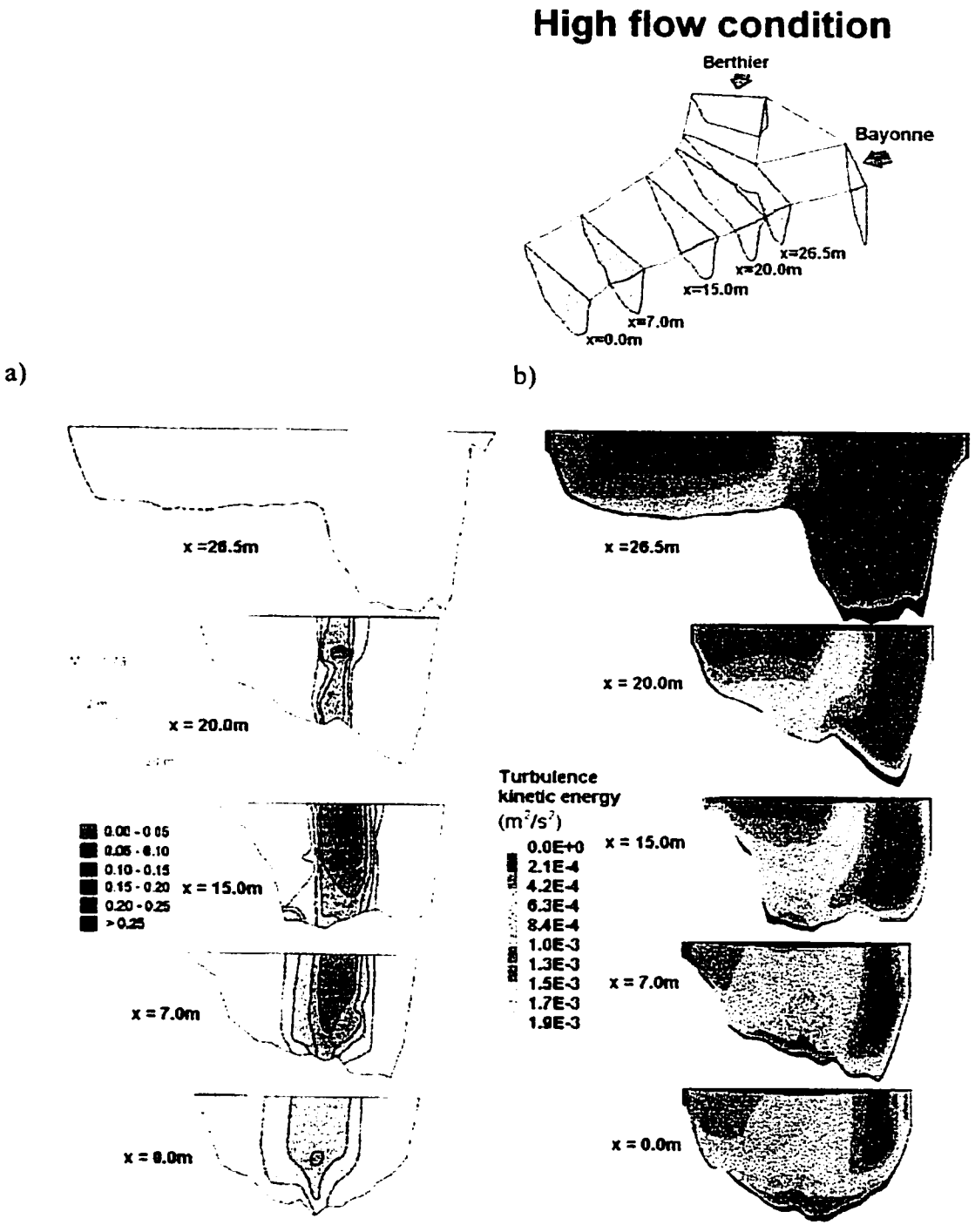

Figure 4.14 Comparison of turbulent kinetic energy between a) field measurements (De Serres et al., 1999) and b) simulation

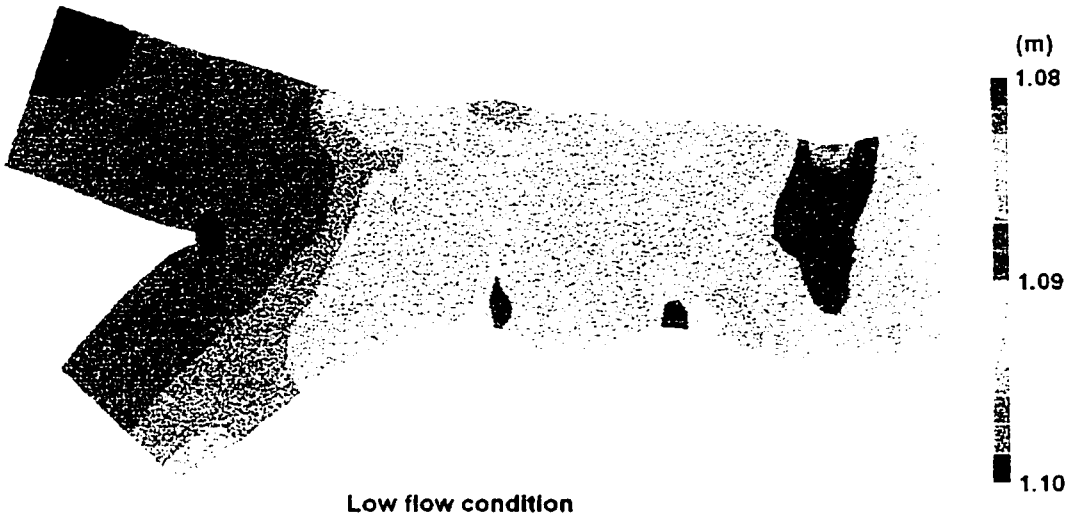

Figure 4.15 Predicted water surface profile for low flow condition

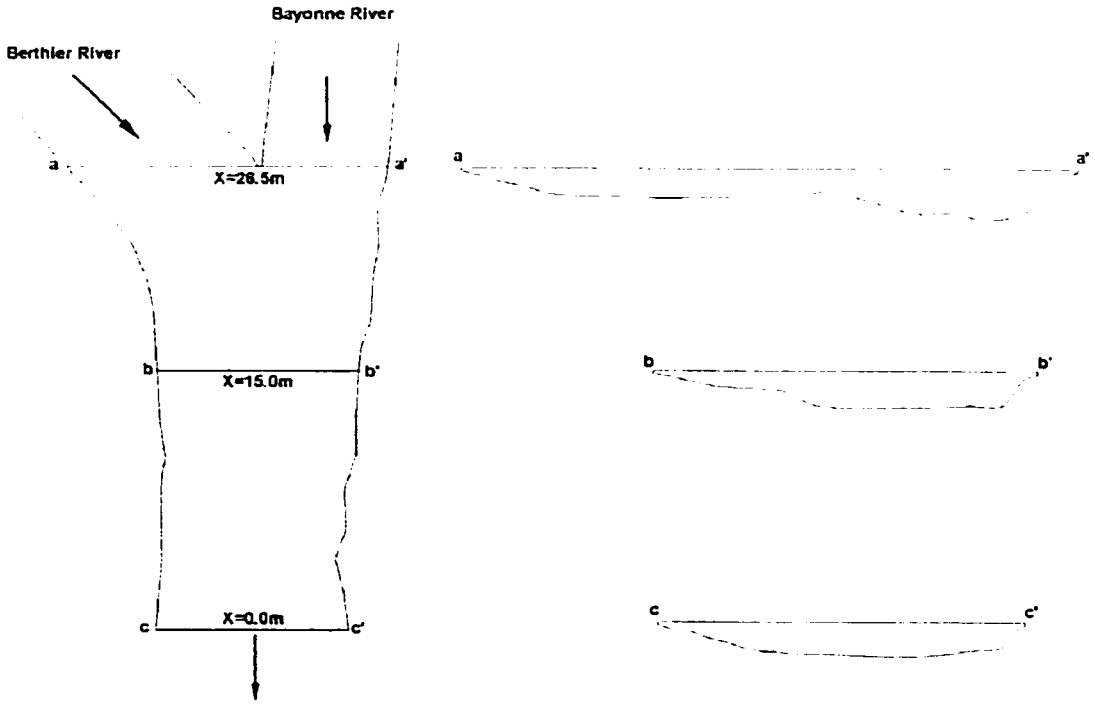

Figure 4.16 Cross sections for velocity data measurements of high flow condition

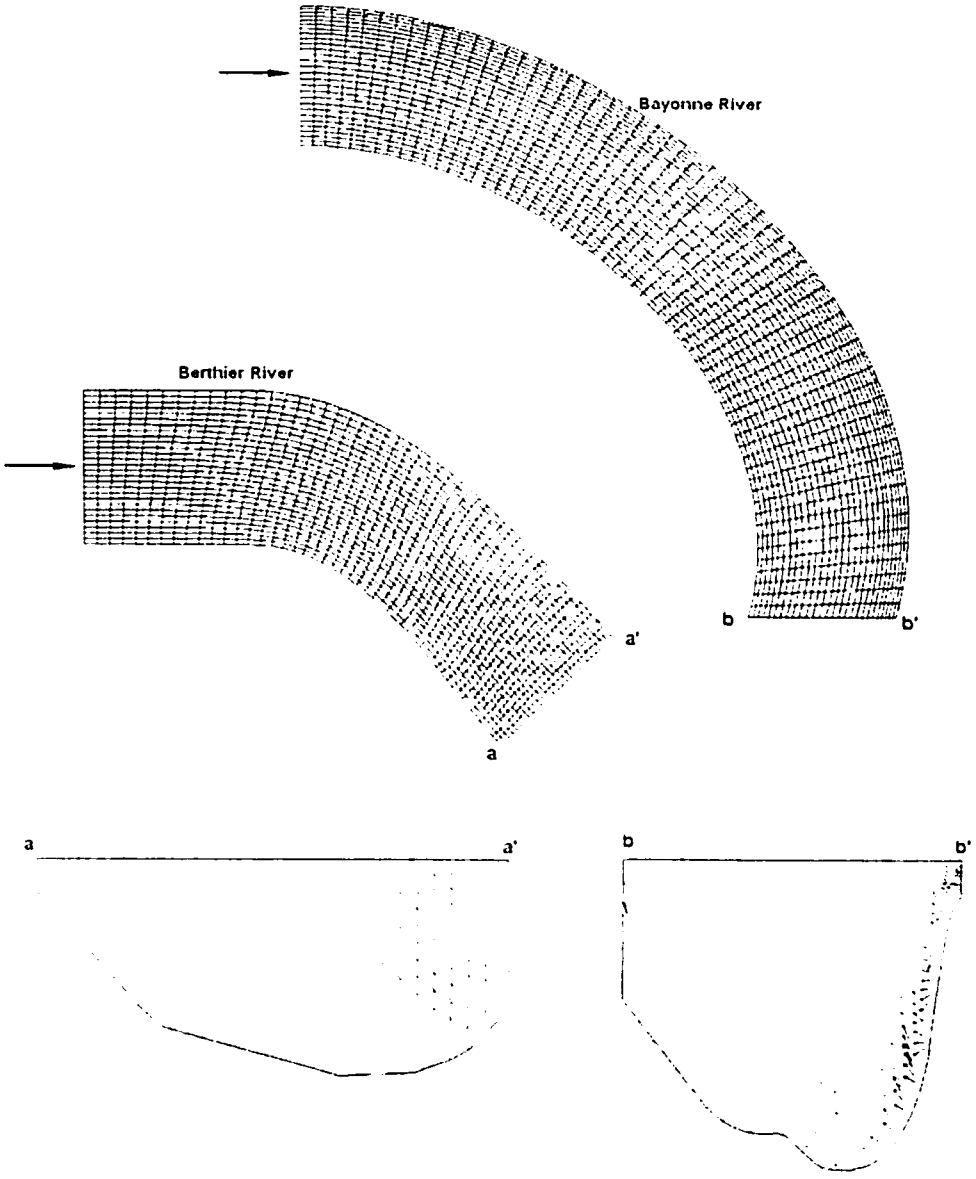

4.17 Grids for Bayonne and Berthier River and the flow pattern at the outlet

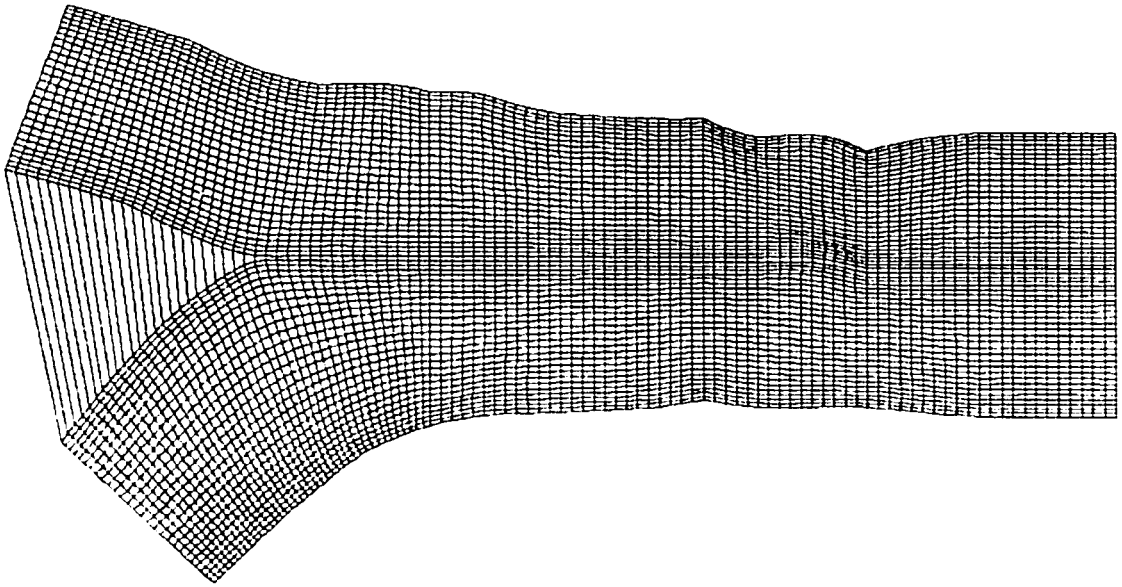

Figure 4.18 Grid for high flow condition

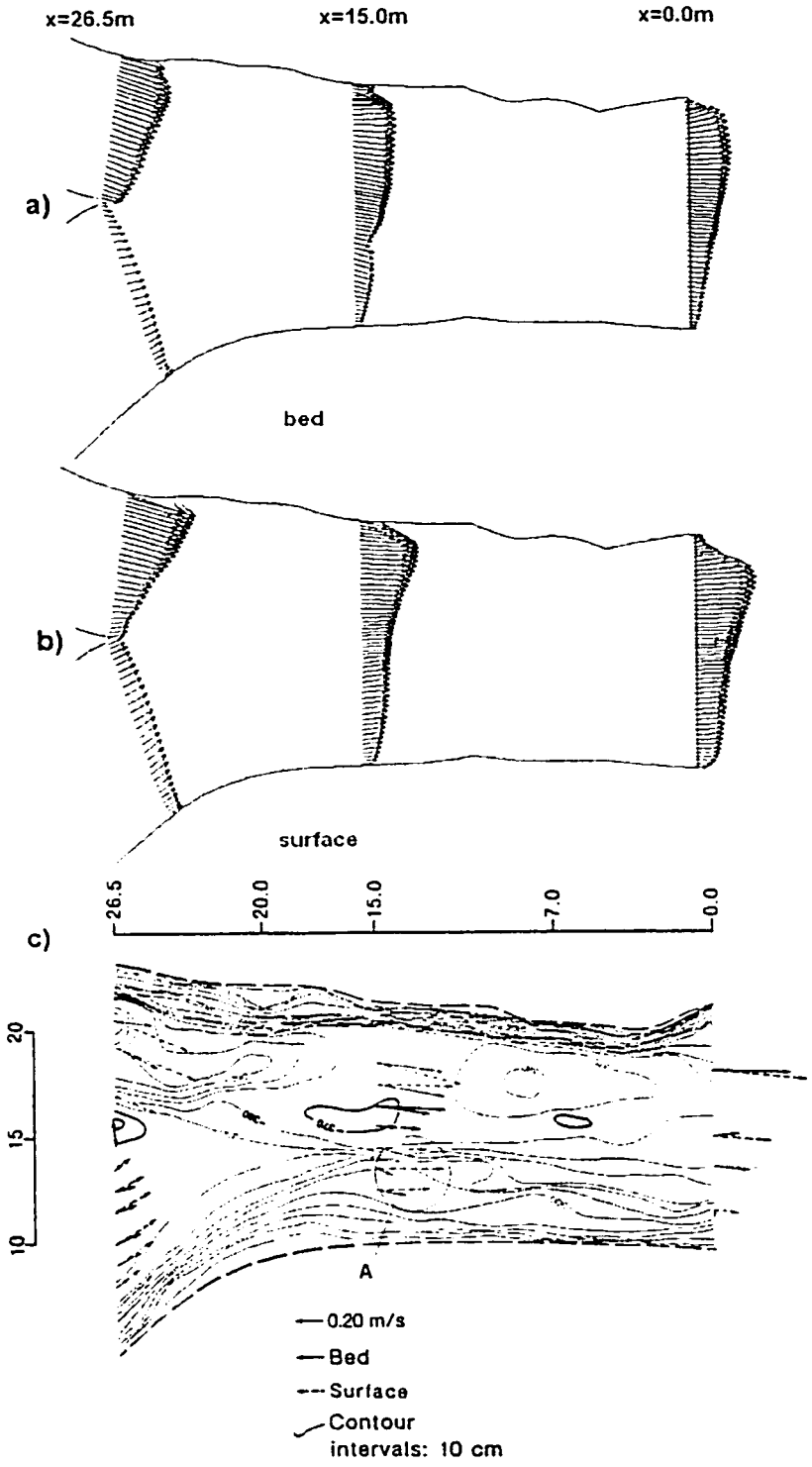

Figure 4.19 Comparison of flow field at water surface and river bed between simulation and field measurements for high flow condition; (a) simulation at the bed; (b) simulation at the water surface; (c) field measurements at the bed and surface (De Serres et al., 1999)

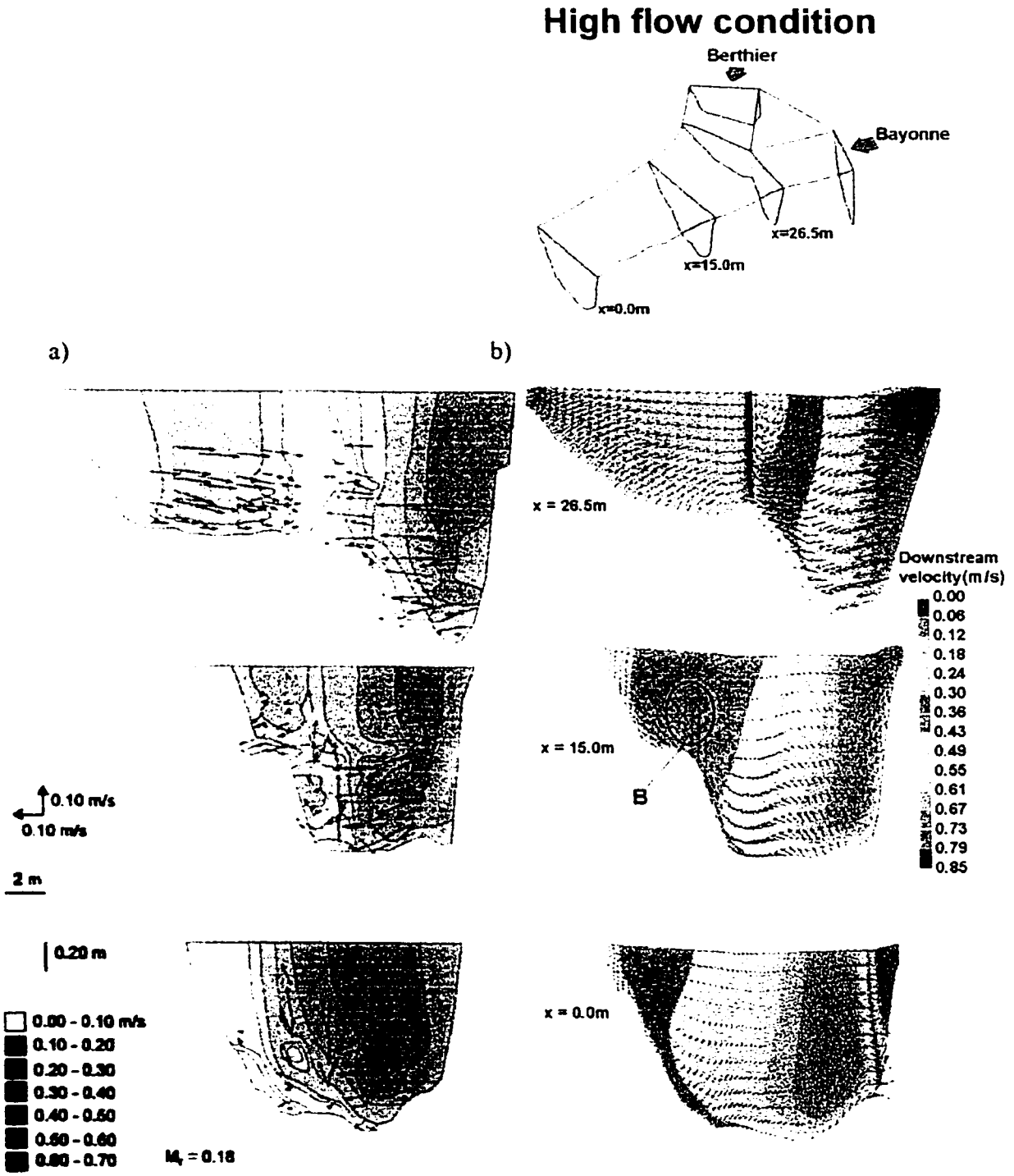

Figure 4.20 Comparison of three-dimensional velocity between a) field measurements (De Serres et al., 1999) and b) simulation for low flow condition (vectors: lateral and vertical velocity, contours: downstream velocity)

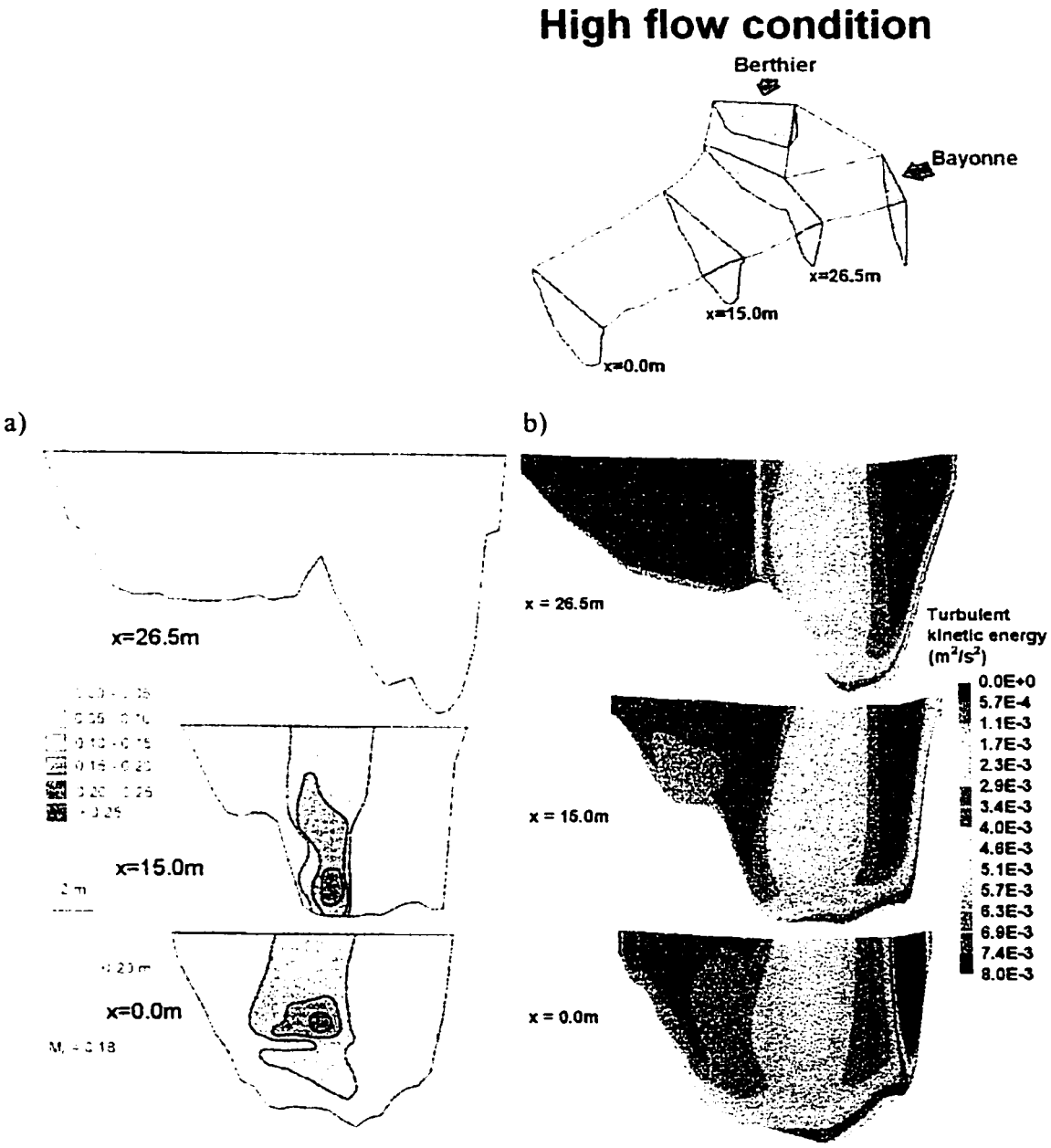

Figure 4.21 Comparison of turbulent kinetic energy between a) field measurements (De Serres et al., 1999) and b) simulation

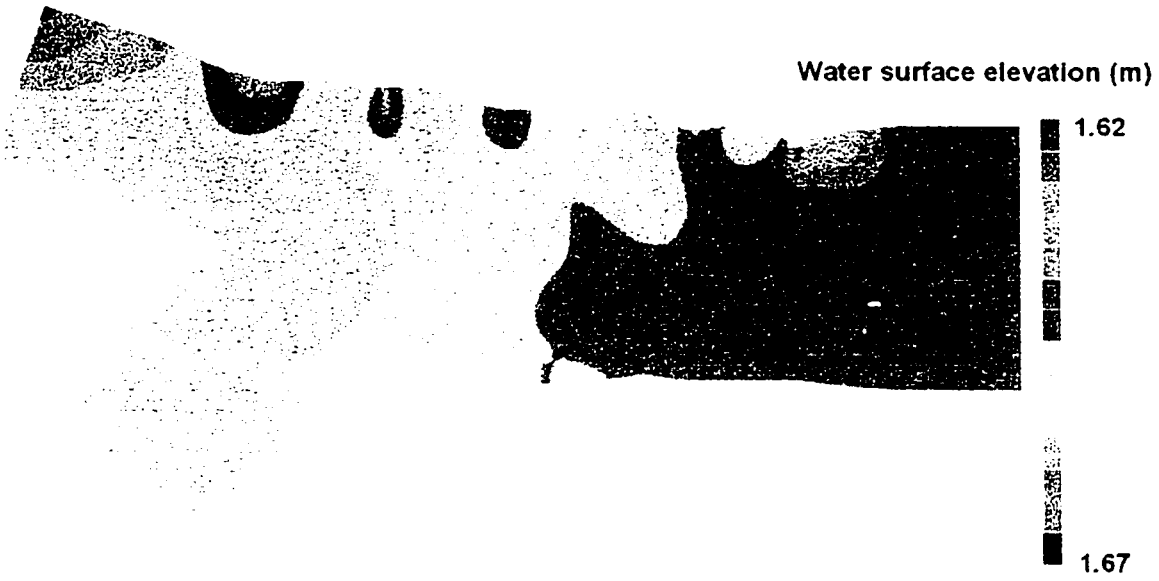

Figure 4.22 Water surface profile for high flow condition from simulation

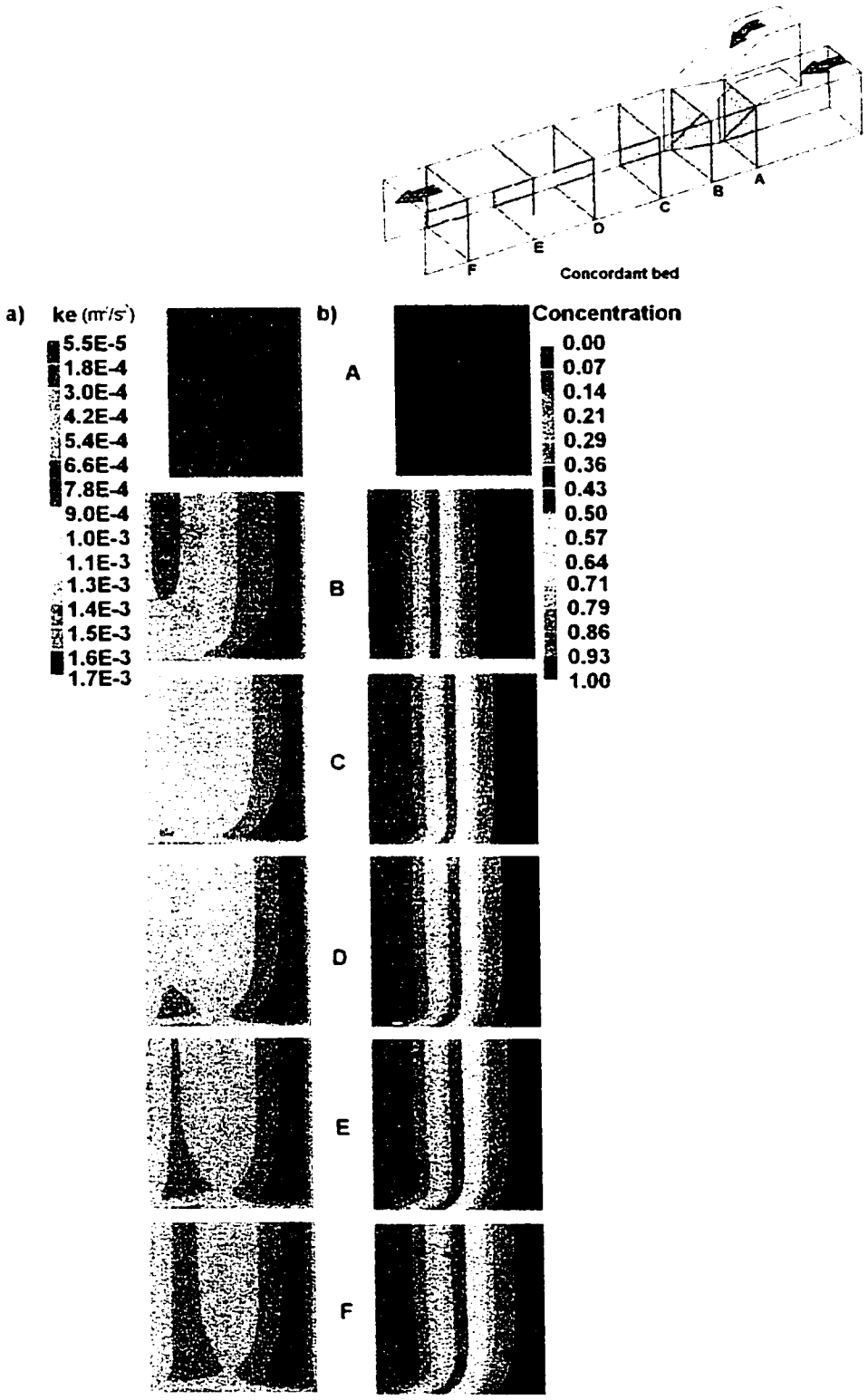

Figure 5.1 Contour plots of a) turbulent kinetic energy and b) concentration for concordant bed laboratory confluence

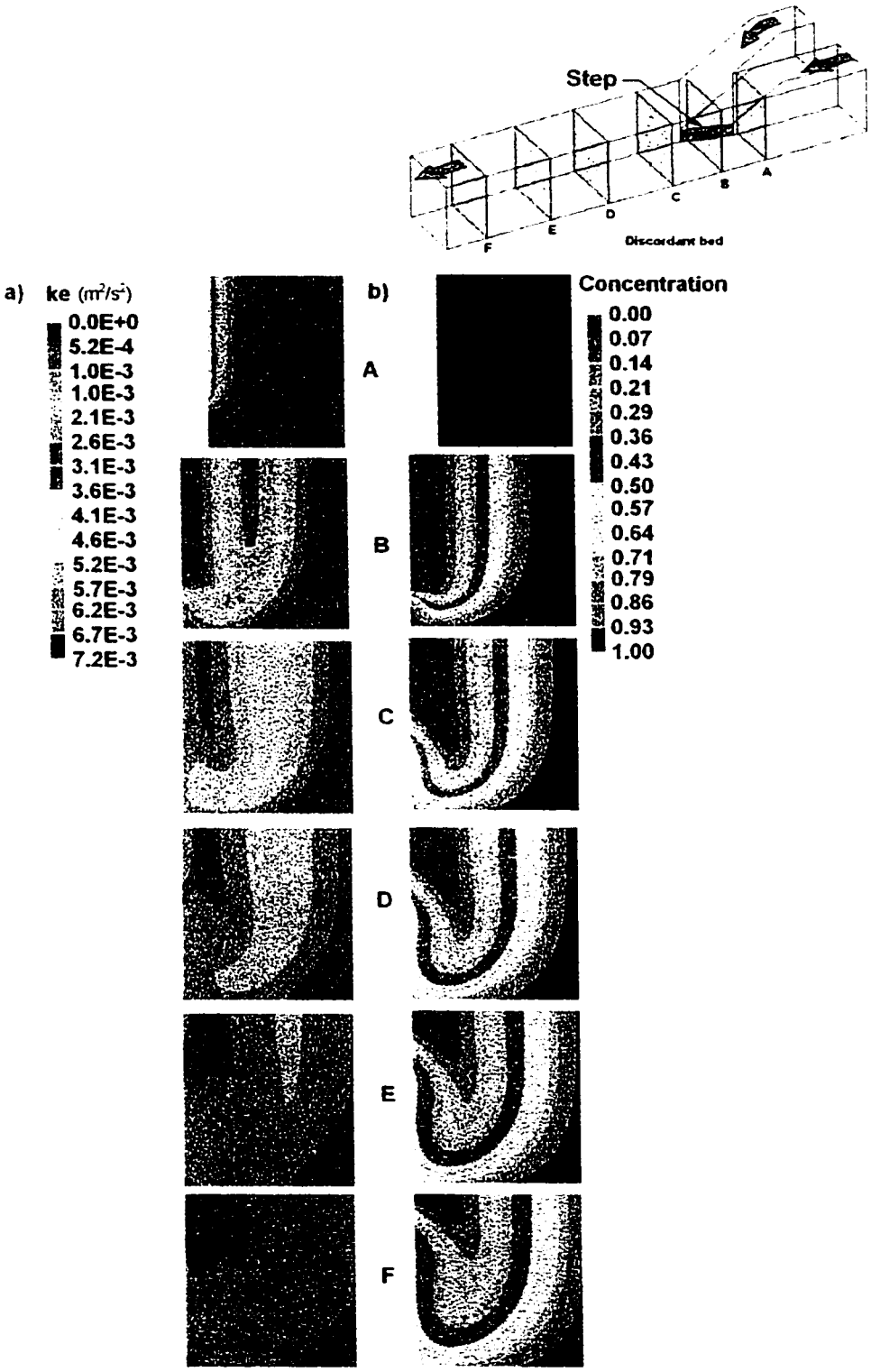

Figure 5.2 Contour plots of a) turbulent kinetic energy and b) concentration for discordant bed laboratory confluence

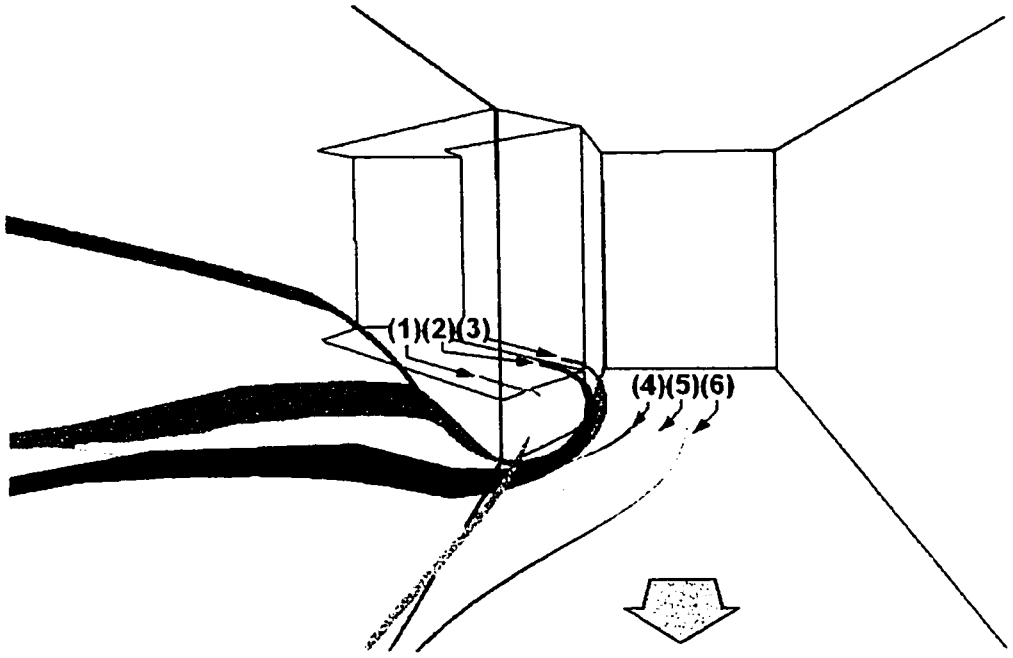

Figure 5.3 Streamlines for discordant bed confluence

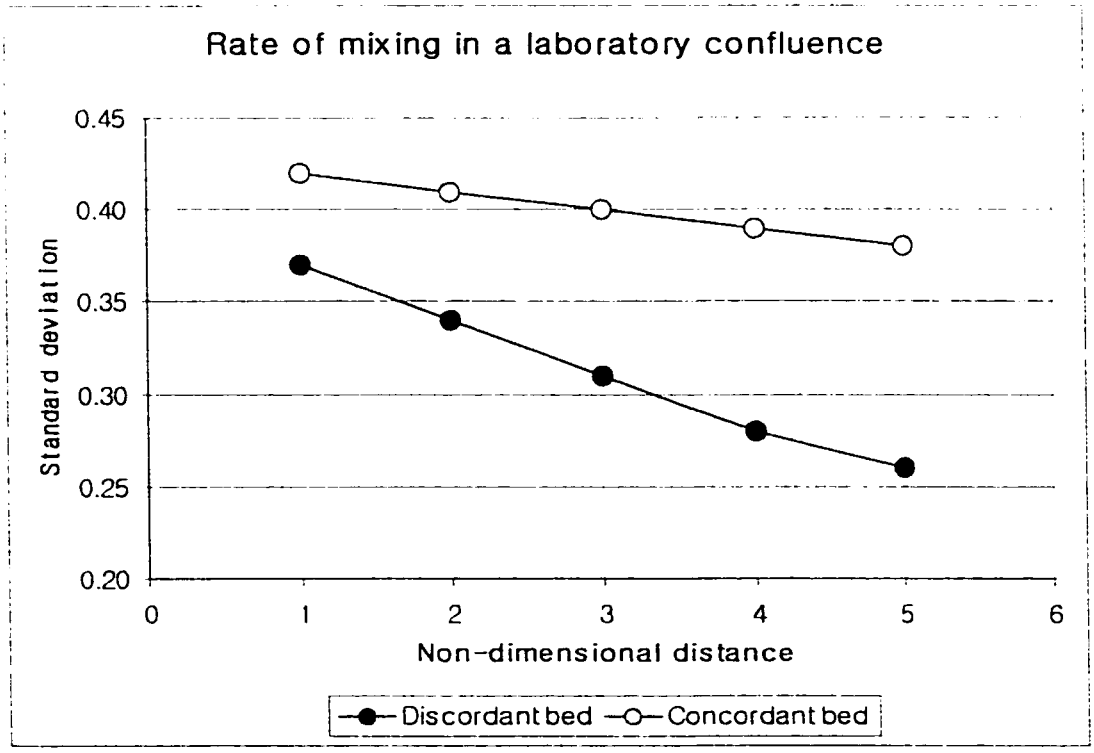

Figure 5.4 Mixing process comparison of laboratory confluences using standard deviation

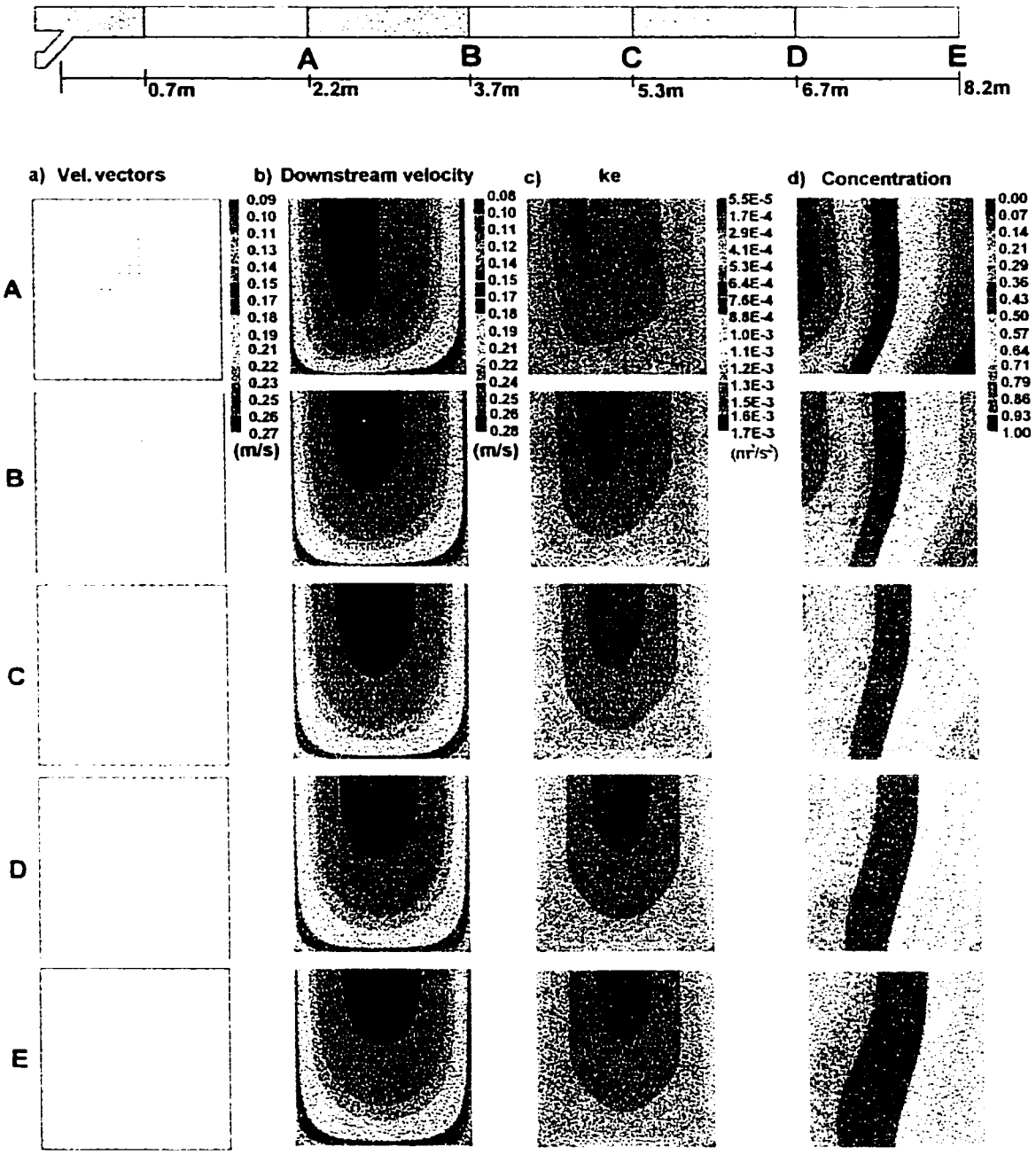

Figure 5.5 Plots of a) velocity vectors, b) contours of downstream velocity, c) turbulent kinetic energy (ke), and d) pollutant concentration (c1) for an extended channel of concordant bed confluence

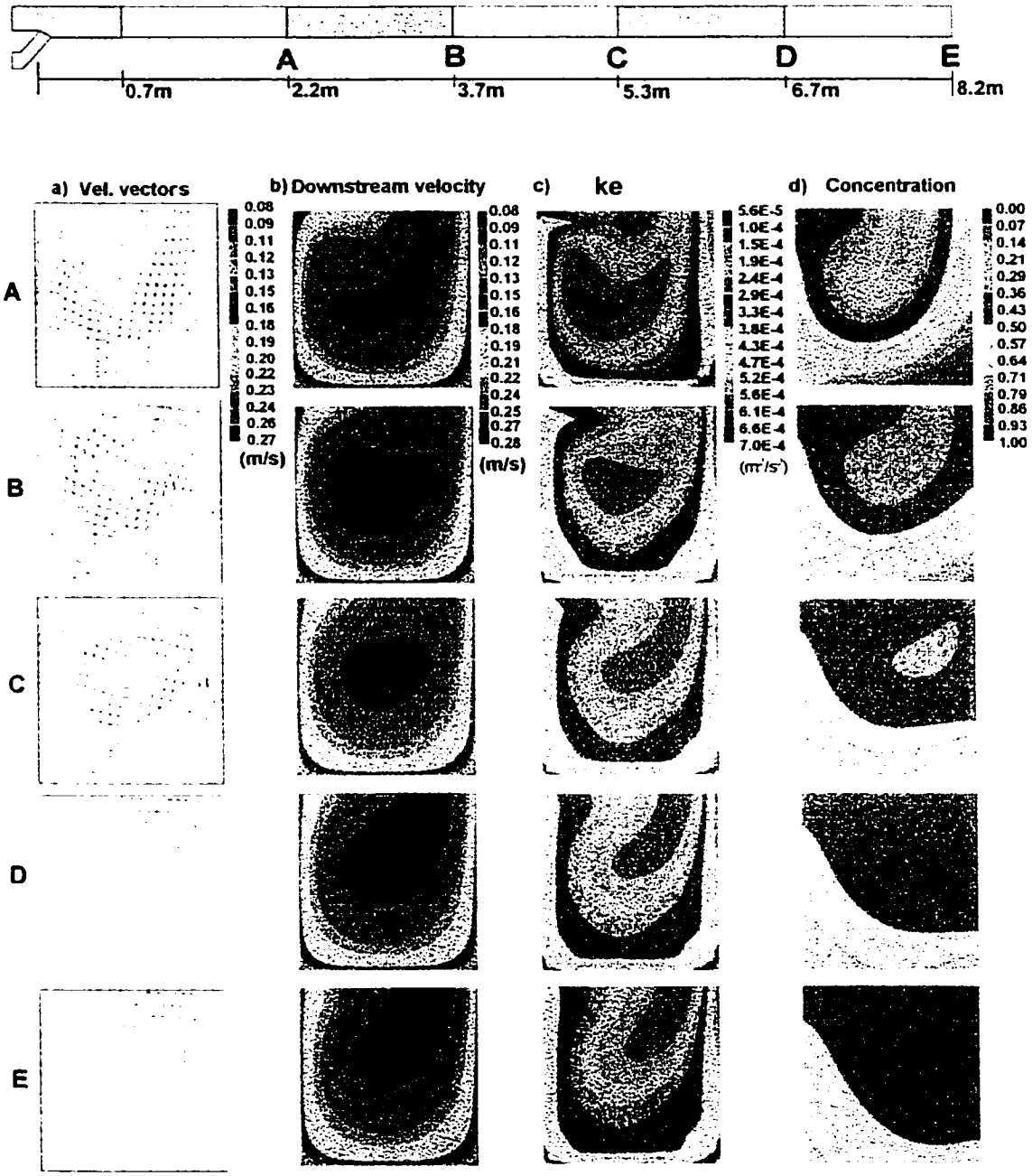

Figure 5.6 Plots of a) velocity vectors, b) contours of downstream velocity, c) turbulent kinetic energy (ke), and d) pollutant concentration (c1) for an extended channel of discordant bed confluence

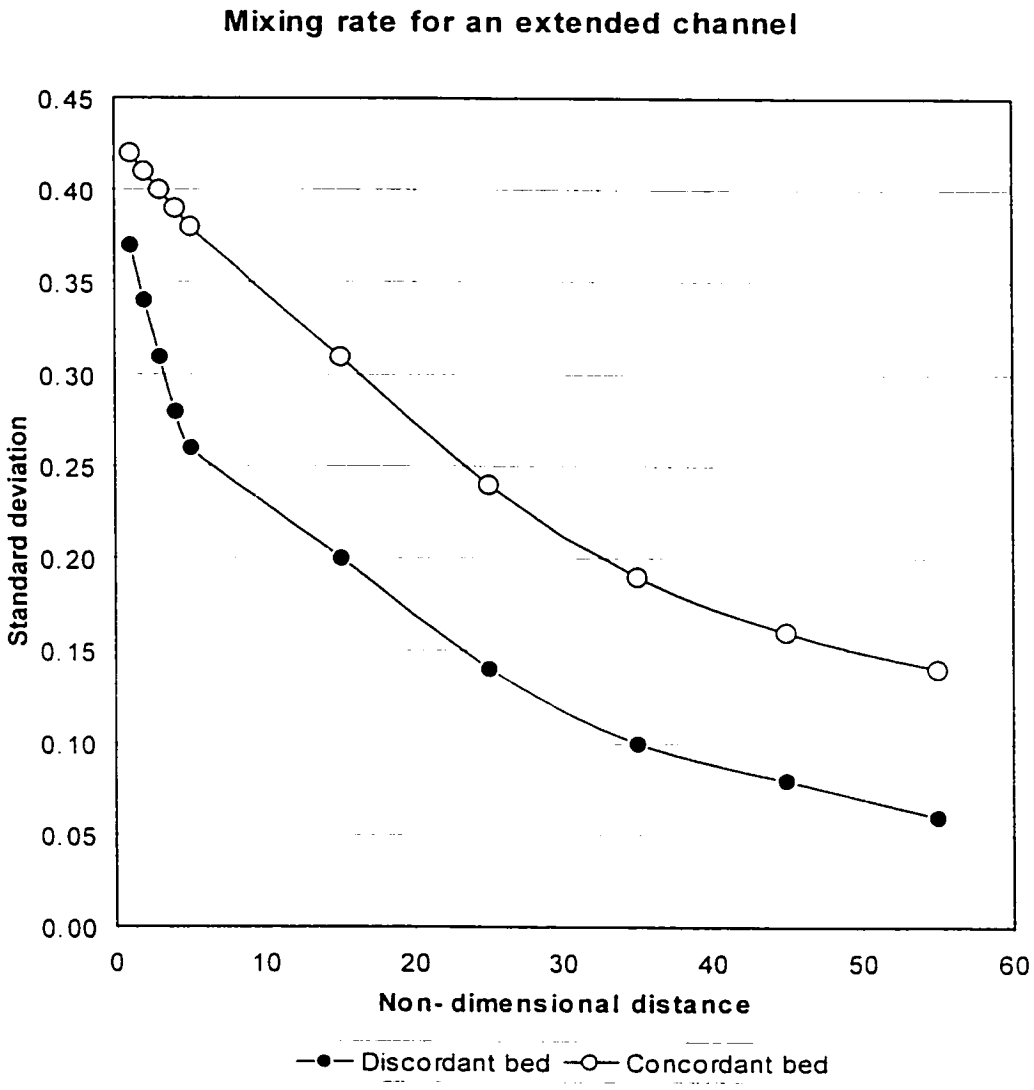

Figure 5.7 Comparison of the mixing process between concordant bed and discordant bed laboratory confluences using standard deviation of pollutant concentration

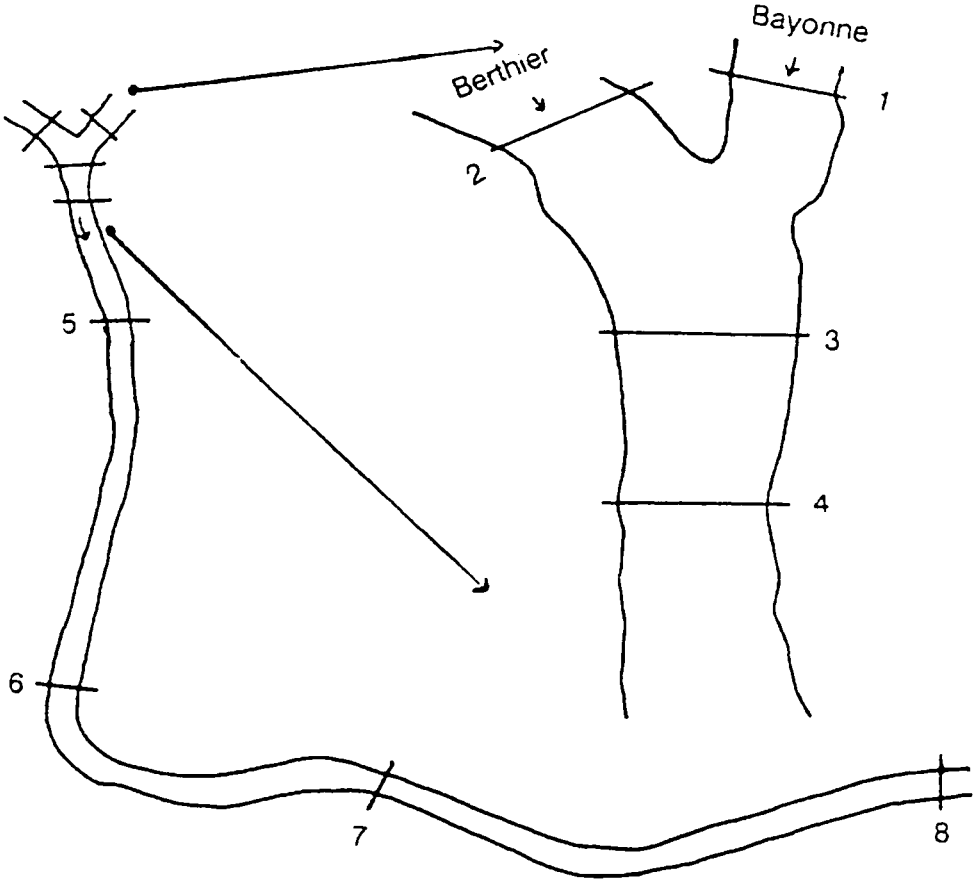

Figure 5.8 Map of the channel further downstream from the Bayonne-Berthier confluence (Gaudet, 1996)

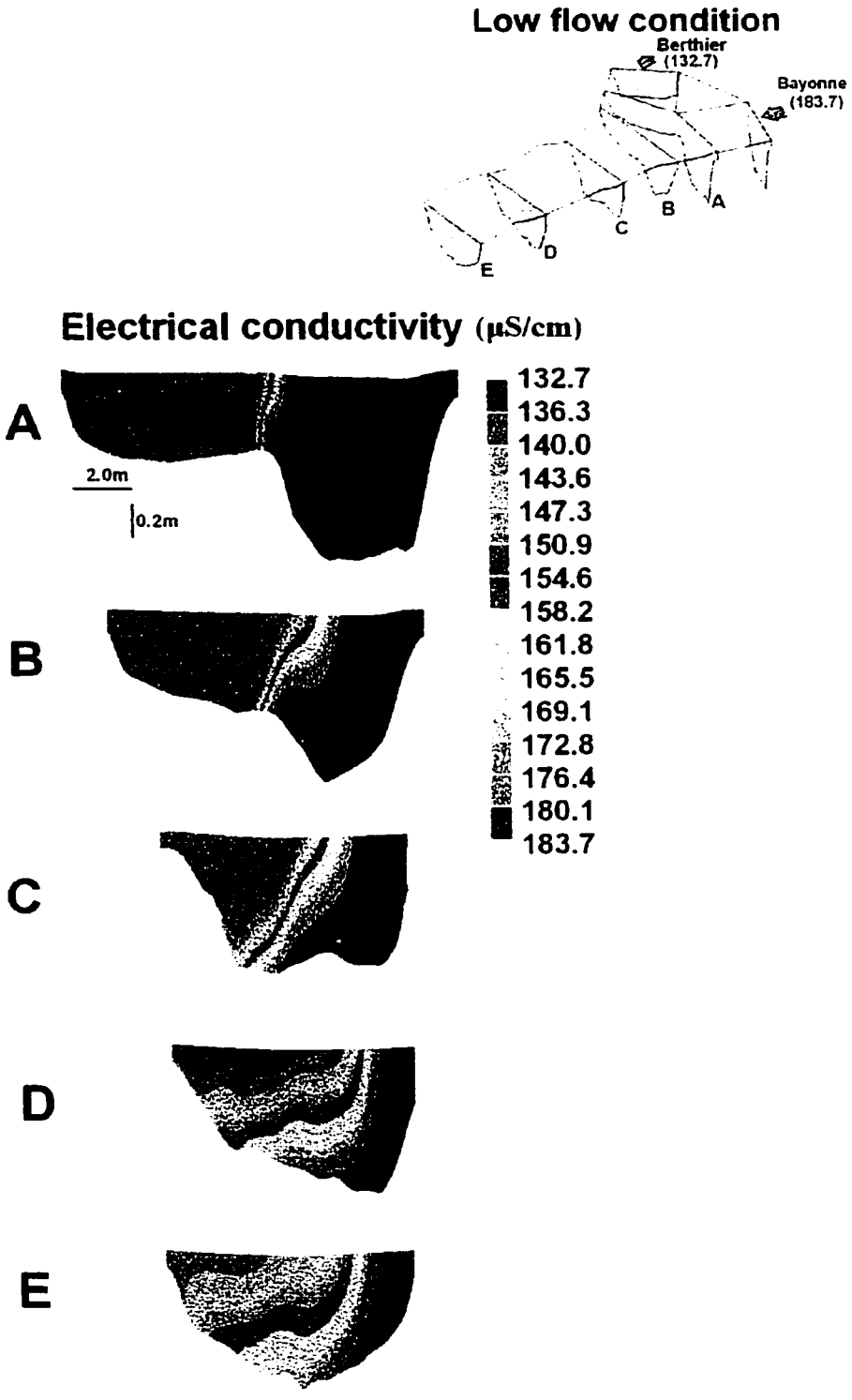

Figure 5.9 Contour plots of the predicted electrical conductivity from low flow simulation

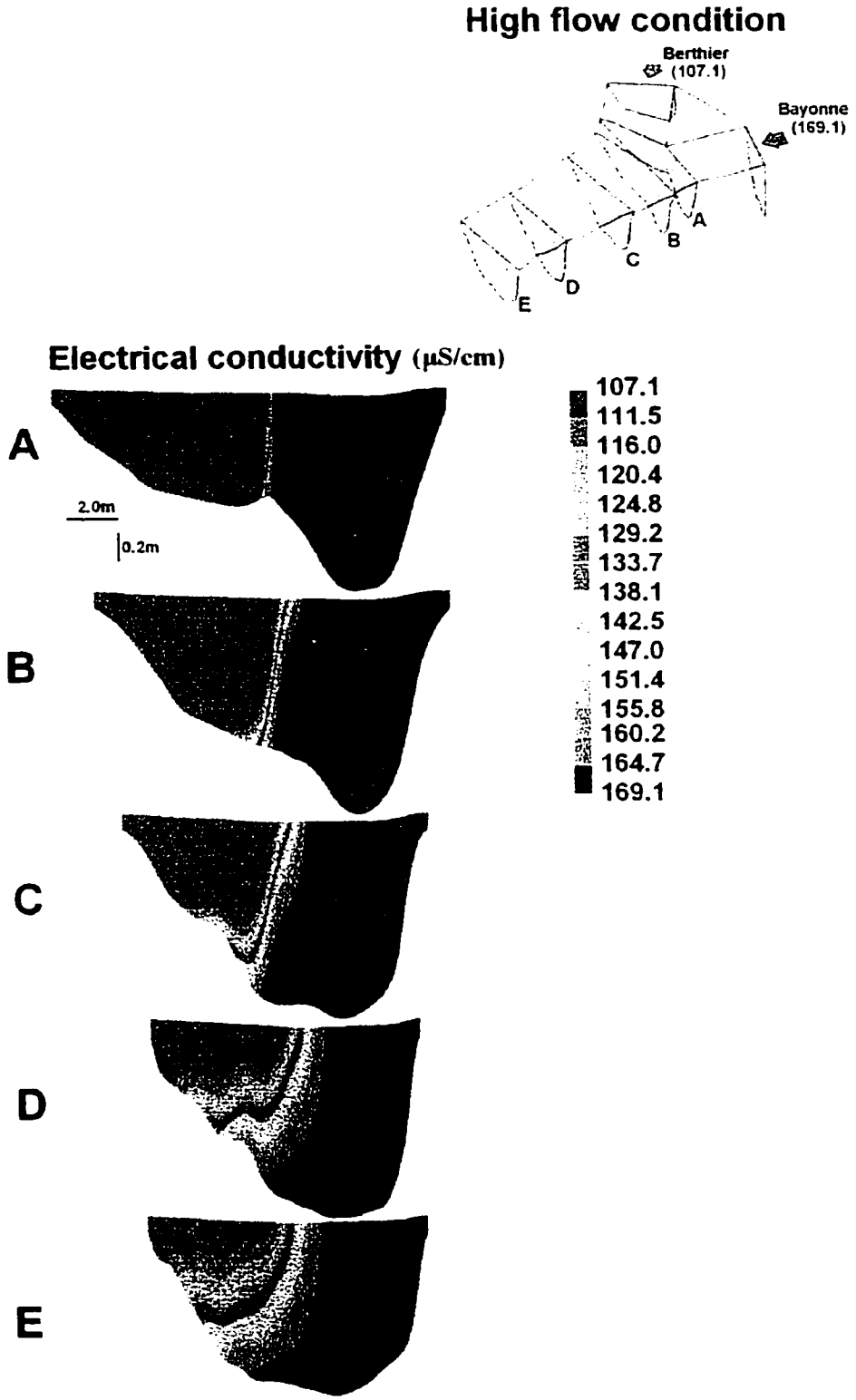

Figure 5.10 Contour plots of the predicted electrical conductivity from high flow simulation

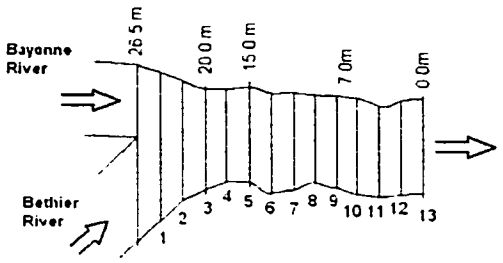

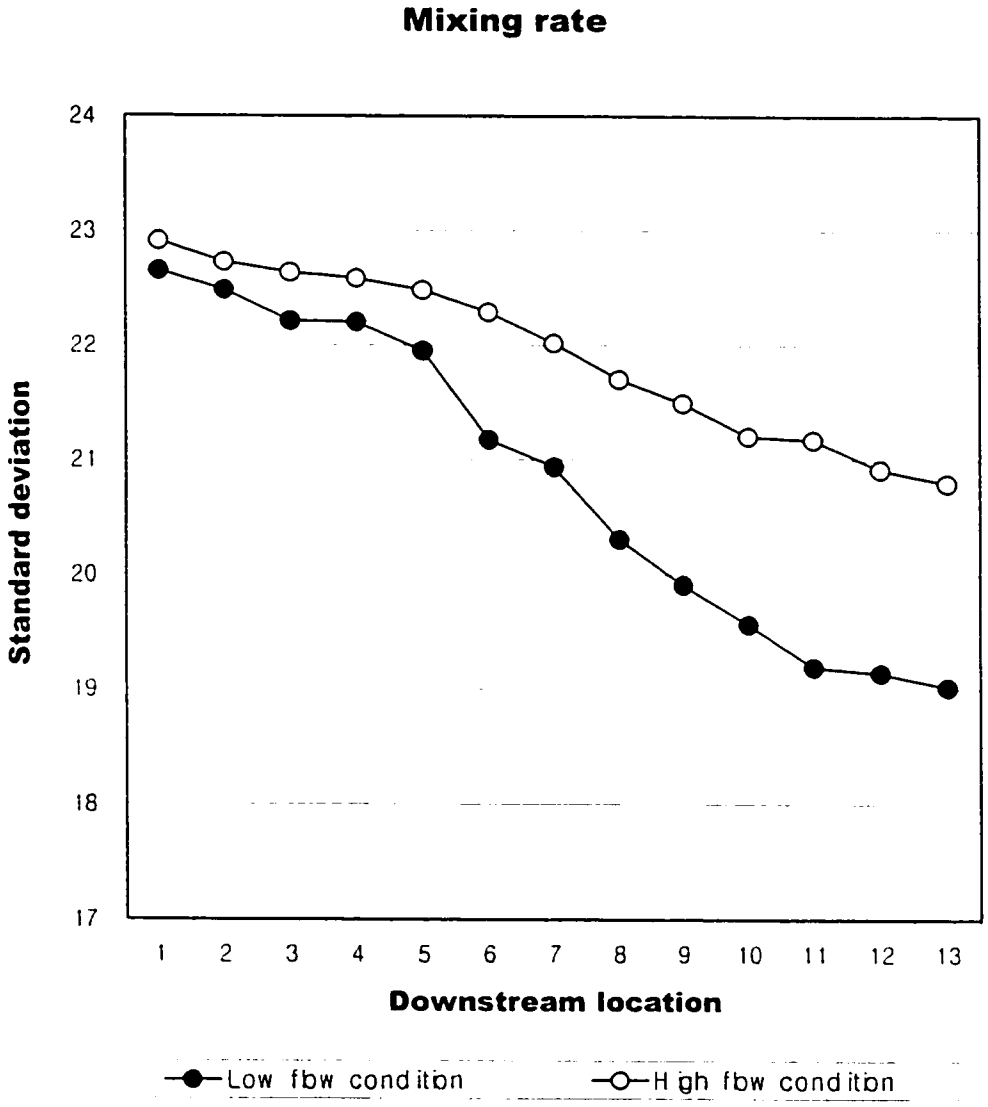

Figure 5.11 Mixing comparison between low and high flow condition for the Bayonne-Berthier confluence (downstream locations are shown as numbers in the map above)

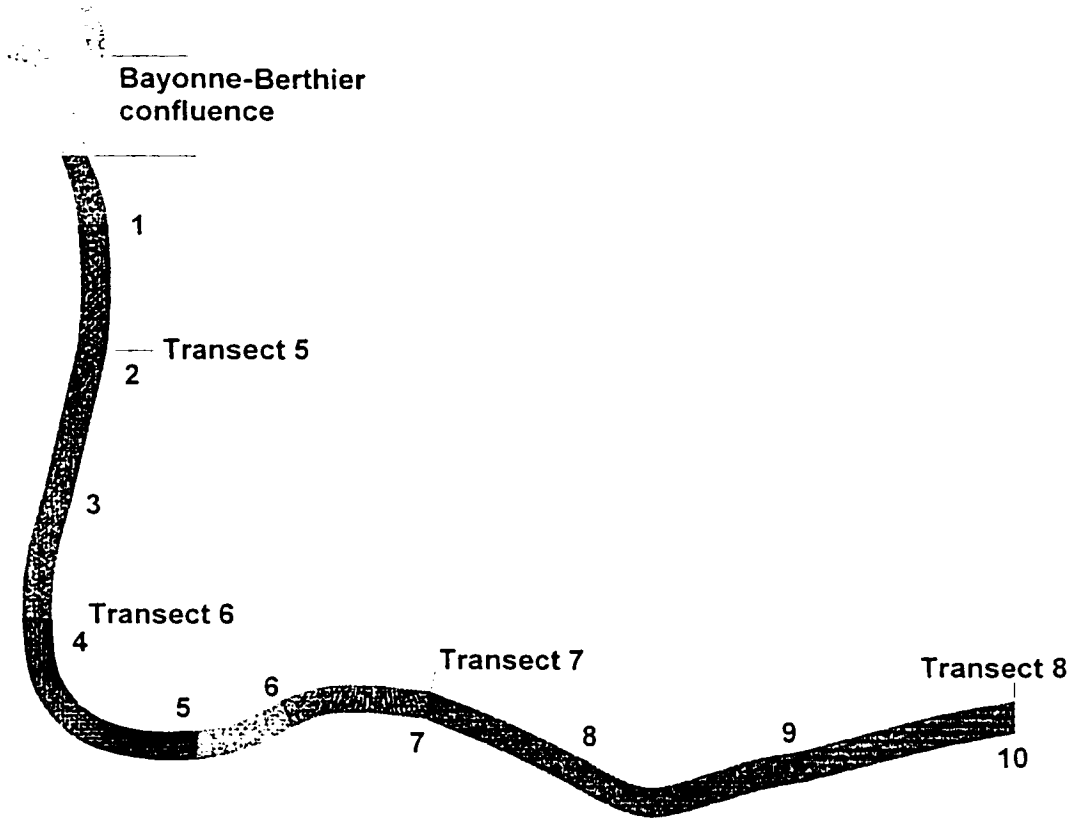

Figure 5.12 Combined grids for the channel downstream of the Bayonne-Berthier confluence

Figure 5.13 Contour plot of predicted electrical conductivity for low flow condition of extended channel

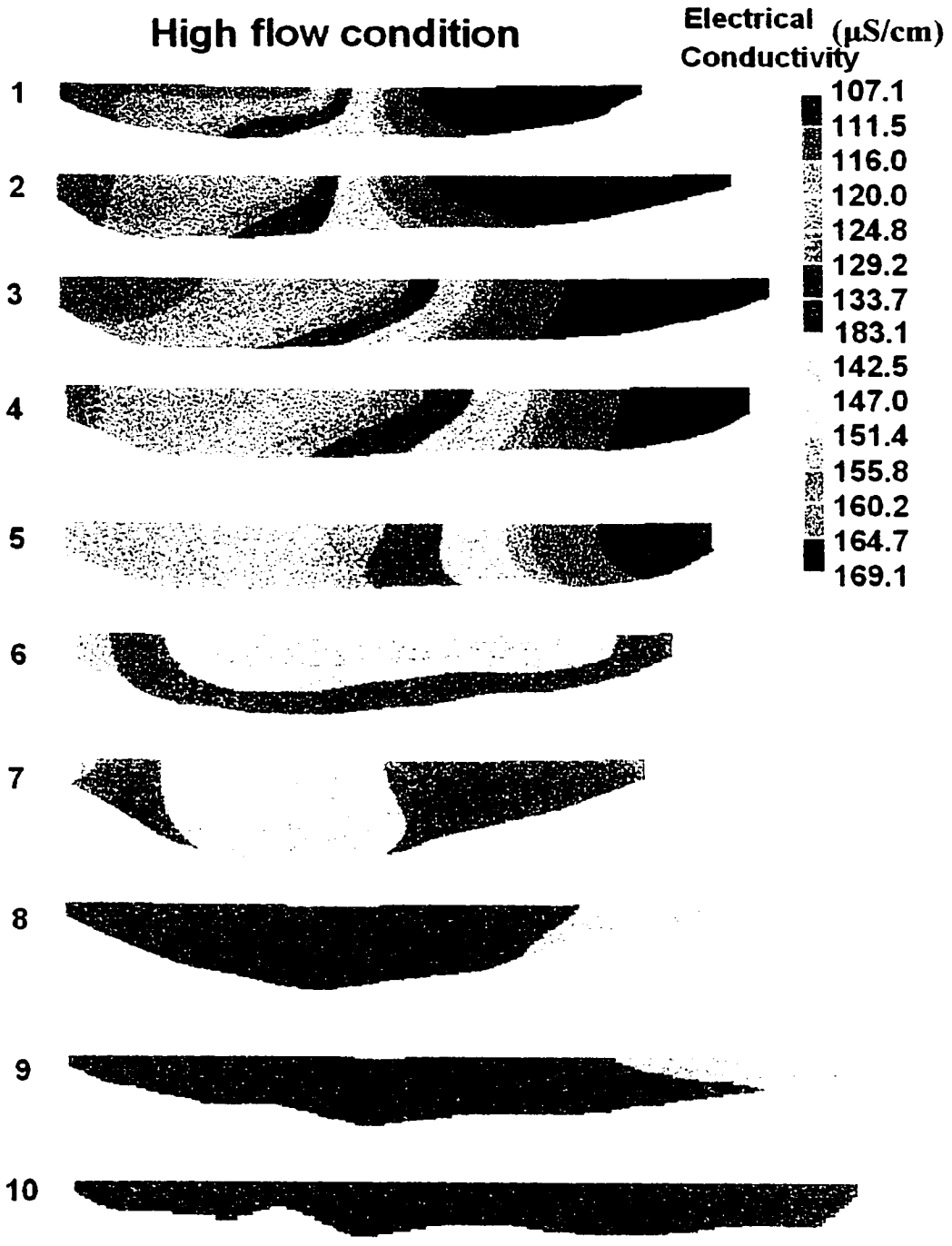

Figure 5.14 Contour plot of predicted electrical conductivity for high flow condition of extended channel

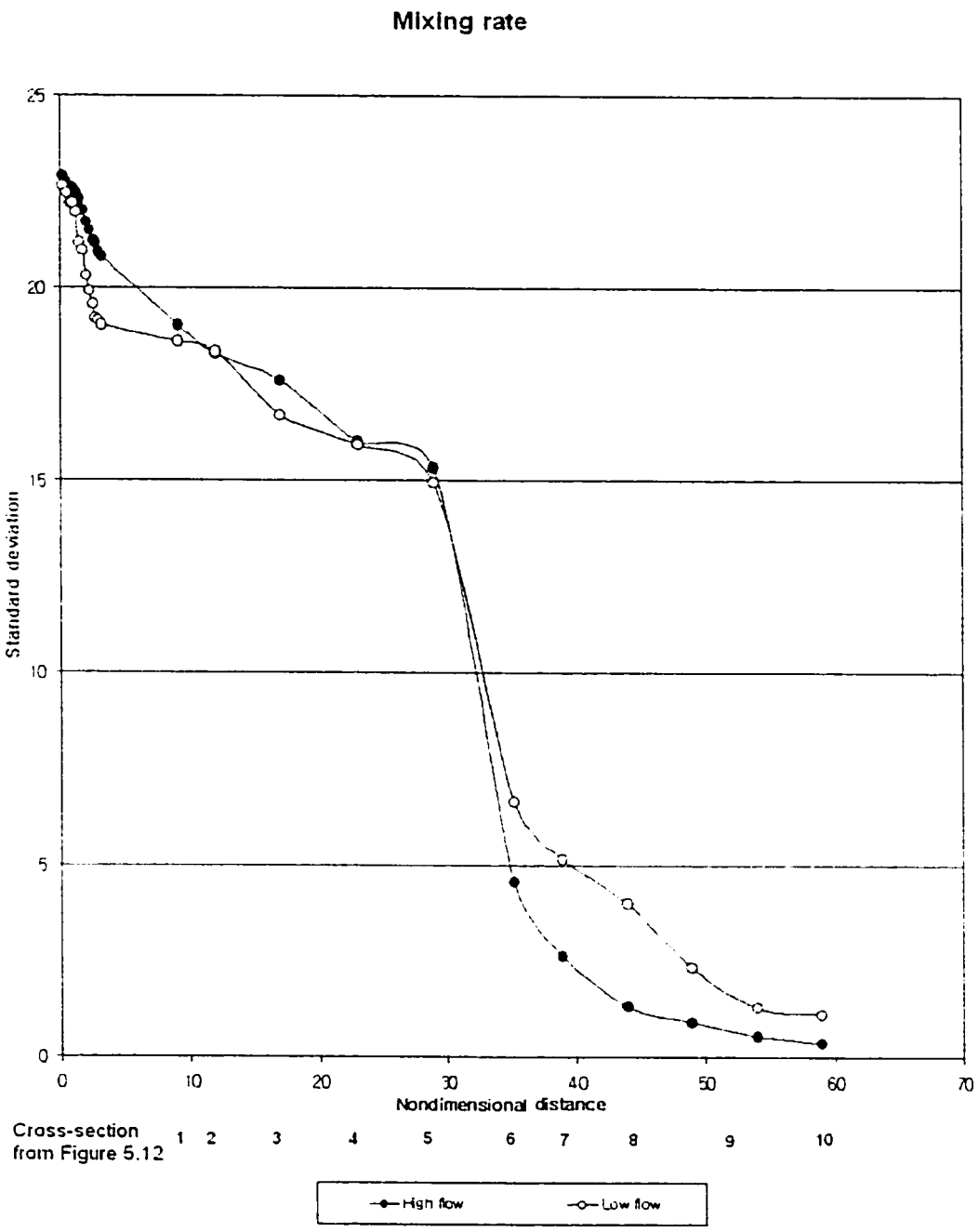

Figure 5.15 Mixing comparison between high and low flow condition for extended channel using standard deviation

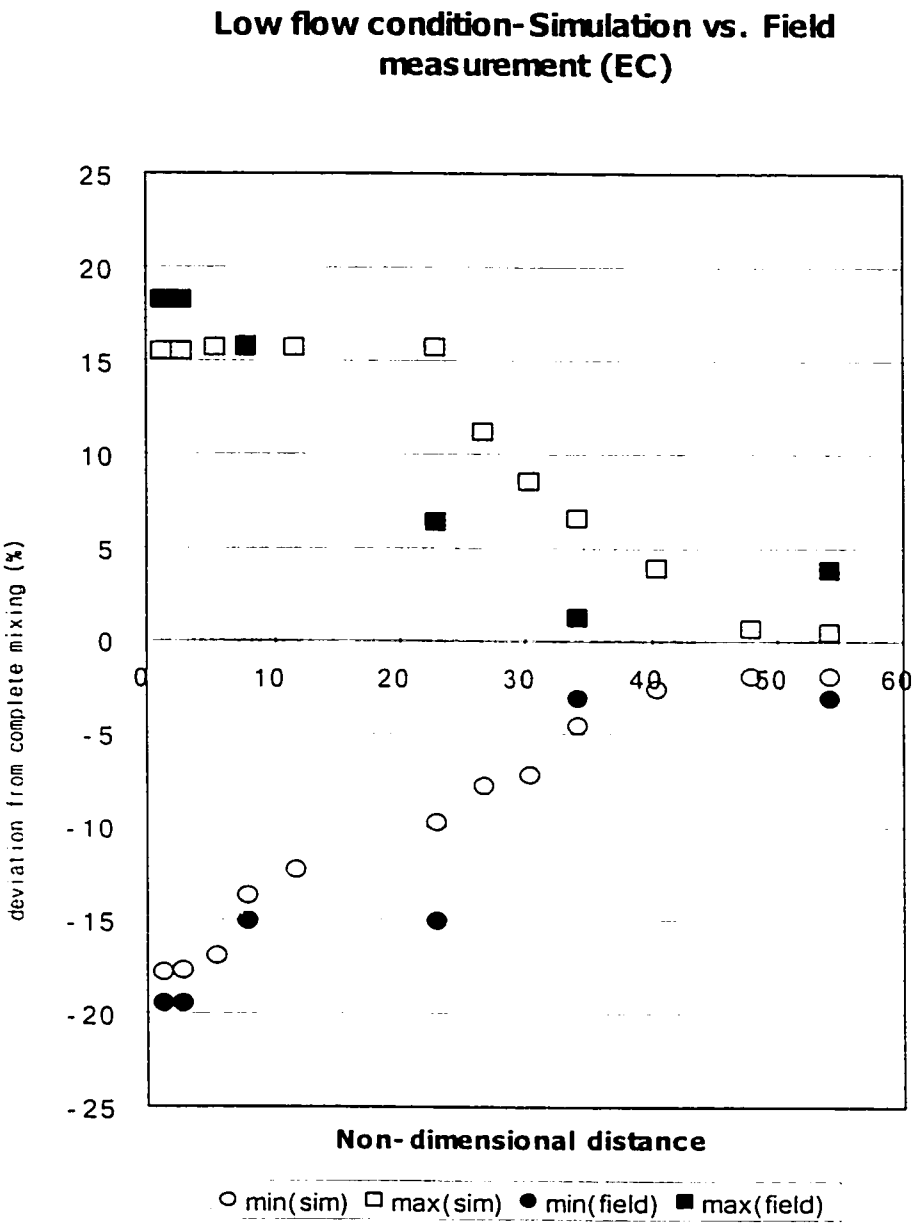

Figure 5.16 Deviation plot for low flow condition

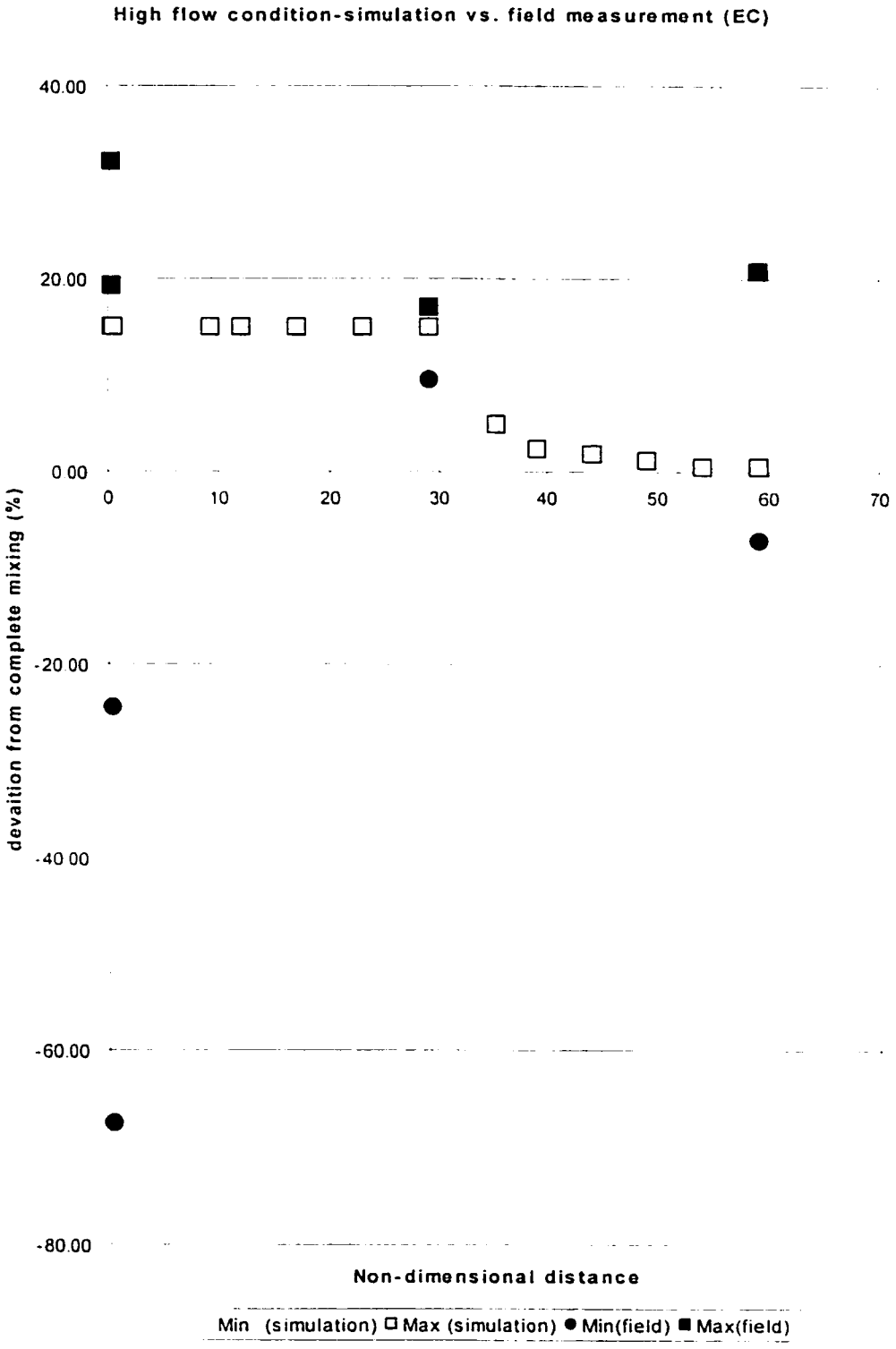

Figure 5.17 Deviation plot for high flow condition

REFERENCES

Andrews, E. D., and Nelson, J. M. (1989). "Topographic response of a bar in the green river, Utah, to variation in discharge." IN Ikeda, S., and Parker, G. (eds), *River meandering: American Geophysical Union*, Water Resource Monograph, 12, 463-485.

Ashmore, P. E. (1982). "Laboratory modeling of gravel braided stream morphology." *Earth surface processes ad landforms*, 7, 201-255.

Bencalal, K.E. McKnight D.M, and Zellweger G.W. (1987). "Evaluation of natural tracers in acidic and metal rich streams." *Water Resources Research*, 23, 5, 827-836.

Best, J. L., and Reid, I. (1984). "Separation zone at open channel junctions." *J. Hydr. Engrg.*, ASCE, 110(11), 1588-1594.

Best, J. L. (1987). "Flow dynamics at river confluences: Implications of sediment transport and bed morphology." *Recent Devel. In Fluvial Sedimentology*, SEPM Spec. Publ. 39, F. G. Etheridge, R. M. Flores, M.D. Harvey, eds., 27-35.

Best, J. L and Roy, A. G. (1991). "Mixing layer distortion at the confluence of channels of different depth." *Nature*, 350, 411-413.

Biron, P., De Serres, B., Roy, A. G., and Best, J. L. (1993a). "Shear layer turbulence at an unequal depth channel confleunce", In: Clifford, N.J., French, J.R., Hardisty, J. (Eds.), *Turbulence: Perspectives on Flow and Sediment Transport*, John Wiley and sons, 197-214.

Biron, P., Roy, A. G., Best, J. L., and Boyer, C. J. (1993b). "Bed morphology and sedimentology at the confluence of unequal depth channels." *Geomorphology*, 8, 115-129.

Biron, P., Best, J. L., and Roy, A. G. (1996). "Effect of Bed discordance on flow dynamics at open channel confluences." *J. Hydr. Engr.*, ASCE, 122, 676-682.

Biron, P., Best, J. L., and Roy, A. G. (1996). "Turbulent flow structure at concordant and discordant open-channel confluences." *Experiments in fluids*, 21, 437-446.

Biron, P. M., Richer, A., Kirkbride, A. D., Roy, A. G., and Han, S. (in press). "Spatial patterns of water surface topography at a river confluence." *Earth Surface Processes and Landforms*.

Bradbrook, K. F., Lane, S. N., Richards, K. S., and Roy, A. G. (1998). "Investigation of controls on secondary circulation in a simple confluence geometry using a three-dimensional numerical model." *Hydrological processes*, 12, 1371-1396

Bradbrook, K. F., Lane, S. N., and Richards, K. S. (2000a). "Numerical simulation of three- dimensional, time-averaged flow structure at river confluences." *Water Resources*

Research, 9, 2731-2746.

Bradbrook, K. F., Lane, S. N., Richards, K. S., Biron, P. M. and Roy, A. G. (2000b). "Large eddy simulation of periodic flow characteristics at river channel confluences." *J. Hydr. Research*, 38, 207-215.

Bradbrook, K. F., Lane, S. N., Richards, K. S., Biron, P. M, and Roy, A. G. (2001). "Role of bed discordance at symmetrical river confluences." *J. Hydr. Engrg.*, ASCE, 127, 351-368.

Bridge, J. S., and Gabel, S. L. (1992). "Flow and Sediment dynamics in a low sinuosity, braided river: Calamus River, Nebraska Sandhills." *Sedimentology*, 39, 125-142.

Choudhury, D. (1993) "Introduction to the renormalization group method and turbulent flow", *Fluent Inc. Technical memorandum* TM-107

Chu, V. H., and Babarutsi, S. (1988). "Confinement and bed-friction effects in shallow turbulent mixing layers." *J. Hydr. Engrg.*, ASCE, 114, 1257-1274.

De Serres, B., Roy, A. G., Biron, P. and Best, J. L. (1999). "Three-dimensional structure of flow at a confluence of river channels with discordant beds." *Geomorphology*, 26, 313-335.

Elhadi, N., Harrington, A., Hill, I., Lau, Y. L., and Krishnappan, B. G. (1984). " River mixing: A state-of-the-art report." *Can. J. Civ. Eng.* 11, 585-609.

Fujita, I., and Komura, S. (1989). "Visualization of the flow at a confluence." *Proceedings of the Third International Symposium on Refined Flow Modeling and Turbulence Measurements*, International Association for Hydraulic Research, Tokyo. Japan, 691-689.

Gaudet, J. M. (1995). "Le mélange des écoulements à l'aval des confluents de cours d'eau", *Unpublished Ph.D Thesis*, Université de Montréal.

Gaudet J. M. and Roy, A. G. (1996). "Effect of bed morphology on flow mixing length at river confluences." *Nature*, 373, 138-139.

Gurran, S. K, Karki, K. S., and Hager, W. H., (1997). "Subcritical junction flow." *J. Hydr. Engrg.*, ASCE, 123, 447-455.

Hager, W. H. (1987). "Discussion of 'Separation zone at open channel junctions, by J. L. Best and I. Reid." *J. Hydr. Engrg.*, ASCE, 113(4), 593-543.

Hodskinson, A. and Ferguson, R. I. (1998). "Numerical modeling of separated flow in river bends: Model testing and experimental investigation of geometric control on the extent of flow separation at the concave bank." *Hydrological Processes*, 12, 1323-1338.

Hsu, C., Lee, W., and Chang, C. (1998). "Subcritical open-channel junction flow." *J. Hydr. Engrg.*, ASCE, 124, 847-855.

Hsu, C., Wu, F. and Lee, W. (1998). "Flow at 90 equal width channel junction." *J. Hydr. Engrg*, ASCE, 124(2),186-191.

Jayatillike, C.L.V. (1969). "The influence of the Prandtl number and surface roughness on the resistance of the sublayer to momentum and heat transfer." *Prog. in Heat & Mass Transfer*, Pergamon Press, 1, 193-329.

Knupp, P. and Steinberg, S. (1993). *Fundamentals of grid generation*, CRC press, Inc

Lam, S. H. (1992). "On the RNG theory of turbulence", *Physics of fluids A*, 4, 1007-1017.

Lane, S. N., Richards, K. S., chandler, J. H. (1995). "Within–reach spatial pattern of process and channel adjustment." *In: Hickin, E.J. (Ed.), River Geomorphology*, 105-130.

Lane, S. N., Bradbrook, K. F., Richards, K. S., Biron, P., and Roy, A.G. (1999). "The application of computational fluid dynamics to natural river channels: three-dimensional versus two-dimensional approaches." *Geomorphology*, 29, 1-20.

Launder B. E., and Spalding, D. B. (1974) "The numerical computation of turbulent flows", *Comp. Methods Appl. Mech. Eng.*, 3, 269-289.

Lin, J. D., and Soong. H. K. (1979). "Junction losses in open channel flows." *Water Resour. Res.*, 15(2), 414-418.

Mamedov, A. S. (1989). "Hydraulic calculation of a confluence." *Hydrotechnical construction*, 23(9), 553-556.

McLelland, S. J., Ashworth, P. J., and Best, J. L. (1996). "The origin and development of coherent flow structures at channel junctions." *In Coherent Flow Structures in Open Channels*, Ashworth, P. J., Bennett, S. J., Best, J. L., and McLellanf, S. J. (eds). Wiley: Chichester; 491-517.

Modi, P. N., Ariel, P.D., and Dandekar, M. J. (1981). "Conformal mapping for channel junction flow." *J. Hydr. Div.*, ASCE, 107(12), 1713-1733.

Mosley M. P. (1976). "An experimental study of channel confluences." *J. Geology*, 84, 535-562.

Meselhe, E. A. and Sotiropoulos, F. (2000). "Three dimensional numerical model for open channels with free surface variations." *AIAA journal*, 38(n2), 115-121.

Nagata, N., Hosoda, T., and Muramoto, Y. (2000). "Numerical analysis of river channel

processes with bank erosion." *J. Hydr. Engrg.*, ASCE, 126, 243-252.

Ouillon, S. and Dartus, D. (1997). "Three-dimensional computation of flow around groyne." *J. Hydr. Engrg.*, ASCE, 123, 962-970.

PHOENICS manual, Concentration, heat and momentum (CHAM)

Ramamurthy, A. S., Carballada, L. B., and Tran, D. M. (1988). "Combining open channel flow at right angled junctions." *J. Hydr. Engrg.*, ASCE, 114(12), 1449-1460.

Rhoads, B. L. and Kenworthy, S. T. (1995). "Flow structure at an asymmetrical stream confluence." *Geomorphology*, 11, 273-293.

Rhoads, B. L. (1996). "Main structure of transport effective flows at an asymmetrical confluence when the main stream is dominant." *In: P.J. Ashworth, S.J. Bennett, J.L. Best, and S.J. McLelland (Editors), Coherent Flow Structures in Open Channels*, John Wiley & Sons Ltd, Chichester, 491-517.

Rhoads, B. L. and Kenworthy, S. T. (1998). "Time averaged flow structure in the central region of a stream confluence." *Earth Surface Processes and Landforms*, 23, 171-191.

Rhoads, B.L. and Sukhodolov, A.N. (2001) Field investigation of three-dimensional flow structure at stream confluences: 1. Thermal mixing and time-averaged velocities. *Water Resources Research*, 37, 9, 2393-2410.

Rodi, W., (1984), *Turbulence models and their application in hydraulics-a state of the art review*. International Associations for Hydraulic Research, Delft, The Netherlands.

Roy, A. G., De Serres, B. (1989). "Morphologie du lit et dynamique des confluents de cours d'eau." *Bull. Soc. Geogr.* Liege 25, 113-127.

Rutherford, J. C. (1994). *River Mixing*. John Wiley & Sons.

Shimizu, Y., and Itakura, T. (1989). "Calculation of bed variation in alluvial channels." *J. Hydr. Engrg.*, ASCE, 115(3), 367-387.

Smagorinsky, J. (1963). "General circulation experiments with the primitive equations." *Monthly Weather Review*, 93, No.3, 99-164.

Spalding, D. B. (1972), "A novel finite-difference formulation for differential expressions involving both first and second derivatives." *Int.J.Num.Meth.Eng.*, 4, 551-559.

Taylor, E. H. (1944). "Flow characteristics at rectangular open channel junctions." *Trans.*, ASCE, 109, 893-912.

Thurhill, A., and Mamone, A. C. (1997). "Selections of confluences sites with ice

problems for structural solutions." *USA Cold Regions Research and Engineering Laboratory, Special report* 97-4.

Tingsanchali, T., and Mahaswaran, S. (1990). "2-D depth averaged flow computation near groyne." *J. Hydr. Engrg.*,ASCE, 116(1), 71-86.

Uijttewaal, W. S. J. and Rooji, R. (2000). "Effects of shallowness on the development of free surface mixing layer." *Physics of Fluids*, 12(2), 392-402.

Webber, N. B., and Greated, C. A. (1966). "An investigation of flow behavior at the junction of rectangular channels." *Proc., Inst. Civ. Engr.*, London, England, 34, 321-334.

Weber, L. J., Schumate, E. D., and Mawer, N. (2001) "Experiments on flow at a 90° open-channel junction." *J. Hydr. Engrg.*, ASCE, 127, 340-350.

Weerakoon, S. B., and Tamai, N. (1989). "Three dimensional calculation of flow in river confluences using boundary fitted co-ordinates." *J. Hydroscience and Hydr. Engrg.*, 7, 51-62.

Weerakoon, S. B. (1990). "Flow structure and bed topography in river confluences." *Unpublished Ph.D. Thesis*, University of Tokyo, Tokyo, Japan.

Weerakoon, S. B. Kawahara, Y., and Tamai, N. (1991). "Three dimensional flow structure in channel confluence of rectangular section." *Proceedings XXIV Congress, International Association for Hydraulic research*, A373-380.

Wilcox, D.C. (1998). *Turbulence modeling for CFD*. DCW Industries.

Wu, W., Rodi, W., and Wenka, T. (2000). "3D numerical modeling of flow and sediment transport in open channels." *J. Hydr. Engrg.*, ASCE, 126, 4-15.

Yakhot, V. and Orszag, S. A. (1986). "Renormalization group analysis of turbulence:. I. Basic Theory.", *J. of Scientific computing*, V.1, (1) pp.1-51.

Yakhot, V., Orszag, S.A., Thangam, S., Gatski, T.B., and Speziale, C.G.. (1992). "Development of Turbulence Models for Shear Flows by a Double Expansion Technique" *Physics of Fluids, A*, v. 4, (7), 1510 – 1520.